

Carnegie Mellon University
MELLON COLLEGE OF SCIENCE

THESIS

SUBMITTED IN PARTIAL FULFILLMENT OF THE REQUIREMENTS
FOR THE DEGREE OF

DOCTOR OF PHILOSOPHY IN THE FIELD OF PHYSICS

TITLE: "Data analysis of Rayleigh-Taylor unstable flows."

PRESENTED BY: Nora Swisher

ACCEPTED BY THE DEPARTMENT OF PHYSICS

SNEJANA ABARJI 8/26/16

SNEJANA ABARJI, CHAIR PROFESSOR DATE

STEPHEN GAROFF 8/26/16

STEPHEN GAROFF, DEPT HEAD DATE

APPROVED BY THE COLLEGE COUNCIL

REBECCA DOERGE 8/26/16

REBECCA DOERGE, DEAN DATE

Data analysis of Rayleigh-Taylor unstable flows

by

Nora Swisher

Submitted in partial fulfillment of the
requirements for the degree of

Doctor of Philosophy

at

Carnegie Mellon University

Department of Physics

Pittsburgh, Pennsylvania

Advised by Professor Snezhana Abarzhi

Department Sponsor: Professor Stephen Garoff

August 23, 2016

Contents

1	Introduction	10
1.1	Analysis of Data	11
1.2	Overview of this thesis	15
2	Methods	17
2.1	Experimental Methods	17
2.1.1	Overview	17
2.1.2	Experiments in the high energy density regime	18
2.2	Theoretical Methods	28
2.2.1	Overview	28
2.2.2	Numerical Methods	31
2.2.3	Modeling RTI with time dependent accelerations	34
2.2.4	Momentum Model	37
2.2.5	Stochastic Model	42
3	Data analysis of laboratory supernova experiments	45
3.1	Introduction	45
3.2	Experimental results	48
3.2.1	Scaling of experimental measurements	48
3.2.2	Curvature of the shock front and interface envelope	51
3.2.3	Amplitude of the interface	53
3.3	Comparison with the momentum model	56
3.4	Discussion	59
4	Data analysis of multiplicative noise in Rayleigh-Taylor mixing	63
4.1	Introduction	63
4.1.1	Relationship to previous studies	65

4.2	Results	66
4.2.1	Exponent and coefficient sensitivity	66
4.2.2	Critical value of the acceleration exponent	67
4.2.3	Asymptotic solutions	69
4.2.4	Invariant quantities	70
4.2.5	The effect of $\langle C \rangle$	73
4.2.6	Number of trajectories	74
4.3	Discussion	77
5	Data analysis of simulated Richtmyer-Meshkov interfacial growth	81
5.1	Introduction	81
5.2	Simulation setup	84
5.3	Diagnostics	85
5.4	Results	88
5.4.1	Velocity of the background motion	88
5.4.2	Growth of the interface amplitude	89
5.4.3	Empirical model of the interface growth	91
5.5	Energy partitioning	94
5.6	Discussion	95
6	Conclusion	98

List of Figures

2.1	Schematic of the laboratory supernova experiment. This illustration shows a side view of the cylindrical experiment tube. The blast wave moves from left to right.	21
2.2	Typical x-ray radiograph of an experiment with a single mode interface; image is taken at $21ns$. This image shows the experiment in the same orientation as Figure 2.1.	23
2.3	Two example radiograph images illustrating measurements and image quality. The shock, bubbles, and spikes all propagate from left to right and the dark grid used for pixel to meter conversion can be seen on the side of the experiment tube. Small crosses mark position measurements analyzed in Chapter 3.	24
2.4	Examples of the pixel intensity method performed on high (a) and low (b) quality images.	26
2.5	Schematic of the interface separating fluids of different densities undergoing RT flow evolution [2]. The spikes of heavy fluid propagating downwards correspond to the dark regions in Figure 2.3 while the bubbles of light fluid propagating upwards correspond to light regions near the interface in Figure 2.3.	28
2.6	Four example plots generated from SPH code simulations of RMI in a two-dimensional domain. In order from left to right, they show region, temperature, density gradient and velocity curl.	34
2.7	Diagram of mixing regime. The dissipation dominated mixing regime (red) is analogous to RM-type mixing while the acceleration dominated mixing regime (blue) is analogous to RT-type mixing	40

2.8	Stochastically modeled time evolution of $C(t)$ normalized by its average value, $\langle C \rangle$	44
3.1	Analysis of the radius of curvature; error bars indicate standard deviations. [94]	52
3.2	Spike amplitude for (a) single mode targets with $h \sim t^{1.39}$, (b) large-two-mode targets with $h \sim t^{1.14}$, and (c) all target types with $h \sim t^{1.12}$. Measurements of large-two-mode targets are shown as squares, two-mode small targets as circles, and single mode targets as diamonds.[94]	54
3.3	Average data (red squares) plotted with the fit from the linearized method. The dashed lines show the fit function with +/- the error of the fit exponent.	56
3.4	Measured spike amplitude points plotted with smooth power law fits $h \sim t^b$. [94]	59
4.1	The modeled solutions normalized by analytic values.	68
4.2	The external acceleration g (black), the solution h (red) and the solutions first and second derivative (blue and green) plotted on a log-log plot to demonstrate the power law dependence for both sub-regimes of the mixing regime.	69
4.3	The appropriate (main figures) and inappropriate (inserts) characteristic values in the acceleration (a) and dissipation (b) dominated regimes.	71
4.4	The invariant value plotted as a approaches $a_{critical}$ in each regime. As the colors get lighter, a gets closer to $a_{critical}$	72
4.5	Two characteristic values measured across the entire range of tested acceleration exponents. In their respective regimes above and below $a_{critical}$ they are nearly flat, but diverge as they cross the critical value.	73
4.6	The invariant values plotted for various values of $\langle C \rangle$	75
4.7	The time evolution of $C(t)$ plotted for various numbers of trajectories. As the value is averaged over more trajectories, the fluctuations become narrower.	76
4.8	PSD of C.	77
4.9	Power-spectrum-density.	78

5.1	Simulation results showing the compound motion induced by the shock. The shock passes through the interface between fluids of different acoustic impedance (from left to right). After the shock passage, the fluid moves as a whole with speed $v_\infty < v_{shock}$ to the right and the interface grows due to the instability with growth rate $v_0 < v_\infty$ [31]. The colors represent region, a property that corresponds to the initial positions. The light fluid is shown in red and green and the heavy fluid is shown in blue.	83
5.2	Illustration of the technique used to measure the amplitude of the interface. Black lines mark the spike and bubble positions and their difference provides the measure of the interface amplitude [31].	87
5.3	The time evolution of difference between the spike position and bubble position. The first 6 time steps after $t = 0$ are used to calculate the initial growth rate, v_0 [31].	87
5.4	The initial RMI growth rate as a function of initial perturbation amplitude from simulation results (squares), linear theory (line), and weakly nonlinear theory (dashed line) [31].	91
5.5	The initial growth rate of the interface (v_0/v_∞) versus the initial perturbation amplitude (a_0/λ). In (b) the data collapses when divided by Atwood number, A	93
5.6	One example of details of the fit. (a) shows the v_0/v_∞ data (dots) and the fit line (dashed line) while (b) plots the difference between the two (the residuals).	94
6.1	Experimental images from single mode target types.	105
6.2	Experimental images from small-two-mode target types.	106
6.3	Experimental images from large-two-mode target types.	107
6.4	Experimental images from planar target types.	108

List of Tables

2.1	Asymptotic solutions of the momentum model for the combination case, $L \sim t^\beta$	41
2.2	Asymptotic solutions of the momentum model for the nonlinear regime, $L = \lambda$	41
2.3	Asymptotic solutions of the momentum model for the mixing regime, $L = h$. Note that $a_{critical} = -2 + (1 + C)^{-1}$	41
3.1	Scaling parameters and characteristic values of quantities of RT dynamics based on τ and λ , the characteristic scales in experiments [94].	50
3.2	Mean values of the parameters of theoretical solutions and numerical models for spike amplitude growth.	57
5.1	Scaling values v_∞ and τ . The fluids are monoatomic gases with adiabatic index $\gamma = 5/3$. The velocity values are rather large due to the use of artificial gasses in order to improve computational efficiency. When the computations are scaled to realistic values, excellent agreement is achieved with experiments. [31]	86
5.2	Simulated [31] and theoretical [103] values of the background velocity normalized by the speed of sound in the light fluid. The results agree within 1% for all simulated Mach and Atwood values.	89
5.3	Fitted coefficient values from the empirical model (Equation 5.2) for all simulated values of Mach and Atwood number. . .	92

Personal Introduction

I started physics research when I performed experimental studies of granular materials with Brian Utter at James Madison University. I thoroughly enjoyed learning analysis techniques to discover what data may tell us about the physical laws governing a system. To study granular materials, I applied image analysis to experiments to find qualitative and quantitative descriptions of a stochastic process [95].

At Carnegie Mellon University, I worked in Steve Garoff's lab for about one year, developing measurement equipment which would provide more detail about the surface tension experiments we were studying. I was motivated at the prospect, since it would provide more quantitative data to analyze. To me data analysis is the most exciting part of the scientific process. I enjoy making new statements by synthesizing information.

At the beginning of 2014, Snezhana Abarzhi talked to me about her research. Study of Rayleigh-Taylor instability is in active development and provides lots of opportunity for analysis of data from experiments and simulations. In this field data analysis has additional challenges because experiments and simulations are difficult to perform and it is difficult to analyze without observer effects. Rayleigh-Taylor flows present challenges to theoretical analysis, experimental design, and simulations because of the nature of the instability. Though I was less interested in mathematical task of solving boundary value problems, Snezhana provided an opportunity for me to perform data analysis on Rayleigh-Taylor experiments and simulations.

I am grateful for my years of training in experimental physics and data analysis with Brian and Steve, and I thank Snezhana for introducing me to this exciting field and giving me the opportunity to study with her.

Abstract

Rayleigh-Taylor and Richtmyer-Meshkov instabilities (RTI and RMI) occur when a fluid interface between fluids of different densities is accelerated against the density gradient. RTI/RMI plays an important role in the dynamics of fluids and plasmas on microscopic scales, such as inertial confinement fusion, through astronomical scales, such as supernova explosions. These problems have been studied for decades, yet it remains a challenge to observe, model, and describe RTI/RMI mathematically. Without the tools used to analyze stable equilibrium, we must find more robust analyses. This work uses robust data analysis techniques to systematically study RT unstable flows.

We report a thorough analysis of experimental data in supernova experiments conducted at high powered laser facilities, evaluating what information experiments and simulations may tell us about the fundamentals of RTI and RT mixing in high energy density plasmas by comparing the data with rigorous theoretical approaches.

We investigate the statistically unsteadiness of RT mixing by numerically modeling the set of stochastic nonlinear differential equations which govern the rate of change of momentum in a packet of fluid undergoing RT instability. By analyzing the modeled solutions, we measure the influence of fluctuations on measurable quantities, find new characteristic values which may be used as to diagnose the regime of an experiment or simulation, and measure the spectra of fluctuations as they propagate throughout the system.

We study the effect of the initial perturbation amplitude on the RMI interfacial dynamics using Single Particle Hydrodynamics simulations. The compound motion of the interface and bulk fluid flow is measured, an empirical model is found to describe data, and we find an upper bound for the amount of energy deposited to the interface.

There exists a plethora of data that may still be analyzed systematically,

as exemplified in this thesis. Future work may improve the fits of experimental data by exploring well designed parameter spaces, model additional stochastic effects, and measure small scale features of flow quantities in simulations.

Chapter 1

Introduction

Portions of this chapter are published in [94]

This thesis presents an integrated study of Rayleigh-Taylor and Richtmyer-Meshkov instabilities to demonstrate the power of comparing experimental results, simulations, and theoretical analysis. We contribute much needed analysis with special attention to systems related to high energy density regimes.

Rayleigh-Taylor instability (RTI) is an important phenomenon occurring in both natural and artificial phenomena. Rayleigh-Taylor (RT) instability occurs whenever fluids are accelerated against their density gradient. A small perturbation at a fluid interface quickly grows, transitions to a nonlinear stage where large-scale coherent structures and small-scale irregularities occur, then develops into turbulent mixing. In the limit when the acceleration is provided by a shock wave, it is called Richtmyer-Meshkov instability (RMI). RT mixing is an important process seen in stellar phenomenon, inertial confinement fusion, and everyday life. It occurs in mundane situations such as water spilling from a cup, as well as exotic situations like supernova explosions. RTI plays a crucial role in inertial confinement fusion [47, 28, 43, 61]. Radial compression of imploding Z-pinch, interaction of plasma liner with targets in magneto-inertial fusion, and material transformation under impact are all influenced by RTI dynamics [91, 36, 79, 25, 104, 83]. Additionally, it may be a mechanism that influences the creation of heavy elements in supernova explosions [18, 63, 17]. Anytime an accelerated fluid has a density gradient, RTI may greatly influence the dynamics. RTI is not limited to normal matter, but also occurs in high energy density fluids and plasmas. By studying RTI and RMI, we will better understand processes important to

developing inertial confinement fusion and supernova explosions. RTI/RMI presents a challenging problem because it is a nonlinear, anisotropic (different characteristics in different directions), multi-scale (important processes happen at different spatial scales), and statistically unsteady process (fluctuations occur around evolving mean values) [4, 2]. Currently, rich sources of data exist, both from high energy laser laboratories and multiphysics simulations spanning large ranges of scales. The systematic analysis of these data is in high demand.

1.1 Analysis of Data

It is not enough to read out what our experimental instruments and simulations tell us. It is important to perform synergistic analysis on multiple experiments, simulations, and theories. In order to do this we must understand the relevant characteristic and invariant values, the effect of noise on measurables, how to appropriately fit data, and the nature of information available from experiments, simulations, and theory. While these data analysis ideas are applicable generally, they are particularly important when studying RTI/RMI. Physicists have been analyzing systems in stable equilibrium for a long time; there are many well-developed tools for analyzing stable problems. However, systems exhibiting RTI/RMI are manifestly unstable. This simple difference introduces many complications. To name a few: perturbation methods must be applied carefully and are only applicable for very short times; experiments are very sensitive to initial conditions; and discretizing the system for simulations may alter the behavior at small scales.

Understanding the role of experiments, simulations, and theory

Scientific knowledge is advanced by the interplay between experiment and theory. Especially for RTI/RMI in high energy density regimes, experimental design and development of simulations is given careful effort and many resources [56, 57, 37, 82, 81]. Analysis of the data produced by these technological achievements is in demand. This thesis utilizes data sources from experiments and simulations as well as theoretical tools to systematically analyze RTI unstable flows. Such a synergistic study is required to advance our understanding of RTI/RMI. In order to perform multifaceted analysis, we must understand the relationships between experiments, simulations, and

theory.

Experiments and simulations are both observations of a controlled system, though each has unique advantages and disadvantages. In particular, experiments have high fidelity but do not provide complete information while simulations provide complete information but are not constrained by physical reality. Experimental results are physically true (although not necessarily analyzed appropriately!), but simulations are only as accurate as the theories used in the code.

Experimental results require appropriate interpretation. RTI/RMI experiments may exhibit large variations in measurable quantities because of inherent stochastic processes and the strong influence of initial conditions, making it difficult to determine precise values. When analyzing simulated data, one must ensure a lack of computational errors before evaluating the accuracy of the equations and parameters used in the simulation. In RTI/RMI simulations, numerical viscosity and surface tension may play important roles at the interface between the two fluids and must not interfere with the natural development of the instability.

Cautious synergistic analysis of experiments and simulations helps us understand the physical behavior of experiments with an expanded set of parameters because all the known quantities of simulations may be varied until agreement with experimental measures is found. With the help of experimental benchmarks, simulations help us infer immeasurable parameters or results in immeasurable parameter ranges. Since RTI/RMI presents unique challenges to theoretical, experimental, and numerical techniques, we must be particularly cautious in our analysis. Using multiple approaches may act as checks and balances to ensure our results are accurate. Due to the sensitivity on initial conditions and the stochastic nature of late stage RTI/RMI evolution, single experiments and simulations have less meaning than aggregate results. This thesis analyzes data from multiple sources in order to achieve a robust analysis (Chapters 3 through 5).

The use of characteristic and invariant values

It is important to look for invariant quantities in physical systems in order to learn about the symmetries and underlying processes involved in the problem [4, 2, 58, 26]. Invariant quantities determined by combinations of measurable parameters can provide insight into the physical significance of the behavior of a system. While individual measurements tell you about that particular

physical quantity, invariant values tell you about the fundamental physics behind the behavior. In RTI/RMI systems, it can be challenging to find invariant quantities because most measurables are time dependent and statistically unsteady. Invariant quantities are identified and used to diagnose the regime of a RTI system in Chapter 4.

When analyzing experimental data, it is important to obtain measurements that are consistent with each other and that are comparable with other studies in order to gain all of the individual advantages of experiments, simulations, and theory as described above. This is particularly important in data analysis of the RTI/RMI experiments, which occur over widely varying parameter regimes and often have limited measurable quantities and/or limited resolution of data [Section 2.1]. In order to draw consistent conclusions when comparing different data sets, measurements from separate sources must be scaled by a single characteristic value. A good characteristic scaling value should be robust, should depend on experimental parameters that are easily controlled and accurately measurable, and should provide reasonable values [58, 26]. Characteristic values are developed in Chapters 3 and 4 and are used throughout this thesis.

A robust characteristic value works for a wide variety of situations. The quantities that determine the characteristic value may vary between experiments, however the characteristic value itself should remain similar across the entire parameter regime. Ensuring robustness of the characteristic value will allow us to make consistent statements about all of the data, without exceptions. This is important to RTI/RMI analysis because the phenomenon occurs on microscopic scales up to astronomical scales and in low and high energy density regimes.

A characteristic value must be determined by parameters that are precisely controllable or accurately measurable. Ideally, a characteristic value will not vary much for the same system with varying initial conditions. In order to characterize the system, the values used must be well-known and determined. For example, ionization in high energy density experiments of RTI cannot be used in a characteristic value because it is not measurable with current diagnostic technology. The wavelength of a laser is well known and varies little between experiments, and thus would make a well controlled characteristic value. In Chapter 3 we use the precision-machined target mass and the well-controlled laser irradiance to determine a characteristic time value.

Finally, a good characteristic scaling will provide reasonable values. This

means that after your data is scaled, the values should be on the order of unity. In the systems we analyze, a sinusoidal initial perturbation is used to induce RTI/RMI in a controlled manner. We scale the perturbation amplitude with the perturbation wavelength, using values from 0 to 1 wavelengths rather than $\sim 10^{-6}m$. The characteristic value should be close to the same order of magnitude as the values we are analyzing. Hence it characterizes the scale of the values by being the same typical size and dimensions of the values.

Understanding the effect of measurables

There are many sources of noise. Intrinsic stochastic quantities and experimental precision can both contribute to noise in data. In addition, unstable equilibrium problems like RTI/RMI are extra sensitive to initial conditions, making measurables vary significantly unless the experimental set up is perfectly controlled. Since any infinitesimal perturbation will grow, a slightly different perturbation may grow significantly differently. In this thesis we focus on intrinsically sensitive and stochastic quantities and leave the problem of experimental precision in RTI/RMI to other studies.

Accounting for intrinsic stochastic quantities and sensitivity to initial conditions is not a trivial task. Sometimes we may use previous knowledge of the system to limit the stochasticity to one particular quantity, or we may know information about the stochasticity such as the distribution or size of the typical fluctuations. It is important to understand potential sources of fluctuations when analyzing data in order to determine how big the tolerance for discrepancies must be. Sensitivity to initial conditions is observed even in state of the art experiments conducted at high powered laser facilities with micro-machined targets. In order to understand RTI/RMI better, we must look at a large quantity of data to improve the statistics and measure mean values. In Chapter 3 we find new results by increasing the previously studied data set by four or five times.

It can be difficult to distinguish different sources of noise experimentally, especially if only one measurement or type of measurement is available. Here simulations can be of service because they provide complete information of the system. In this thesis we simulate multiplicative noise within a model describing RTI growth. Since all the quantities of the model are known (inputs and solutions), we are able to make statements about which quantities are affected by the stochasticity and we are able to characterize the fluctuations

expected in measurable quantities (Chapter 4).

Fitting

Computers are capable of fitting almost any function to a dataset, however computers are not always capable of making smart fitting decisions. There are two important fitting practices relevant to this thesis: using appropriate numbers of adjustable parameters and understanding the behavior of functions with respect to the behavior of physical quantities. The number of adjustable parameters should be small. With too many adjustable parameters, one can fit any data set with precision without learning anything about the data. For example, polynomials can approximate any function on a finite interval with any chosen degree of accuracy if enough terms are used. Simpler fits are generally better and one should not have more adjustable parameters than well known (either controllable or precisely measurable) parameters. In the RTI/RMI field, a commonly used model called the drag model has 7+ adjustable parameters [55, 34, 33]. While such a model may describe the data, it does not provide fundamental information about the system.

By putting forethought into the functions used to fit, physically significant fits are easier to obtain. For example, we often expect physical quantities to have certain qualities like self-similarity, monotonic dependence, symmetry, or to approach some particular value in a limit. By choosing a compatible function with the same qualities, we can build these characteristics into the fit. In this thesis many power law functions are used. This choice occurs because many RTI/RMI flow quantities are known to be self-similar. One must also be aware of the constraints that certain functions place on data fits. For example, determining the exponent of a power law requires several decades of data and/or data with a very fine resolution [58, 26]. This limits the strength of statements we can make by fitting smaller, lower resolution data sets. Significant analysis is made possible by careful, thoughtful fits in Chapters 3 and 5.

1.2 Overview of this thesis

RTI/RMI presents a challenging area of study, despite being studied for decades. In order to gain new insight we thoroughly analyze data and theory. First, descriptions of the experimental (Section 2.1), theoretical (Section 2.2),

and numerical (Section 2.2.2) methods are given, then the results from three integrated analyses each using multiple methods are described (Chapters 3 through 5).

Experimentally we perform careful image analysis of laboratory supernova experiments and discover what experiments may tell us about RT flow by analyzing relevant theories and simulations (Chapter 3).

One simplified, yet robust theoretical model uses symmetries and the conservation of momentum to describe Rayleigh-Taylor (RT) flow (Section 2.2.4). We extend this model by evaluating asymptotic solutions in new regimes (Section 2.2.4), introducing stochasticity to the equations (Section 2.2.5), and we apply the model by fitting to data from laboratory supernova experiments (Section 3.3).

Numerically, we employ a stochastic differential equation solver (Section 2.2.5) as well as a Lagrangian simulator called single particle hydrodynamics (SPH) code (Section 2.2.2). The stochastic differential equation solver models thousands of trajectories over several decades using a momentum-based model with multiplicative noise. SPH code simulates a shock wave interacting with a fluid interface, modeling Richtmyer Meshkov Instability. A broad parameter regime is investigated in both cases and results are compared with experimental results and theoretical analysis (Chapters 4 and 5).

In Chapter 3 experimental results are compared with the momentum model as well as some simulations commonly used in the field. Results from the stochastic numerical code are analyzed with respect to the momentum model in Chapter 4 with notes relating to the general status of experiments in the field. Finally, a broad parameter regime is studied with SPH code and compared with both linear theory and experimental results in Chapter 5.

Chapter 2

Methods

2.1 Experimental Methods

2.1.1 Overview

While RTI occurs in everyday life, well controlled experiments can be challenging. Here we discuss what experiments have been attained by others in the field with special attention for the experiments analyzed in this thesis.

RTI requires three “ingredients” to occur. This unstable equilibrium occurs when there is an interface between two fluids, those fluids have different densities, and an acceleration is applied to the system. The equilibrium position is a perfectly flat interface and any deviation away from equilibrium will grow. The simplest example of RTI occurs when water spills out of an overturned cup. Water and air are the two fluids of different densities and the acceleration is applied by gravity. The instability grows due to perturbations at the surface, which cause the interface to deviate from an ideally planar surface. If paper is placed over the cup, then the interface remains flat and the system remains in equilibrium.

In hydrodynamic RTI/RMI experiments, many challenges arise due to the nature of the instability. Initial interfaces must be extremely well controlled in order to study RTI/RMI seeded with a single mode initial perturbation. Dynamics are strongly dependent on initial conditions- small changes in the initial perturbation may lead to large differences in the dynamics. Experimentally, it is a challenge to achieve a sharp, well-controlled interface [50, 100, 69].

Since RTI/RMI dynamics include compound motion of the bulk velocity

plus the interface growth, experiments must be able to image the interface as it is moving in order to study the interfacial dynamics. The bulk often moves quickly, requiring precision timing, especially in the high energy density regime that requires nanosecond timing between images.

The primary use of experimental data in this thesis occurs in the high energy density regime in Chapter 3. These experiments are described in detail in the following section.

2.1.2 Experiments in the high energy density regime

Portions of this section are published in [94]

Experimentally measuring flow parameters of RTI/RMI in hydrodynamic systems is a challenge because of the fast background motion of the system and sensitivity to initial conditions. Experiments of RTI/RMI in high energy density plasmas (HEDP) is even more challenging. It is important to study these systems in order to better understand supernova explosions and implosions in inertial confinement fusion. Laboratory supernova experiments have been conducted at high powered laser facilities by appropriately scaling parameters contributing to the energy density [37, 82, 56, 57, 17]. In chapter 3 we analyze data from these impressive experiments and compare with simulations and theory. Here we describe the experimental methods.

Supernova experiments are designed to mimic the evolution of supernova SN1987A at high powered laser facilities such as the Omega Laser Facility and the National Ignition Facility in order to study the astronomical system in a controlled environment [79]. SN1987A is a type II core-collapse supernova and its progenitor star has a layered structure. During the star's explosion, a blast wave propagates from the center of the star outwards through the layers of material with progressively decreasing density [102, 17]. The gradients of the fields of pressure and density point in opposite directions in the star's interior, leading to RTI. The outer and inner stellar layers experience extensive interfacial mixing and it is believed that during the supernova explosion, RT mixing may provide special conditions for the generation of elements with heavy atomic mass and thus may explain the abundance of these elements in the universe [17].

A core-collapse supernova is characterized by high energy density [104]. The values of energy density are somewhat similar in the laser experiments [79, 84, 22]. In addition, both supernova and laboratory hydrodynamics can be regarded as self-similar and Eulerian at continuous scales because the

effects of dissipation and diffusion are usually small, and so are the characteristic scales on which dissipation and diffusion occur [4, 20, 51]. This suggests that if the parameters are properly scaled, astrophysical processes can be mimicked and studied in a well-controlled laboratory experiment at high powered laser facilities [84]. Requirements for the systems to achieve such hydrodynamic similarity include the need for collisional thermodynamics accompanied by negligible heat conduction and radiation flux as well as insignificant viscous dissipation. With these conditions in mind, experiments are designed to investigate the interaction of a blast wave with a helium-hydrogen interface in supernova SN1987A [37, 82, 81]. While in realistic laboratory environments the characteristic scales are small ($\sim \mu m$ and $\sim ns$), one may achieve the astrophysical values of energy density by varying the power and time duration of the laser beam and the properties of the target [36, 84, 79, 22].

For example, in supernova SN1987A at time $\sim 2000 s$, the characteristic values are estimated as $\sim 9 \times 10^8 m$ for length, $\sim 2 \times 10^5 m/s$ for velocity, $\sim 7.5 kg/m^3$ for density, and $\sim 3.5 \times 10^{12} Pa$ for pressure. In the first HEDP laboratory experiments in Cu plasma at time $\sim 20 ns$ the corresponding values are $\sim 5.3 \times 10^{-5} m$, $\sim 1.3 \times 10^3 m/s$, $\sim 4.2 \times 10^3 kg/m^3$, and $\sim 6 \times 10^{10} Pa$ [79, 84]. According to the Braginski model, one can further evaluate the Reynolds and Peclet numbers in supernova SN1987A to be $Re \sim 2.6 \times 10^{10}$ and $Pe \sim 2.6 \times 10^5$ while in HEDP laboratory experiments, $Re \sim 1.9 \times 10^6$ and $Pe \sim 1.8 \times 10^3$ [84, 23]. These numbers are all large, implying that the role of dissipation effects is small and occurs on small scales. Remarkably, the Euler number is ~ 0.29 in supernova SN1987A and ~ 0.34 in laboratory experiments. The Euler number is defined as the product of the velocity and the square root of the ratio of the density and pressure. This suggests that the Euler number (or the energy density) is the proper dimensionless scaling parameter for imitating and studying the astrophysical phenomena in laboratory experiments [79, 84]. High powered laser facilities are necessary to achieve experiments with such parameters. Scrupulous analysis of the invaluable experimental data is in demand.

The evolution of core-collapse SN1987A is believed to be driven by a blast wave [102, 17]. Blast waves are induced by a large energy release in a small volume over a short time [97, 86, 41]. With time, their length scale increases and velocity scale decreases. In the case of a uniform compressible fluid, the dynamics of blast waves are described by self-similar solutions [87, 19]. If a blast wave is driven solely by energy transport, the solution belongs to so-

called first-kind self-similarity [97, 86]. If a blast wave is driven by energy and momentum transport (e.g. by an impact), then the solution belongs to the so-called second-kind self-similarity [92, 41]. In the former case the scaling law is set by the problem dimensionality according to whether the energy is released by a point source, a line source, or a planar source. In the latter case, the scaling law depends also on the load history and mass transport at the times of the explosions [87]. The analysis of blast wave propagation in a fluid with exponentially decaying density can be found in [87]. The interaction of blast waves with non-uniform density fields and with density discontinuities is a fundamental and, in many regards, an open problem.

Generation of shocks and blast waves with prescribed properties is an experimental challenge in high powered laser facilities [79, 82, 81]. A common approach is to use laser beams to concentrate a large amount of energy on a small target in a short time [56, 57, 37]. As laser light starts to irradiate the target surface, the outer part of the target material is ablated, and plasma is created. The ablation pressure of this newly created plasma drives a shock wave into the material. The shock strength is extremely high causing the material to behave as a fluid, i.e. unionized and/or partially ionized plasma [16]. Depending on the laser pulse duration as well as the material properties and load history, two regimes are usually realized in experiments: a quasi-steady shock wave for a ~ 1 ns pulse and an ultra-short shock wave for less than 10 ps laser pulse duration [32]. In supernova experiments, the first regime is realized.

For studying RT mixing in supernova experiments, the target is composed of a pair of two initially solid materials, such that the shock propagates from the denser to the lighter fluid. At the fluid interface, the shock splits into a transmitted shock and a centered reflected rarefaction wave thus accelerating the flow [66, 64]. When the temporally uniform ~ 1 ns laser pulse ends, the pressure supporting the initial shock ceases. At the same time, the ablated plasma continues to expand creating a rarefaction wave [56, 57]. This rarefaction wave moves into the material in the same direction as the initial shock and overtakes the shock reducing the flow velocity [37, 82, 81]. It is believed that the resulting dynamics of the fluid flow is similar to that driven by a blast wave [56, 57].

In supernova experiments, due to complex processes induced by the laser radiation, the acceleration is directed from the denser to the lighter fluid, causing the development of RTI [56, 57]. In RT mixing flow, the velocities are large and the Reynolds number is high [82]. While at such conditions

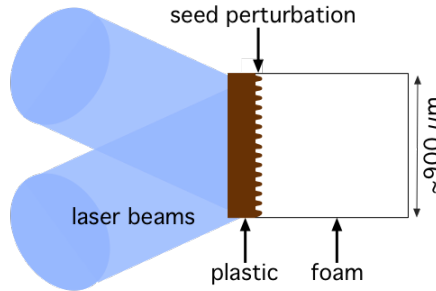


Figure 2.1: Schematic of the laboratory supernova experiment. This illustration shows a side view of the cylindrical experiment tube. The blast wave moves from left to right.

canonical homogeneous turbulence is expected to occur, RT mixing exhibits a significant degree of order [15, 3, 4, 89, 20, 51]. Particularly, it has been observed that at late times when the initial perturbation amplitude increases by ~ 70 times its initial value, the structure of bubbles and spikes remains coherent and its wavelength is set by the initial conditions [56, 57, 37, 82, 81].

Experimental setup

The schematic of supernova experiments is shown in Figure 2.1. The experimental set up is described in detail in [56, 57, 37, 82, 81]. In the experiments a strong laser beam irradiates an initially solid target with two layers of different densities— dense plastic and light foam. The plastic and foam components are encased in $915 \mu\text{m}$ polyimide tube that has $25 \mu\text{m}$ thick walls. The foam piece is $2 - 4 \text{ mm}$ of carbonized resorcinol formaldehyde (CRF) foam with a density of 50 mg/cm^3 , and the plastic component is a $150 \mu\text{m}$ polyimide ($C_{22}H_{10}O_5N_2$) with density of 1.41 g/cm^3 . In the center of the plastic disk there is a strip of doped plastic that acts as a tracer because it is highly opaque to the diagnostic x-rays. The purpose of the strip is to

observe the dynamics at the center of the target free from a potential bias that might be caused by interactions of the laser beam with the target edges. The tracer strip directly abuts the foam layer. At the interface between the materials, a three-dimensional seed perturbation is micro-machined into the plastic piece. The perturbation is periodic in the plane and consists of either a single wave or a superposition of two waves. The single mode perturbation has a $71 \mu m$ wavelength and $5 \mu m$ peak-to-valley amplitude. The two-mode patterns consist of waves with either $212 \mu m$ or $424 \mu m$ wavelength mode superimposed on the $71 \mu m$ wavelength pattern which are called small-two-mode and large-two-mode respectively. Additionally, some experiments are performed with a planar interface [56, 57].

The experiments are conducted at the Omega Laser Facility using multiple shots. In each shot, ten Omega laser beams irradiate the plastic layer of the target. The energy of the $351 nm$ laser beam is $\sim 4.5 kJ$, and the variation in the laser energy is within 5% over multiple shots. Each laser beam passes through a distributed phase plate to give the beam a smooth super Gaussian profile with a full width half maximum diameter $820 \mu m$ [56, 57, 37, 82, 81].

Experimental diagnostics

The main diagnostic of the experiment is x-ray radiography that uses point-projection pinhole backlighting and images the experiment perpendicular to the shock propagation, laser irradiance, and instability growth. An example of an x-ray radiograph is shown in Figure 2.2. In this image, the shock is moving from left to right and it can be seen as the dark curved area on the right. The bright region to the right of the shock is un-shocked foam. The region of alternating light and dark areas is the interface showing the mixing of the plastic and foam materials. The plastic appears dark because it is denser and doped with a material opaque to x-rays. This doped material acts as linear tracers of the flow in space and time. The rarified plastic material is to the left of the tracer strip edge. The dark portion on the far left is diagnostic shielding. For this specific experiment, the target has a single-mode initial perturbation and is observed $21 ns$ after the initial laser pulse [56, 57, 37].

It is important to note that each experiment produces a single image. Images are taken at different times to create a “collage” of the system, as opposed to a “movie” of a single event. It has been assumed that these

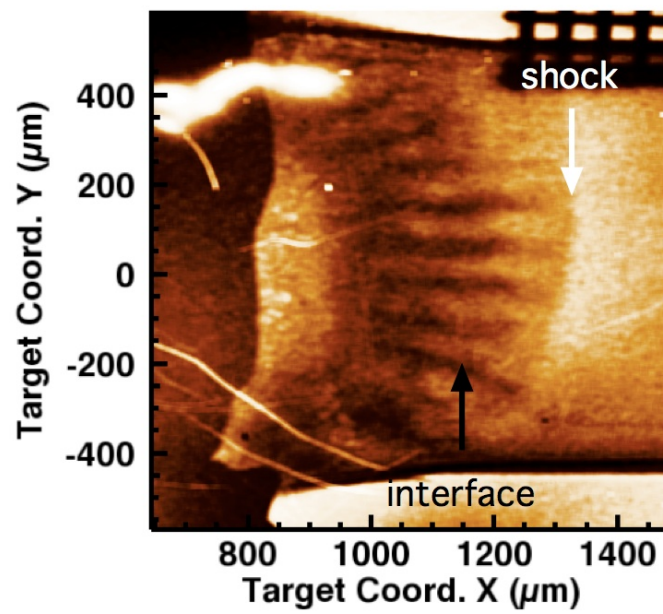
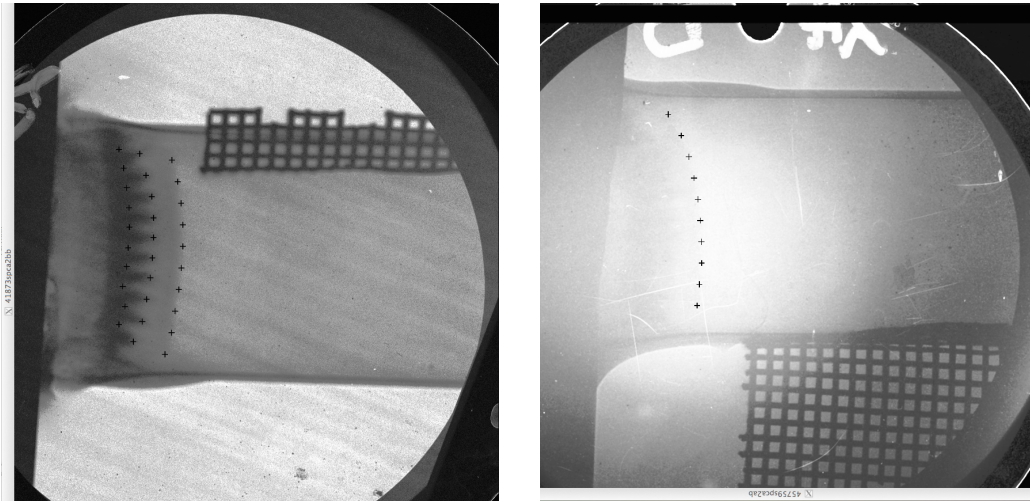


Figure 2.2: Typical x-ray radiograph of an experiment with a single mode interface; image is taken at $21ns$. This image shows the experiment in the same orientation as Figure 2.1.



(a) An example of an image with clear features.

(b) An example of a noisy, low contrast image.

Figure 2.3: Two example radiograph images illustrating measurements and image quality. The shock, bubbles, and spikes all propagate from left to right and the dark grid used for pixel to meter conversion can be seen on the side of the experiment tube. Small crosses mark position measurements analyzed in Chapter 3.

separate snapshots taken of different experiments at different times may be regarded as the time evolution of the same system. We presented quantitative support for this assumption in reference [94] and Chapter 3.

Image processing

We analyze the experimental images by using the Interactive Data Language (IDL) and ImageJ software package for image processing and analysis in Java. As some images show features more clearly than others, we devise a 1-10 ranking system based on the feature clarity, giving better quality images higher scores. Figure 2.3a shows an image with quality rank 9 and Figure 2.3b shows an image with quality rank 3. We confidently analyze 32 out of the 67 available images, discarding images where features are not identifiable.

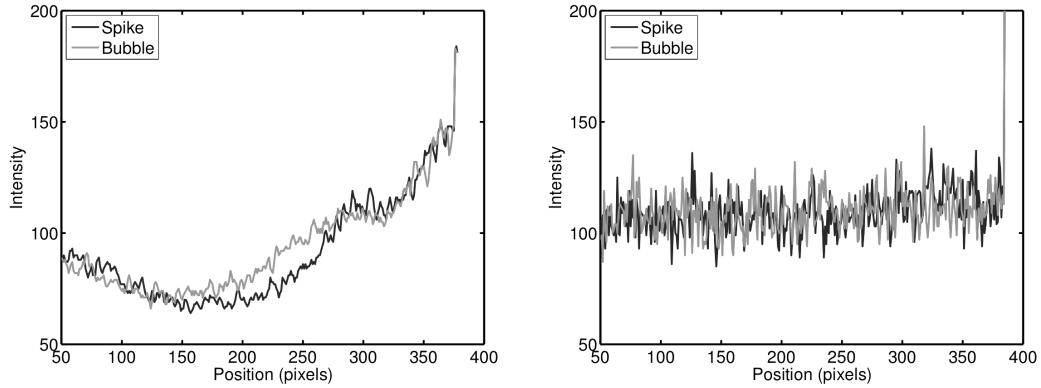
Two types of measurements are obtained from images: the radii of curvature of the interface and the shock front, and the amplitude of the interface. In all images, the shock front and the interface appear curved. We mea-

sure this curvature by fitting a circle to 10 position measurements along the feature. The radius of curvature of the interface is measured from the spike envelope, or the positions of the edges of the spikes. The amplitude of the interface is an important measurement in RTI/RMI. We measure it by finding the length of the spikes. The amplitude of the interface is determined by measuring the distance between the base and tip of the spikes. We are able to measure spikes from images with high feature visibility. 83 spikes were measured from 11 images: 4 images from single mode targets, 3 from small-two-mode targets, and 5 from large-two-mode targets. All the images analyzed for interface amplitude or spike length can be found in the Appendix.

We apply two measurement techniques to observe the amplitude of the interface: a computerized intensity profile method and visual inspection. Although “visual inspection” may sound non-technical in comparison with the computerized intensity profile method, we show that both measurement techniques identify the same quantity. For high quality images, both methods quantitatively measure the same feature. In low quality images the computerized method is affected by noise while the human eye is an impressive instrument that can still identify features of the interface. If an image is very low quality and neither method reliably identifies the amplitude of the interface, then it is eliminated from the data set.

The computerized intensity method measures the pixel intensities in the x-ray image. The intensity profile along a spike is not clear enough to detect features by itself so the pixel intensity along a spike is plotted with the pixel intensity along the neighboring bubble, as in Figures 2.4a and 2.4b. When comparing the bubble and spike intensity profiles, one can discern the positions of the base and tip of the spike.

We measure the amplitude of the interface via visual inspection by using the software ImageJ. Measurable images clearly show the spikes and bubbles, whereas features in the flow bulk cannot be easily determined. To measure the spike amplitudes, first the spike tip and base are identified. Then a line is drawn along the length of the spike. This line acts as a guide so that the measurement stays in the middle of the spike. To measure the tip position, the cursor is placed over the line in the direction normal to shock propagation (across the spike) and the tip of the spike in the direction of the shock propagation (along the spike). The coordinates corresponding to the cursor position from the ImageJ toolbar are recorded. To measure the base position, coordinates are found for the intersection of the middle line of the



(a) For a high quality image, the lines representing intensity along a spike and a neighboring bubble deviate ~ 150 pixels at the base of the spike. They combine at ~ 280 pixels at the tip of the spike. The spike length is ~ 130 pixels.

(b) Fluctuations are large and the bubble and spike intensities do not deviate noticeably for low quality images. In this image, the spike is detectable by visual inspection.

Figure 2.4: Examples of the pixel intensity method performed on high (a) and low (b) quality images.

spike and the line connecting the tips of the two neighboring bubbles. These measurements are analyzed in detail in Chapter 3.

Both the intensity profile method and the visual inspection method is used on five spikes in the image from Figure 2.3a and the measurements are compared. The average difference between the spike amplitude measurements is only 6.4% of the spike amplitude. This small error confirms that both methods are measuring the same feature. Either method appears to be equally accurate for the highest quality images however the computerized intensity profile method is more affected by noisy or grainy images. Figure 2.4a shows the small difference between the spikes and bubbles in one of the clearest images while Figure 2.4b shows the same intensity measurements for low contrast images. On the lower quality image it is not possible to discern the spike and bubble by their pixel intensities. As many images have high noise and low contrast, we chose to use the visual inspection method in order to avoid additional errors from the noisy intensity profile method.

Each experiment includes a wire grid with cell spacing of $6.35 \times 10^{-5} m$ placed next to the tube [55, 37, 82]. Measuring the grid spacing for each

image allows the use physical units of m instead of pixels. For the images used in calculations of the curvature and spike amplitude, the average grid spacing is 55.8 pixels yielding an average conversion factor of $1.13 \times 10^{-6} m$ per pixel. The standard deviation of the conversion factors is 3.90 pixels. Although the spread of conversion factors is small, we calibrate each image individually to avoid this variation.

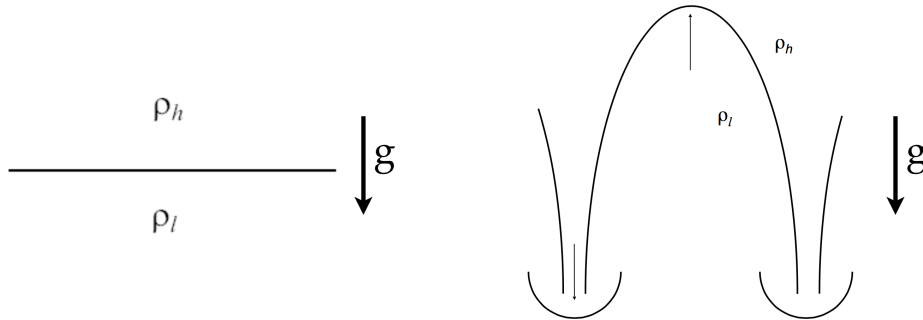


Figure 2.5: Schematic of the interface separating fluids of different densities undergoing RT flow evolution [2]. The spikes of heavy fluid propagating downwards correspond to the dark regions in Figure 2.3 while the bubbles of light fluid propagating upwards correspond to light regions near the interface in Figure 2.3.

2.2 Theoretical Methods

Portions of this section are published in [94]

In this chapter, we survey the theoretical and numerical approaches relevant to Rayleigh-Taylor and Richtmyer Meshkov instabilities. An overview of the field will be briefly discussed followed by a more in depth description of the momentum model and the new regimes studied in this thesis. Detailed description of theoretical methods used to study RTI and RMI can be found in references [1, 2, 4, 5, 6, 7, 8, 9, 10, 3, 15].

2.2.1 Overview

As the RT/RM instability develops, bubbles of light fluid penetrate the heavy fluid and spikes of heavy fluid penetrate the light fluid as demonstrated in Figure 2.5 [4]. RT mixing is a mathematically challenging and intellectually rich theoretical problem. One must account for many demanding requirements because the problem is multi-scale, nonlinear, non-local, and statistically unsteady[1, 2, 4, 5, 6, 7, 8, 9, 10, 3, 15].

RTI dynamics may be described by the nonlinear, compressible Navier Stokes or Euler equations with initial conditions and boundary equations

in the continuous matter approximation [58]. The equations describing the conservation of mass and momentum are

$$\dot{\rho} + \nabla \cdot \rho \mathbf{v} = 0, \quad \rho(\dot{\mathbf{v}} + (\mathbf{v} \cdot \nabla)\mathbf{v} - \mathbf{g}) + \nabla p + \dots = 0 \quad (2.1)$$

where ρ , v , and p are the density, velocity and pressure of the fluid, and the dot indicates a partial time derivative. The unexpressed terms (“...”) include surface tension, viscous stress and other effects which will not be discussed here. Equation 2.1 is supplemented by the initial conditions and boundary conditions for each individual system, as well as the equation for energy transport and the equation of state for compressible fluids. Equations of concentration transport must also be included for miscible fluids [58]. For incompressible, immiscible fluids, the fluid interface is a discontinuity and may be described by the use of the Heaviside step function, H :

$$\rho = \rho_h H(-\theta) + \rho_l H(\theta), \quad \mathbf{v} = \mathbf{v}_h H(-\theta) + \mathbf{v}_l H(\theta) \quad (2.2)$$

where θ is a scalar function on the coordinates and time with $\theta = 0$ corresponding to the interface, ρ_h and v_h are the density and velocity of the heavy fluid in the region, $\theta < 0$ and ρ_l and v_l are the density and velocity of the light fluid in the region, $0 < \theta$ [2, 58]. If no mass flows across the interface, then the pressure and the normal component of velocity are continuous at the interface:

$$p_h|_{\theta=0} = p_l|_{\theta=0}, \quad \mathbf{v}_l \cdot \mathbf{n}|_{\theta=0} = \mathbf{v}_h \cdot \mathbf{n}|_{\theta=0} = -\dot{\theta}/|\nabla\theta| \quad (2.3)$$

where $\mathbf{n} = \nabla\theta/|\nabla\theta|$, the unit vector normal to the interface. For spatially extended fluid systems the flow has no mass sources and can be periodic in the plane normal (x, y) to the direction of gravity (z) ,

$$\mathbf{v}_h|_{z \rightarrow +\infty} = \mathbf{v}_l|_{z \rightarrow -\infty} = 0 \quad (2.4)$$

The governing set of equations is closed with the addition of initial conditions at the interface and boundaries of the domain [77, 30].

In RTI/RMI the system of equations is challenging to solve due to the sharp density gradients, multiple physical processes, nonlinearity, multiple scales, and the ill-posedness of the problem [4]. RT flow is characterized by multiscale structures as well as extensive transports of mass, momentum, and energy across scales [4, 78, 62, 85, 29, 99, 101, 53, 52, 76, 66, 75, 60, 44].

The large scale dynamics of bubbles and spikes is characterized by two length scales: the amplitude of the mixing zone or interface, h in the direction of the acceleration (\mathbf{g}) and the spatial period λ along the plane of the interface [2]. λ , the horizontal scale is introduced by the initial perturbation and/or the mode of fastest growth with wavelength $\sim (\nu^2/g)^{1/3}$, where ν is the kinematic viscosity and $g = |\mathbf{g}|$. The vertical scale is expected to have self-similar growth in the mixing regime with $h \sim gt^2$, and it can be regarded as an integral scale representing cumulative contributions of small-scale structures produced by shear at the interface [4, 5, 8]. If the flow is two-dimensional and the initial perturbation is broad-band and incoherent, then the horizontal scale λ may grow with time [13].

Typically the governing equations are studied in three regimes: linear growth, nonlinear growth, and mixing. For initial perturbations described by a sine wave, the growth rate of the perturbation at small times can be calculated from linear theory. There are several approaches to solve the boundary value problem in the case of nonzero viscosity and surface tension [54]. However, open problems still exist in the linear regime, for example RTI with time dependent acceleration, broad band initial perturbation, and miscible fluids [2]. Standard weakly nonlinear approaches, such as the Ginzburg-Landau equations, do not apply to RTI/RMI. Overall, the core result of linear theories is the presence of a characteristic scale, which is determined by stabilizing effects and can be determined by dimensional analysis [4, 2].

At large times, bubbles and spikes form coherent structures on large scales. In this nonlinear regime, there are rigorous approaches for solving the boundary value problem which account for symmetries and singularities of the dynamics. These approaches originated in references [38, 48, 12] and are reviewed in [2]. In the nonlinear theories, the core result is the multi-scale character, in which both the horizontal and vertical scales contribute to the dynamics.

At late times RT mixing insues due shear between the two fluids of different densities. Shear occurs on the sides of bubbles and spikes flowing past each other and causes vortical structures on small scales. This regime has an extensive history of study that includes interpolation models and turbulence models. Neither method satisfactorily explains the complete set of data from experiments and simulations. The momentum model was developed for the constant acceleration case by accurately incorporating the results of and connecting to nonlinear theory [2], solving the governing equations of the fluid motion. This phenomenological model accounts for fundamental properties

of the governing equations such as symmetries and scale invariance. This momentum model also identified a new invariant value of the flow and showed departure of RT mixing flow properties from canonical Kolmogorov turbulence [51]. Success has been achieved by the momentum model in explaining existing experimental and simulation results and reconciles the earlier interpolation and turbulence models, recreating their results for particular cases [2].

2.2.2 Numerical Methods

Continuous Methods

Simulations of RTI/RMI provide valuable insight into experiments because they are often able to consider multiple physics phenomenon and keep track of many parameters and flow quantities. Simulations may provide valuable insight into parameters that may be difficult to measure experimentally (Section 1.1). Numerical methods used in the field are summarized and the two methods used in this thesis, stochastic and SPH code, are described. Details of the stochastic differential equation solver used can be found in references [5, 6] and the details of the SPH code can be found in references [91, 90, 93]. In this chapter, we briefly describe simulations whose results are used in this thesis, ranging from a simple numerical differential equation solver modeling a noisy drag coefficient to a Lagrangian simulation of a shock wave interacting with a fluid interface.

It is a challenge to model Rayleigh-Taylor and Richtmyer-Meshkov instability because the phenomenon involves multiple scales, sharply changing flow quantities, and is highly sensitive to initial conditions. It is an additional challenge to model Richtmyer-Meshkov instability (RMI) in regimes relevant to high energy density (HED) applications such as supernovae and inertial confinement fusion. One may simplify the problem by neglecting multi-physics effects, however the numerical simulation must still model shocks, accurately account for dissipation processes, and track interfaces [91, 90, 31]. Additionally, since RM dynamics are described by power laws, the flow parameters must be diagnosed with high precision and accuracy in both space and time and must span substantial dynamic range in order to identify the power law exponent [15].

Despite the challenge, using RMI simulation data can be used to analyze experimental results. To date, due to limitations of experimental diagnostics

in supernova experiments, one cannot directly measure the parameters of acceleration driven RTI and RT mixing. Numerical approaches are usually applied to evaluate the acceleration time-dependence and provide benchmarks for experiments [56, 57]. There are two continuous approaches typically used for modeling RTI/RMI. One possible approach is one dimensional hydrodynamic simulations that describe the flow dynamics in the case of an ideally planar interface with account for realistic properties of the fluids. The other approach is a multi-dimensional hydrodynamic simulation describing dynamics of ideal fluids separated by a realistic perturbed interface. Continuous methods are usually applied in selected parameter regimes and require extensive validation and verification. Small scales are not usually resolved in continuous methods; they are better suited to simulating large scale dynamics.

To model the flow dynamics in the case of realistic fluids separated by an ideal unperturbed interface, one-dimensional radiation hydrodynamics code Hyades can be applied [56, 57, 59]. This is a Lagrangian code that models dynamics of a uniform three-temperature fluid. It has a multi-group flux-limited diffusion radiation transport model and approximates the electron heat transport by flux-limited diffusion. The multi-group radiation model allows one to assign energy ranges to multiple photon groups. For each of the photon groups, the opacity is calculated by using an average atomic model. To relate the state variables, the so-called SESAME equations and the state tables are employed. To model supernova experiments, the simulations are set up with the main target components, and the laser energy deposition package is utilized. In the simulations, the nominal value of the laser energy is reduced by $\sim 1/2$ in order to account for the reduction in laser energy absorption for the angled laser beams and the absence of lateral heat transport. The laser energy is then calibrated using the experimental values of the shock and the interface velocity [56, 57].

To model the flow dynamics in the case of ideal fluids separated by a realistic perturbed interface, the multi-dimensional hydrodynamic code FLASH may be applied [56, 57]. This Eulerian finite-difference code is developed to model multi-physics processes in astrophysical applications. The code numerically solves the Euler equations for ideal fluids and applies a variety of modules to capture various physical effects. The code has numerical dissipation and diffusion and does not track the interface. The code employs an adaptive mesh for accurate modeling and efficient computation. To model supernova experiments by FLASH code, simulations are conducted of a two-

dimensional Cartesian flow for the case of two ideal compressible fluids with adiabatic index 1.4. Experimental parameters are used to scale the simulations [56, 57]. Results from Hyades and FLASH codes are used to analyze data from laboratory supernova experiments in Chapter 3.

Particle Methods

Particle methods have different strengths and weaknesses than continuous methods. Particle methods excel at modeling small scales, although modeling longer periods of time is computationally expensive. One successful technique for numerically modeling strong-shock-driven RMI is a Lagrangian approach implemented in the Smooth Partical Hydrodynamics (SPH) code, and its detailed description is found in references [91, 90, 93, 31]. Here we provide a quick overview in this section and use the code in Chapter 5.

SPH represents a fluid via particles in a mesh-free numerical code. SPH particles, which represent the continuous media, consist of mathematical basis functions or kernels that move along the fluid flow. The kernels are cubic B-spline functions resembling Gaussian wave packets. To make up the fluid, the kernels overlap at a diameter equal to the Gaussian width. The equations mathematically describing the SPH particles can be found in reference [91]. These particles can be easily identified in space and time and the contribution of the particle to the flow parameters can be properly weighted. Thus, flow quantities can be summed over all particles in order to compute the conservation of mass, momentum, and energy.

SPH code models fluid flow quantities of each particle including temperature, density, pressure, position, and velocity. Additionally it tracks a quantity called region, which marks particles of different species and tracks material particles. Typically we define the heavy fluid, the bulk of the light fluid, and the light fluid at the interface as three different regions. Examples of these simulated quantities are shown in Figure 2.6. The particle density changes in the region plot in Figure 2.6, demonstrating the adaptive particle size used to capture accurate dynamics while saving computational resources. More, smaller particles are used at the interface where gradients may be stronger and this is seen as darker colors on region plots.

SPH code has limitations, as does any numerical method. For example, one must use artificial viscosity in order to prevent neighboring particles from penetrating one another. Extreme parameter regimes, such as high Mach number or large compressibility are impressively handled without issue,

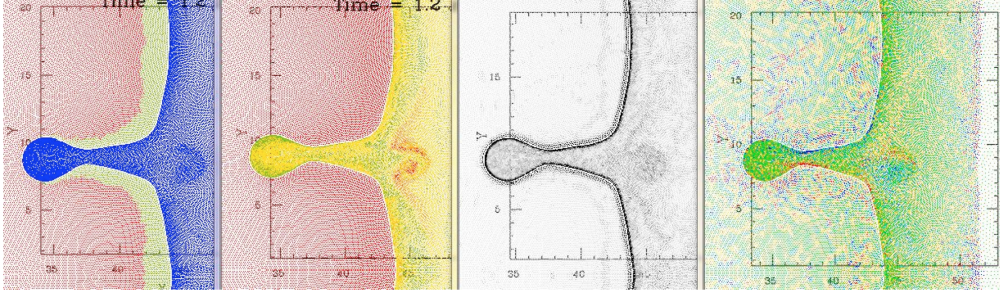


Figure 2.6: Four example plots generated from SPH code simulations of RMI in a two-dimensional domain. In order from left to right, they show region, temperature, density gradient and velocity curl.

although they require larger number of particles and long computational times. In this work, the SPH code appropriately handles numerical problems [93].

2.2.3 Modeling RTI with time dependent accelerations

RTI driven by blast waves and shock waves

In many cases, RTI may be driven by blast waves and shock waves. Theoretical description of these processes requires special consideration outside of the scope of this thesis. Here we give a brief overview of important qualities. More detailed description is found in references [97, 86, 87, 41, 19, 92, 64, 80, 4, 2, 15, 49, 34, 91, 45, 66].

Blast waves are induced by a large energy release in a small volume over a short time [97, 86, 41]. With time the initial burst of energy spreads out; the length scale increases and the velocity decreases. Generally these blast and shock waves are unsteady and the associated acceleration experienced by the fluid is time dependent. In the case of a uniform compressible fluid, the dynamics of blast waves are described by self similar solutions [87, 19]. If a blast wave is driven solely by energy transport, the solution is classified as self-similarity of the first kind [97, 86]. If a blast wave is driven by energy and momentum transport (e.g. by an impact), then the solution has self similarity of the second kind [92, 41]. In the former case, the scaling law is set by the problem dimensionality according to whether the energy is released by a point source, a line source, or a plane source. In the latter case, the

scaling law depends on more complicated processes such as the load history and mass transport at the times of the explosion [87].

The self-similar nature of flow parameters in blast wave driven-RTI motivates our use of power law accelerations in Sections 2.2.4, 3, and 4. The interaction of blast waves with non-uniform density fields and with density discontinuities is a fundamental and, in many regards, open problem that is not addressed in this work.

Richtmyer-Meshkov Instability

Richtmyer-Meshkov instability develops when a steady shock wave is refracted at the interface between fluids of different acoustic impedance (which is proportional to density) [64, 80]. If the shock propagates through an ideally planar interface from the light fluid to the heavy fluid, it splits into a transmitted shock traveling through the heavy fluid and a reflected shock traveling back through the light fluid [103]. For a planar interface, the bulk of the fluids and the fluid interface move together with velocity v_∞ after the shock passage [91, 45, 66]. For initially perturbed interfaces then the interface perturbation grows at a rate v_0 on top of the background velocity, v_∞ due to the impulsive acceleration from the shock (illustrated in Figure 5.1) [64, 80]. The interface evolves into a coherent structure of bubbles and spikes on large scales with the light fluid penetrating the heavy fluid in bubbles and the heavy fluid penetrating the light fluid in spikes [4, 2]. Eventually the bubbles and spikes decelerate after the linear and nonlinear growth. The sides of bubbles and spikes experience shear, producing Kelvin-Helmholtz instabilities on small scales leading to RM mixing. Heterogeneous anisotropic RM mixing is a noisy process with properties distinct from those of canonical turbulence [15, 49, 34].

In RM dynamics, the background motion velocity or velocity of the bulk, v_∞ is an important parameter (Sections 5.2 and 5.4.1). It can be calculated precisely with zero-order theory by using the conservation of mass, momentum, and energy, and the fluids' equations of state [80]. For ideal gases, the background motion is a function of the Mach number M of the shock, the adiabatic indices γ of the fluids, and the Atwood number A describing the density contrast between the two fluids ($A = (\rho_h - \rho_l)/(\rho_h + \rho_l)$) where ρ_h is the density of the heavy fluid and ρ_l is the density of the light fluid) [80]. Depending on the shock Mach number, the background motion may be subsonic or supersonic. In terms of the speed of sound in the light fluid, c_l , v_∞

is subsonic for weak shocks with $M \sim 1$, $v_\infty/c_l \sim 1$ for moderate shocks with $M \sim 3$, and v_∞ is supersonic for strong shocks with $M \gg 1$ [90, 91, 45].

RMI flow consists of this background motion v_∞ in addition to the growth of the interface, v_0 . This compound motion makes it challenging to reliably diagnose the growth of the interface in experiments, since measurements must be taken of a quickly moving region [69, 39]. Simulations however, are not limited by the laboratory rest frame and may use a Galilean transformation to study the interface without considering v_∞ [49, 34, 24]. While this ability to study RMI in a moving frame of reference makes it easy for us to study the interface, it is still important to compare the simulated results to experiments (Section 1.1).

The initial growth rate v_0 is an important measure of RMI because it tells us how the shock interacts and exchanges energy with the interface between the two fluids. For ideal gases, the interface growth (v_0) is a function of M , γ , and A similar to v_∞ , and it also depends on the initial perturbation wavelength, λ and amplitude, a_0 when the initial interface can be described by a single-mode sinusoidal pattern $z^* = a_0 \sin(kx)$ where the wavevector $k = 2\pi/\lambda$, z is the coordinate of the interface in the direction along the shock propagation, and x is the coordinate of the interface in the direction normal to the shock [103].

The initial growth rate can be calculated precisely by linear theory when the initial amplitude is very small ($ka_0 \ll 1$). In this case, the initial growth rate is a linear function of the initial amplitude, as $v_0 \sim Mc_l(ka_0)$ [74, 103, 80]. When the initial amplitude is moderately small, but not very small $ka_0 \ll 1$, then $v_0(ka_0)$ becomes nonlinear with v_0 increasing with (ka_0) slower than linear. A correction factor to the linear initial growth rate has been calculated [98, 74]. For values of (ka_0) greater than 1, v_0 may be even smaller than the predictions of linear and weakly nonlinear theory [91, 39, 46].

At late times of RMI development ($tv_0/\lambda \gg 1$), the incompressible approximation within group theory considerations theoretically describes the dynamics of large scale coherent structures [2, 1, 9]. In the background motion's frame of reference (moving at v_∞), there is no significant fluid motion away far from the interface at late times. The flow at and around the interface is multi-scale, governed by the wavelength and amplitude of the interface, and in the nonlinear stage the RMI bubbles flatten as they decelerate [90, 91, 45]. RM mixing develops at even later stages of RMI evolution ($tv_0/\lambda \rightarrow \infty$). Understanding all the features and dynamics of RM mixing are in many regards, an open problem [15, 49, 66].

In Chapter 5 we compare our empirical model fits of simulation results to results of this theoretical framework. We are interested in understanding the dependence of the initial velocity of the interface on initial conditions such as amplitude of the initial perturbation and initial Mach and Atwood numbers. By using the momentum model and particle simulations, we achieve new results that substantially contribute to research in this field.

2.2.4 Momentum Model

Throughout this thesis we focus on the methods best suited to studying the mixing regime in the case of unsteady accelerations. We analyze data, obtaining as much information as possible from experimental data. We apply the momentum model because of its success describing the RT mixing regime. This phenomenological method analyzes symmetries and scaling properties and is connected to nonlinear analysis based on the group theory approach [15, 4, 2]. It employs novel theoretical concepts, such as invariance of the rate of momentum loss, and successfully describes experimental results.

The analysis finds that an imbalance in the momentum is necessary for RT mixing to accelerate, strong accelerations may lead to flow laminarization, RT mixing can exhibit order, and RT mixing has a set of invariant measures [15, 4, 2]. This model identifies new fundamental properties of RT mixing that can lead to better understanding and control of RT dynamics. In limiting cases the momentum model reproduces the results of other interpolation and turbulence models [11, 73, 34, 35, 40, 72, 21]. Here we expand the analysis by investigating two regimes with distinct asymptotic solutions. Only brief overview of the momentum model as it pertains to its use in this thesis is provided. More detailed information is discussed in references [1, 2, 4, 5, 6, 7, 8, 9, 10, 3, 15]

RT mixing in supernova explosions and inertial confinement fusion is driven by a blast wave [102, 17]. The hydrodynamics of blast waves in incompressible fluids is described by self-similar solutions [87, 19]. The scaling law can depend on the load history and mass transport or the problem dimensionality, depending on how the energy is deposited [97, 86, 92, 41]. Considering these two important applications of RT mixing and wanting the solutions to remain generally applicable, we use accelerations in the form of power laws.

Overview

Unlike Kolmogorov turbulence, RT mixing does not have an invariant energy dissipation rate; energy may not characterize the flow in RT mixing as well as momentum [4]. In RT flows, the transport of momentum can be found from the spatial distribution of the velocity and density fields [2]. We apply theoretical analysis considering symmetries and momentum transport in RT flow to analyze the dynamics in the case of time-dependent acceleration [4, 3, 2, 10, 8]. We describe RT flows by balancing the rates of gain and loss of specific momentum. The dynamics of a small parcel of fluid undergoing RT mixing is governed by the rate of momentum gain per unit mass, $\tilde{\mu}$ balanced with the rate of momentum loss per unit mass, μ . The basic governing equations are

$$\dot{h} = v, \quad \dot{v} = \tilde{\mu} - \mu \quad (2.5)$$

where h is the vertical length scale (i.e. amplitude, the vertical size of the right side of Figure 2.5), v is the corresponding velocity, $\tilde{\mu}$ and μ are the magnitudes of the momentum loss and gain in the vertical direction (along the acceleration \mathbf{g}), and dot indicates a partial time derivative. On the basis of dimensional analysis, the rates of specific momentum gain and loss can be rewritten in terms of the rates of gain and loss of specific energy, $\tilde{\epsilon}$ and ϵ as $\tilde{\mu} = \tilde{\epsilon}/v$ and $\mu = \epsilon/v$ [4, 3, 2, 10, 8]. Equation 2.5 is a simplified, dimensional model of the system of equations 2.1-2.4 which represents the conservation of mass and momentum [2]. Further consideration of symmetries and invariants of RT dynamics is discussed in references [15, 4, 8].

One can find asymptotic solutions for Equation 2.5 and investigate the properties of RT mixing by considering $\tilde{\mu} = gf$ (where factor f depends on the density ratio and $g = \|\mathbf{g}\|$ is rescaled hereafter as $gf \rightarrow g$), and by using $\epsilon = Cv^3/L$ for the drag term, where L is the characteristic length scale for energy dissipation and C is a finite constant representing the drag coefficient. Equation 2.5 is analogous to Equation 2.1, where $\dot{h} = v$ is an analog of the conservation of mass and $\dot{v} = \tilde{\mu} - \mu$ is an analog of the conservation of momentum. This becomes apparent when ∇ is considered as $\sim 1/\text{length}$. Evaluation of order and scaling in RT mixing flow is made possible by considering invariants and symmetries in the problem [15, 3]. Throughout this thesis, we analyze dimensionless asymptotic solutions for $t/t_0 \gg 1$ and $h/h_0 \gg 1$ where t_0 is the characteristic time scale and h_0 is some initial value with an initial velocity $v_0 \sim h_0/t_0$.

Generally the acceleration, g , can be constant or time dependent. The case of constant acceleration has been studied previously both with and without accounting for turbulent diffusion [8]. In this work, we focus on the time dependent case. In particular we consider $g(t)$ as a power law in time in order for our results to be applicable to experiments relating to inertial confinement fusion and supernova explosions which are driven by blast waves and therefore have accelerations with power law time dependence.

We analyze asymptotic solutions for acceleration with power law time dependence, $g = g(t) = At^a$, where parameter A is a positive constant and its dimensions are $[A] = m/s^{(2+a)}$. The characteristic length scale for energy dissipation can be vertical ($L \sim h$, the amplitude), horizontal ($L \sim \lambda$, the wavelength), or a combinations of these two scales. If the characteristic scale for energy dissipation is a combination of scales, ($L \sim t^\beta$, where $0 < \beta < b$), or if the characteristic length scale for energy dissipation is horizontal ($L \sim \lambda$, $\lambda = \text{constant}$) then a dominant asymptotic solution with power-law time dependence can be found for certain ranges of the acceleration exponent, a . We look at asymptotic solutions of the form $h = Bt^b$. For physical relevance, we impose the conditions $B > 0$ and $b > 0$ to ensure that the interface amplitude and the growth of the interface are positive.

Analysis of the asymptotic solutions for Equation 2.5 allows one to consider possible mechanisms of transition from nonlinear to mixing regime in RT flows by comparing the cases of $L \sim \lambda$ and $L \sim h$ [Tables 2.2 and 2.3]. In the case of time dependent acceleration with $g(t) = At^a$, a transition may occur (similar to the case of constant acceleration) from the nonlinear to the mixing regime with the horizontal scale increasing with time [4, 8]. This phenomenon, sometimes called bubble merger, is considered by some to be necessary for the development of RT mixing and growth of the interface. However, the growth of the horizontal scale, while possible, is not a necessary condition for RT mixing to develop. Similar to the case of constant acceleration, RT mixing develops due to an imbalance of the rates of gain and loss of specific momentum in the case of time dependent acceleration and a vertical scale being the characteristic scale for energy dissipation [15, 4, 8].

In Equation 2.5, if the characteristic scale for energy dissipation is a combination of scales, and it is a power law function of time with $L \sim t^\beta$, where $0 < \beta < b$, then dominant asymptotic solution with power law time dependence, $h = Bt^b$ has exponent $b = a + 2$ for $0 < \beta < (a+2)/2$, and $b = \beta + (a+2)/2$ for $\beta > (a+2)/2$ and $a > -2$. The asymptotic solutions for the combination case are summarized in Table 2.1.

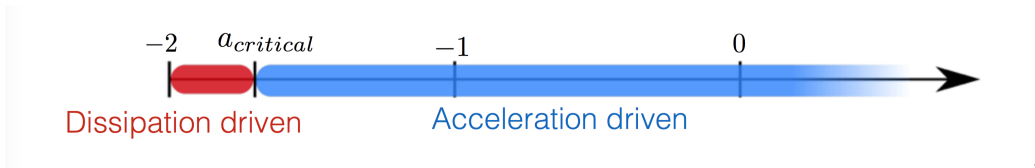


Figure 2.7: Diagram of mixing regime. The dissipation dominated mixing regime (red) is analogous to RM-type mixing while the acceleration dominated mixing regime (blue) is analogous to RT-type mixing

If the characteristic length scale for energy dissipation in Equation 2.5 is horizontal, $L \sim \lambda$, and λ is a constant, then for the acceleration exponent, $a > -2$ the asymptotic solution has the form $h = Bt^b$ with exponent $b = (a+2)/2$ and prefactor $B = \sqrt{\frac{A\lambda}{C((a+2)/2)^2}}$. When the exponent $a = -2$ the asymptotic solution is logarithmic in time, $h \sim \lambda \ln(t/t_0)$. For the acceleration exponent below -2, no power law asymptotic solutions $h = Bt^b$ exist with $B, b > 0$. We call the regime when $L \sim \lambda$ the nonlinear regime, by analogy with RTI with constant and impulsive accelerations. The asymptotic solutions for the nonlinear regime are summarized in Table 2.2.

In this work we focus our discussion on the mixing regime. We summarize and expand upon previous studies of the $L = h$ case, analyzing larger ranges of the acceleration exponent and describing two different regimes.

Asymptotic solutions of the form $h = Bt^b$ can be obtained when the characteristic length scale for energy dissipation is $L \sim h$, the amplitude. The exponent b and the prefactor B are identified from Equation 2.5 and have dimensions $[b] = 1$ and $[B] = m/s^b$. Depending on the value of the acceleration exponent different solutions exist. A critical value of the acceleration exponent divides the solutions into two regimes as illustrated in Figure 2.7. By analogy with the constant acceleration case, the regime corresponding to the range of a values above the critical value is called acceleration dominated mixing. In acceleration dominated mixing, the acceleration, g is significant and contributes to the dynamics. The regime corresponding to a values below the critical value is called dissipation dominated mixing as the dissipation or drag term plays a more significant role. If the acceleration exponent a is in the range $a < -2$, then no power-law asymptotic solutions $h = Bt^b$ with $B > 0$ and $b > 0$ exist. The various asymptotic solutions for each regime are summarized in Table 2.3.

Range of a	Range of β	Solution for h
$-2 < a$	$0 < \beta < (a+2)/2$	$h = Bt^b$ with $b = a + 2$
$-2 < a$	$\beta > (a+2)/2$	$h = Bt^b$ with $b = \beta + (a+2)/2$

Table 2.1: Asymptotic solutions of the momentum model for the combination case, $L \sim t^\beta$.

Range of a	Solution for h
$-2 < a$	$h = Bt^b$ with $b = 1 + a/2$ and $B = \sqrt{\frac{A\lambda}{C(1+a/2)^2}}$
$a = -2$	$h \sim \lambda \ln(t/\tau)$

Table 2.2: Asymptotic solutions of the momentum model for the nonlinear regime, $L = \lambda$.

Range of a	Solution for b	Solution for B	Sign of \dot{v}
$-1 < a$	$b = a + 2$	$B = A/(a+2)((a+1)+C(a+2))$	$\dot{v} > 0$
$a_{critical} < a < -1$	$b = a + 2$	$B = A/(a+2)((a+1)+C(a+2))$	$\dot{v} < 0$
$-2 < a < a_{critical}$	$b = (1 + C)^{-1}$	$B > 0$	$\dot{v} < 0$

Table 2.3: Asymptotic solutions of the momentum model for the mixing regime, $L = h$. Note that $a_{critical} = -2 + (1 + C)^{-1}$.

Acceleration dominated mixing

If the acceleration $g(t) = At^a$ has the exponent $a > -2 + (1 + C)^{-1}$, then the dominant asymptotic solution has exponent $b = a + 2$ and prefactor $B = A/[(a+2)((a+1)+C(a+2))]$. It is important to note that depending on the value of a within this range, the effective acceleration of the interface can be positive ($\dot{v} > 0$ for $a > -1$) or negative ($\dot{v} < 0$ for $-2 + (1 + C)^{-1} < a < -1$). Also note that while the prefactor has some dependence on the drag coefficient, the exponent only depends on the acceleration exponent. According to the theory, the exponent of the power law describing the interface should be a constant.

This subregime also contains the special case of a steady state solution. When $a = -1$, the time derivative of the interface amplitude is a constant and $\dot{v} = 0$. This steady state case is analogous to the $L \sim \lambda$, constant acceleration case, in which nonlinear RTI grows as $h \sim t\sqrt{g\lambda}$ with constant velocity [4, 97]. The rates of momentum gain and loss is necessarily balanced in order for $\dot{v} = 0$. In Section 4.2.6 we use the steady state solution in the mixing regime to study stochastic effects with minimal time dependent dynamics.

Dissipation dominated mixing

If the acceleration exponent a is in the interval $-2 < a < -2 + (1 + C)^{-1}$, then the dominant asymptotic solution has exponent $b = (1 + C)^{-1}$ and the prefactor is a positive free parameter. We call this regime dissipation dominated mixing. The acceleration of the interface is negative for all the acceleration exponents in the dissipation dominated mixing regime ($\dot{v} < 0$ for $-2 < a < -2 + (1 + C)^{-1}$). It is important to note that the exponent depends on C and is independent of a unlike the acceleration dominated mixing regime. Note that the prefactor is only determined by initial conditions and we are unable to control it or compare it with flow quantities.

2.2.5 Stochastic Model

Detailed discussion about stochasticity in RTI and RT mixing can be found in references [2, 5, 6]. RT mixing is a turbulent phenomenon whose dissipation process has a random character [5, 6]. To study stochastic effects in RT mixing in Chapter 4, the momentum model is extended by modeling the drag

coefficient as a stochastic quantity. In particular, the drag coefficient, C is a stochastic quantity, leading to a fluctuating rate of momentum loss. To model this, we must use a stochastic differential equation in addition to Equation 2.5 and the equations must be expressed in differential form. Equation 2.5 is rewritten in differential form and appended by a third equation describing the evolution of the drag coefficient. The set of equations governing RT mixing with a stochastic dissipation process is

$$\begin{aligned} dh &= vdt, & dv &= gdt - \frac{Cv^2}{h}dt, \\ dC &= -C \ln\left(\frac{C}{\langle C \rangle} - \frac{\sigma^2}{2}\right) \frac{dt}{\tau_C} + \sigma_C \sqrt{\frac{2}{\tau_C}} dW \end{aligned} \quad (2.6)$$

where $\langle C \rangle$ is the average value of C , σ is the standard deviation of C , τ_C is the characteristic time scale of dissipation, and dW is the standard Wiener process. C is a stochastic process that is, in general, time dependent. The drag coefficient is described with a log normal distribution plus a standard Wiener process. A log normal distribution was chosen because RT mixing fluctuations are known to have long-tail distributions [5, 6]. We use a log normal distribution which is asymmetric: $\langle C \rangle \neq C_{max}$ with values $\langle C \rangle = C_0 e^{-\sigma^2/2}$ and $C_{max} = C_0 e^{-\sigma^2}$. A characteristic time scale τ_C describes how quickly the distribution of C approaches a stationary probability density function (the Wiener process). The probability density function is characterized by the mean value, $\langle C \rangle$, the largest value, C_{max} , and the standard deviation, σ . In this study, we use $\sigma = 0.5\langle C \rangle$ for all cases.

Examples of the simulated time evolution of C are seen in Figure 2.8. To study the system described by the momentum model with time-dependent accelerations, we numerically solve the set of differential equations shown in Equation 2.6 using a numerical differential equation solver with multiplicative noise in C++. A power law acceleration is assumed and then information about the time evolution of the drag coefficient, the amplitude of the interface, and the velocity of the interface are obtained for various values of the acceleration exponent. In order to accurately determine the power law solutions we model 1000 trajectories over six decades of time for each set of parameters. The modeled values of the acceleration and drag coefficient are output as diagnostics and the solution for the amplitude of the interface and its growth rate are output for analysis.

Detailed discussion of the model and code overviewed in this section can be found in references [5, 6]. Using a numerical differential equation solver

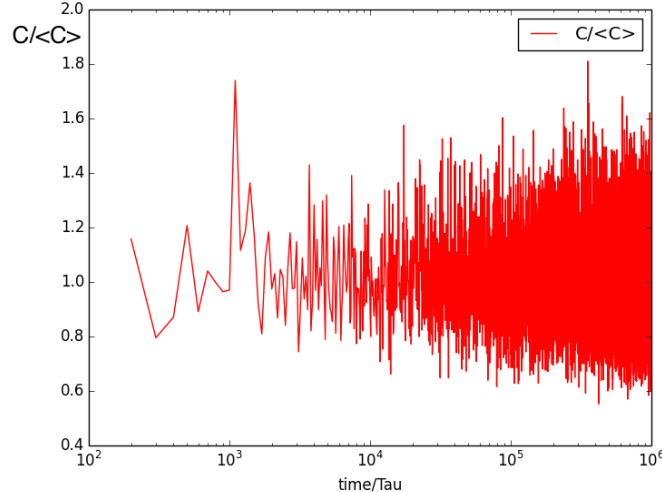


Figure 2.8: Stochastically modeled time evolution of $C(t)$ normalized by its average value, $\langle C \rangle$.

with multiplicative noise in C++, we numerically solve the governing equations with the acceleration modeled as a power law and the drag coefficient modeled as a statistical process with a lognormal distribution [5, 6]. In order to accurately determine the power law solutions we model 1000 trajectories over six decades of time for each set of parameters. The modeled values of the acceleration and drag coefficient are output as diagnostics and the solution for the amplitude of the interface and its growth rate are output for analysis.

The stochastic code models Equation 2.6 for n_v trajectories. At each time step, it outputs the drag coefficient C , the interface amplitude h , and its time derivative v , each averaged over all modeled trajectories. In this work, power law accelerations of the form $g(t) = At^a$ are simulated.

The time range t , total number of time steps N_t , acceleration exponent a , mean drag coefficient $\langle C \rangle$, and number of trajectories n_v are adjustable inputs. Typically in this thesis we use a time range of $t = 10^5$ or 10^6 seconds and $N_t = t \times 10^3$ time steps. The number of trajectories is $n_v = 10^3$, with the exception of Section 4.2.6 which analyzes the stochastic model data for $n_v = 1$. The acceleration exponent is varied from $a = -2$ to $a = 0$.

Chapter 3

Data analysis of laboratory supernova experiments

Portions of this chapter are published in [94]

3.1 Introduction

RTI plays an important role in the study of high energy density plasmas (HEDP) in inertial confinement fusion and supernova explosions. These phenomena present a challenging topic of study because material dynamics are characterized by high energy density, sharply and rapidly changing flow fields, and small effect of dissipation and diffusion; in these instances RTI presents in a very fast and strong system. Here, we report a thorough analysis of experimental data in supernova experiments conducted at high powered laser facilities [56, 57, 37, 82, 81]. We evaluate what information experiments and simulations may tell us about the fundamentals of RTI and RT mixing in HEDP by comparing the data with rigorous theoretical approaches.

Supernova experiments are designed to mimic the evolution of supernova SN1987A at high powered laser facilities such as the Omega Laser Facility and the National Ignition Facility in order to study the astronomical system in a controlled environment [79]. SN1987A is a type II core-collapse supernova and its progenitor star has a layered structure. During the star's explosion, a blast wave propagates from the center of the star outwards through layers of material with progressively decreasing density [102, 17]. The gradients of the pressure and density fields point in opposite directions in the star's inte-

rior, leading to RTI. The outer and inner stellar layers experience extensive interfacial mixing and it is believed that during the supernova explosion, RT mixing may provide special conditions for the generation of elements with heavy atomic mass and thus may explain the abundance of these elements in the universe [17].

A core-collapse supernova is characterized by high energy density [104]. The values of energy density are somewhat similar in the laser experiments [79, 84, 22]. In addition, both supernova and laboratory hydrodynamics can be regarded as self-similar and Eulerian at continuous scales because the effects of dissipation and diffusion are usually small, and so are the characteristic scales on which dissipation and diffusion occur [71, 20, 51]. This suggests that if the parameters are properly scaled, astrophysical processes can be mimicked and studied in a well-controlled laboratory experiment at high powered laser facilities [84]. Requirements for the systems to achieve such hydrodynamic similarity include the need for collisional thermodynamics accompanied by negligible heat conduction and radiation flux as well as insignificant viscous dissipation. With these conditions in mind, experiments are designed to investigate the interaction of a blast wave with a helium-hydrogen interface in supernova SN1987A [37, 82, 81]. While in realistic laboratory environments the characteristic scales are small ($\sim \mu m$ and $\sim ns$), one may achieve the astrophysical values of energy density by varying the power and time duration of the laser beam and the properties of the target [36, 84, 79, 22].

For example, in supernova SN1987A at time $\sim 2000 s$, the characteristic values are estimated as $\sim 9 \times 10^8 m$ for length, $\sim 2 \times 10^5 m/s$ for velocity, $\sim 7.5 kg/m^3$ for density, and $\sim 3.5 \times 10^{12} Pa$ for pressure. In the first HEDP laboratory experiments in Cu plasma at time $\sim 20 ns$ the corresponding values are $\sim 5.3 \times 10^{-5} m$, $\sim 1.3 \times 10^3 m/s$, $\sim 4.2 \times 10^3 kg/m^3$, and $\sim 6 \times 10^{10} Pa$ [79, 84]. According to the Braginski model, one can further evaluate the Reynolds and Peclet numbers in supernova SN1987A to be $Re \sim 2.6 \times 10^{10}$ and $Pe \sim 2.6 \times 10^5$ while in HEDP laboratory experiments, $Re \sim 1.9 \times 10^6$ and $Pe \sim 1.8 \times 10^3$ [84, 23]. Remarkably, the Euler number is ~ 0.29 in supernova SN1987A and ~ 0.34 in laboratory experiments. The Euler number is defined as the product of the velocity and the square root of the ratio of the density and pressure. This suggests that the Euler number (or the energy density) is the proper dimensionless scaling parameter for imitating and studying the astrophysical phenomena in laboratory experiments [79, 84]. High powered laser facilities are necessary to achieve experiments with such

parameters. Scrupulous analysis of the invaluable experimental data is in demand.

The evolution of core-collapse SN1987A is believed to be driven by a blast wave [102, 17]. Blast waves are induced by a large energy release in a small volume over a short time [97, 86, 41]. Blast wave solutions are self similar and may be described by power laws. It is an experimental challenge to generate shocks and blast wave with prescribed properties in high powered laser facilities [79, 82, 81]. The laser beams concentrate a large amount of energy onto a small target in a short amount of time [56, 57, 37], causing a large energy release in a small volume over a short time. The laser irradiation ablates the outer part of the target and plasma is created, also creating a blast wave due to the ablation pressure. More details of how blast waves are created in laboratory supernova experiments is provided in Section 2.2.3. It is believed that the resulting dynamics of the fluid flow is similar to that driven by a blast wave [56, 57].

In supernova experiments, due to complex processes induced by the laser radiation, the acceleration is directed from the denser to the lighter fluid, causing the development of RTI [56, 57]. In RT mixing flow, the velocities are large and the Reynolds number is high [82]. While at such conditions canonical homogeneous turbulence is expected to occur, RT mixing exhibits a significant degree of order [15, 71, 4, 89, 20, 51]. Particularly, it has been observed that at late times when the initial perturbation amplitude increases by ~ 70 times its initial value, the structure of bubbles and spikes remains coherent and its wavelength is set by the initial conditions [56, 57, 37, 82, 81].

The ordered character of RT mixing has been discovered within the framework of rigorous theoretical analysis considering symmetries and momentum transport in RT flow [71, 4, 2], Section 2.2.4. The analysis finds that RT mixing has a new set of invariants leading to stronger correlations, steeper spectra, and weaker fluctuations when compared to canonical turbulence [15, 71, 4, 8]. In addition to explaining experiments in plasmas, the analysis has also agreed with experiments in fluids suggesting that a strong acceleration may laminarize the flow [88, 67, 65, 68, 70, 96].

In this work, we further investigate what experiments may tell us about the fundamentals of RT dynamics in high energy density regime by conducting scrupulous data analysis of supernova experiments. Previous data studies in these systems involved measurements of some single selected spikes [56, 57]. Herein, we analyze all viable structures in all available experimental x-ray images of the flow that are taken at late stages of RT mixing evolution.

We process the experimental images by using visual and computerized images techniques, and by measuring delicate features of the interface in order to determine the curvature and amplitude of the interface. A new scaling is identified for calibration of experimental data to enable accurate analysis and comparisons. The curvature of the interface (which is observed in all images) is shown to remain constant (within the noise level), which allows us to expand the data set size and statistics. New theoretical solutions are reported to describe asymptotic dynamics of RT mixing with time-dependent acceleration. The data are in good quantitative agreement with the theoretical analysis. Our results enable the development of new approaches for the rational design of experiments and simulations of RTI and RT mixing in HEDP.

The experimental set up and diagnostic methods of laboratory supernova experiments are described in Section 2.1.2. An overview of the numerical methods discussed here is given in Section 2.2.2 and theoretical details are shown in Section 2.2.4. The results of the Hyades and FLASH numerical simulations are discussed in detail in [56, 57]. For the purposes of this chapter, the simulations provide the exponents of the power-law functions of time of the interface position and the acceleration. According to Hyades simulations, when considering the same time interval as the experiments, the position of the planar interface can be described as a power law function of time with exponent 0.6. According to FLASH simulations, the acceleration in the hydrodynamic system can be described as a power law function of time with exponent -1.1 during the time interval of the experiments [56, 57].

3.2 Experimental results

3.2.1 Scaling of experimental measurements

When analyzing experimental data, it is important to obtain measurements that are consistent with each other and that are comparable with other studies. It is particularly important in data analysis of the supernova experiments, which record a collage of images of different events as opposed to a movie of a single event [Section 2.1.2]. In order to draw consistent conclusions, measurements from these separate images must be scaled by a single characteristic value. A good characteristic scaling must be robust, must depend on experimental parameters that are easily controlled and accurately

measurable, and must provide reasonable values, Section 1.1 [58, 26].

Supernova experiments result from the interplay of complex physical processes at extreme conditions of high energy density. The outcome of these experiments is represented by x-ray images whose analysis yields the linear tracers of the flow in space and time. To analyze the data, a time-scale and a length-scale of the hydrodynamic system should be identified.

Traditionally, data in supernova experiments are presented in SI units because the standard calibration values are time-dependent and are not directly diagnosed. It is a challenge to find a time scaling when the measurable parameters with time units are also time-dependent. Even though no quantities with time units are constant in supernova experiments, we obtain a characteristic time scale in the hydrodynamic system by applying the well-known initial conditions and experimental parameters with low fluctuations.

In supernova experiments, the laser energy is $E_0 \sim 4.5 \text{ kJ}$, the diameter of the laser spot is $\sim 8.2 \times 10^{-4} \text{ m}$, and the laser shot duration time is $\sim 1 \times 10^{-9} \text{ s}$. This produces a laser irradiance the target (the laser energy per unit time that is deposited to the target per unit area) of $I_0 \sim 8.5 \times 10^{18} \text{ W/m}^2$, Table 3.1. This value is well known and fluctuates less than 5% across all experiments. The other well-controlled experimental quantity is the total mass of the plastic piece of the target. The plastic piece of the target is a disk with density 1.41 kg/m^3 , a diameter of $9.05 \times 10^{-4} \text{ m}$ and a width of $1.50 \times 10^{-4} \text{ m}$. The volume and the density provide the total mass of $m \sim 1.36 \times 10^{-7} \text{ kg}$, and this value varies by 1% or less between experiments. The combination of the total mass divided by the laser irradiance raised to the power $1/3$ provides units of seconds, as $\tau = (m/I_0)^{1/3}$. The characteristic time τ given by this combination is $\tau = 2.74 \text{ ns}$. Remarkably, the overall run time T in the experiment is usually $2.5 \times 10^{-8} \text{ s}$ leading to $T/\tau \approx 9.2$. Therefore, the time scale τ is robust; it varies very little between experiments. It depends on easily controlled parameters; the laser power is well known and the targets are precision machined. It provides a reasonable value; it is the same order of magnitude as the measurements. This new time scaling meets the criteria for a good characteristic value [Section 1.1].

In our data analysis study, all position or distance measurements are scaled by the perturbation wavelength $\lambda = 71 \mu\text{m} = 7.1 \times 10^{-5} \text{ m}$. The perturbation wavelength is a standard scaling which also fits the criteria of being robust, controlled, and a reasonable value [Section 1.1].

To further justify the use of (λ, τ) -based scaling for data analysis, to reveal the presence of acceleration in the fluid system, and to determine

Quantity	Expression	Value
Laser energy	E_0	4.5 kJ
Laser irradiance	I_0	$8.5 \times 10^{18} \text{ W/m}^2$
Target mass	m	$1.36 \times 10^{-7} \text{ kg}$
Length	λ	$7.1 \times 10^{-5} \text{ m}$
Time	$\tau = (m/I_0)^{1/3}$	$2.73 \times 10^{-9} \text{ s}$
Acceleration	λ/τ^2	$9.5 \times 10^{12} \text{ m/s}^2$
Specific kinetic energy	$(\lambda/\tau)^2$	$6.7 \times 10^8 \text{ J/kg}$
Specific total energy	E_0/m	$2.59 \times 10^{10} \text{ J/kg}$
Energy ratio	$(\lambda/\tau)^2/(E_0/m)$	$1.36 \times 10^{-7} \text{ kg}$

Table 3.1: Scaling parameters and characteristic values of quantities of RT dynamics based on τ and λ , the characteristic scales in experiments [94].

possible length scale for energy dissipation in RT mixing flow, we perform a coarse comparison of the overall run-time of the experiments $T/\tau \sim 9.15$ to the overall growth of the amplitude $H/a_0 \sim 70$ and $H/\lambda \sim 5$, where H is the “final” amplitude of the interface, and $a_0 = 5\mu\text{m}$ is the peak-to-valley initial perturbation amplitude. This comparison suggests that $(H/a_0) \sim (T/\tau)^{1.9}$ and $H/\lambda \sim (T/\tau)^{0.72}$ implying that in supernova experiments the (λ, τ) -based scaling is reasonable, the RT flow may indeed accelerate, and the amplitude may serve as a scale for energy dissipation.

Table 3.1 gives the values of the scaling parameters and the characteristic values they produce. This scaling is presented for the first time, to the author’s knowledge. In particular, this scaling allows us to evaluate in supernova experiments the characteristic value of acceleration as $\lambda/\tau^2 \sim 9.5 \times 10^{12} \text{ m/s}^2$, and the specific kinetic energy as $(\lambda/\tau)^2 \sim 6.7 \times 10^8 \text{ J/kg}$. By combining these values with the value of the Reynolds number $Re \sim 10^6$ [79], we evaluate the acceleration-set viscous scale of RT mixing dynamics as $\sim \lambda Re^{-2/3}$ and $\lambda Re^{-2/3} \sim 10^{-8} \text{ m}$ [71, 26], which is substantially smaller than the length scale λ .

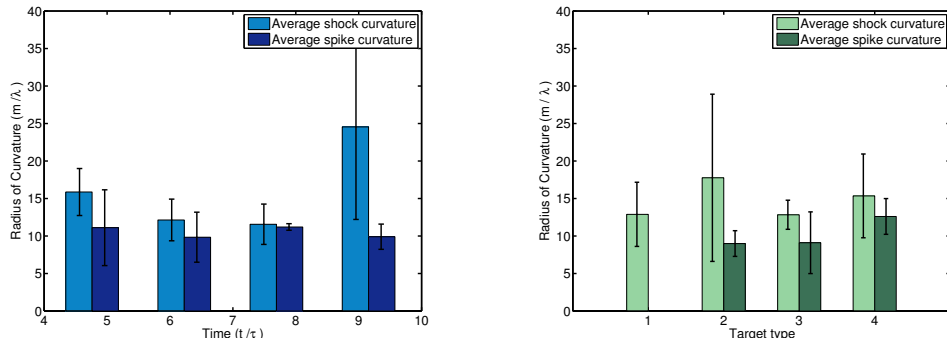
3.2.2 Curvature of the shock front and interface envelope

In images from supernova experiments, all of the shock fronts and the interface envelopes qualitatively appear to be curved [56, 57, 37, 82, 81]. The cause of this curvature is unknown. Possible causes may include three-dimensional departures of shocks and rarefaction waves from their ideal planar shape, strong coupling of scales in RT mixing flow, and the imprint of the experimental conditions such as the laser intensity profile.

While the curvature of shock fronts and interface envelopes is a common phenomenon in HEDP experiments, to date, no systematic studies of the phenomenon are conducted. Reliable quantification of the curvature dependence on the parameters of HEDP experiments requires in-depth understanding of such fundamental and challenging problems as light-material interaction at microscopic scales, interaction of plasma flow with boundaries at meso-scales, and interaction of shocks and rarefaction waves with non-uniform flow fields and the effect of the finite size of the target at macroscopic scales. In this work, as is required by the scientific method, we undertake the first step to understand the phenomenon: we measure it.

The details of the curvature measurement are given in Section 2.1.2. We measure the radius of curvature of the shock front as well as the interface envelope. We further look at the effects of time and different target types (planar, single mode, and two modes) on the radii of curvature. Experimental images from four time steps (13, 17, 21, and 25 ns) and four target types (planar, single mode, small-two-mode, and large-two-mode) are analyzed. Figure 3.1a represents the overall time evolution by taking averages over target type. Figure 3.1b represents the effect of target type by taking averages over time. It is remarkable that while in some cases the error bar can be substantial, the curvatures across both plots are essentially constant. This is true for both spike and shock curvatures. The mean value of the radius of curvature R for spikes is $(R/\lambda) \sim 10.3$ with $(R^{2\pi/\lambda}) \sim 64.7$ and for shocks is $(R/\lambda) \sim 14.4$ with $(R^{2\pi/\lambda}) \sim 90.5$. According to the experimental data the radius of curvature neither increases nor decreases, suggesting that the curvature may be an imprint of the experimental conditions.

Several experimental conditions may contribute to the curvature. The laser has a super-Gaussian intensity profile, causing slightly higher pressure near the center of the target. This and the finite size of the target may cause the shocks, rarefaction waves, and the interface envelopes to deviate away



(a) Radii of curvature of shock and spikes for experimental images from all target types plotted with respect to time.

(b) Radii from all times plotted versus target type. In order, the target types are planar, single-mode, small-two-mode, and large-two-mode.

Figure 3.1: Analysis of the radius of curvature; error bars indicate standard deviations. [94]

from a planar shape. Furthermore, some new specific modes may be induced as an effect of the finite size of the target. Since the curvature does not change in time, this indicates that spikes may grow in the same manner as neighboring spikes in the same image. If the curvature is indeed imprinted by the initial experimental conditions, then the system evolves straight along the tube with the pre-determined geometry. This suggests that we can treat the spikes individually and thus improve our statistics for spike length analysis. From scrupulous measurements that are described in Section 2.1.2, we observe that in the same image the spike length varies only slightly, within 6% – 10%, thus supporting our hypothesis on the curvature effect being an imprint of the experimental conditions. It is worth noting also that averaging the radius of curvature over time returns the same result as averaging over its configuration space, in our case target type. This implies that the set of images taken at different times can be regarded as a time evolution of a single system. While in earlier studies this assumption was implicitly applied, by our knowledge, we provide its first empirical confirmation of the assumption on the basis of analysis of experimental data.

Thus, the analysis of available existing data in supernova experiments provides the experimental confirmation of the following assertions: curvature of the shocks and the interface envelopes may be an imprint of the experimen-

tal conditions, the set of images taken at different times can be regarded as a time evolution of a single system, one can treat each of the spikes individually and thus enlarge the data set size and statistics.

3.2.3 Amplitude of the interface

In images from supernova experiments, a visible structure of bubbles and spikes is developed for all non-planar targets due to RT growth of the initial perturbations at the interface [37, 82]. During the run-time of the experiments, the perturbation grows approximately 70 times the initial perturbation peak-to-valley amplitude or approximately 5 times the initial perturbation wavelength [56, 57]. The amplitude of the interface is determined by measuring the distance between the base and tip of the spikes. We are able to measure spikes from images with high feature visibility. 83 spikes were measured from 12 images: 4 images from single mode targets, 3 from small-two-mode targets, and 5 from large-two-mode targets. We focus our analysis on the large-two-mode and single mode target types, since they provided the biggest data sets of images with clear features. For more detail on interface amplitude measurements, see Section 2.1.2.

For the large-two-mode case, the average interface amplitude at each time step is shown in Figure 3.2(a). The standard deviation of each time step is measured, and then those four standard deviations are averaged for an overall standard deviation. In terms of $\lambda = 71\mu m$, the initial perturbation wavelength, the average standard deviation is 0.21 wavelengths and, as the final amplitude is 4.21 wavelengths, this corresponds to a 5% variation for the large-two-mode targets.

For subsequent comparison with various models, we fit a power law to the spike growth, describing the growth of the interface amplitude as a power-law function of time, $h = Bt^b$. The large-two-mode targets produce spikes growing as $h \sim t^{1.14}$. Thus, according to data, the power law exponent is greater than 1 (unity) implying that the spike does accelerate in this particular time interval.

For the single mode case, the spike amplitudes are shown in Figure 3.2(b). The average standard deviation is 0.42 wavelengths and, as the final amplitude is 4.29 wavelengths. This corresponds to a 10% variation for the single mode targets, which is twice as large as the deviation of two-mode-large measurements. The additional noise is likely due to the smaller quantity and poorer quality of the data set. The best fit power law describes the single

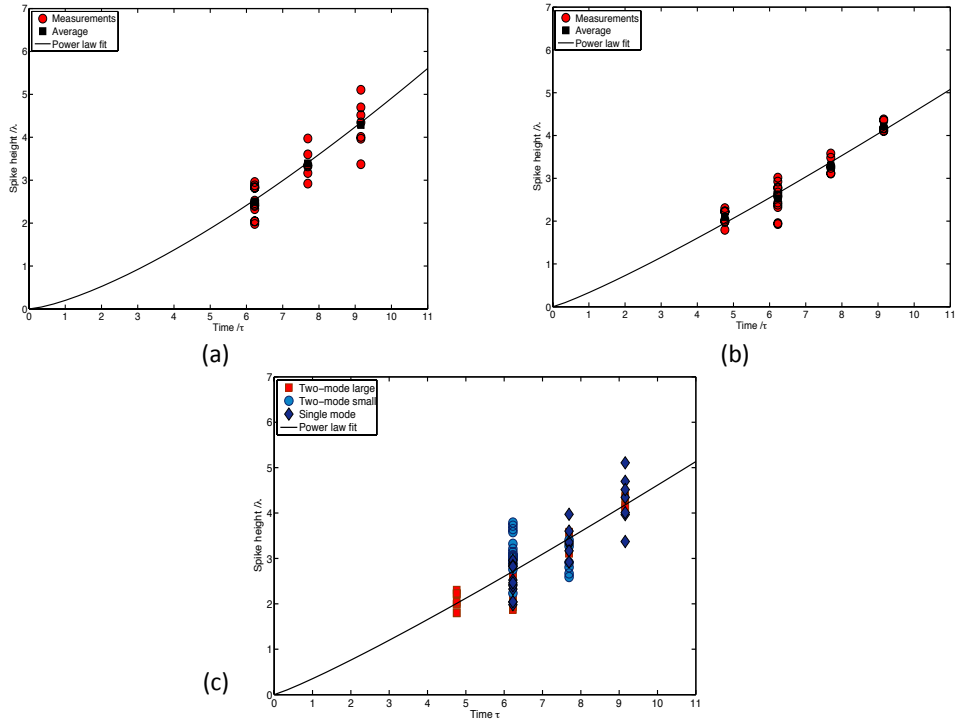


Figure 3.2: Spike amplitude for (a) single mode targets with $h \sim t^{1.39}$, (b) large-two-mode targets with $h \sim t^{1.14}$, and (c) all target types with $h \sim t^{1.12}$. Measurements of large-two-mode targets are shown as squares, two-mode small targets as circles, and single mode targets as diamonds.[94]

mode spike amplitudes as $h \sim t^{1.39}$.

When spikes of all target types are included and fit with a single power law, the spikes grow with an effective exponent of 1.12 (i.e. $h \sim t^{1.12}$), and an average standard deviation of 0.36 wavelengths corresponding to 8.5% variation, as the final amplitude is 4.25 wavelengths. The contributions of the various target types can be seen in Figure 3.2(c).

We work with averages at each time step because that is standard way for the community. The observation times were chosen to ensure reproducibility and consistency of extremely challenging experimental conditions. Although taking an average produces very coarse data, it matches the coarseness in the independent variable. We fit the data by two methods: linearizing and bootstrapping.

We combine data from all target types and find averages at each time step. Then, we plot the data on a log-log plot and fit the log of the data with a line (Figure 3.3). This linearization allows us to analyze the fit, including estimating errors. The linear fit is found by the expressions

$$b = \text{slope} = \frac{(n \sum x_i y_i) - (\sum x_i)(\sum y_i)}{(n \sum x_i^2) - (\sum x_i)^2} \quad (3.1)$$

$$B = \text{intercept} = \frac{(\sum x_i^2)(\sum y_i) - (\sum x_i)(\sum x_i y_i)}{(n \sum x_i^2) - (\sum x_i)^2} \quad (3.2)$$

where $x_i = \log(t_i)$, $y_i = \log(h_i)$, and n is the total number of data points, which is 4 in this case. With this method the error in the fit exponent is given by

$$\Delta b = \text{slope error} = S \sqrt{\frac{n}{(n \sum x_i^2) - (\sum x_i)^2}} \quad (3.3)$$

where $S = \sqrt{\frac{\sum (y_i - bx_i - B)^2}{n-2}}$, the sum of the residuals. By this method, the log of the data from all target types is described by a slope of $b = 1.1$ with error, $\Delta b = 0.1$.

If the data are assumed to be independent and identically distributed points, then we may use the bootstrapping technique. Bootstrapping uses random sampling with replacement to predict errors. To do this we fit a random sampling of the data and store the fit parameters in a list or array, we repeat 1000 times, and then we analyze the distribution of the fit parameters. When performed on all 82 spike measurements, the mean fit exponent is 1.24 and the standard deviation of the fit exponents is 0.08.

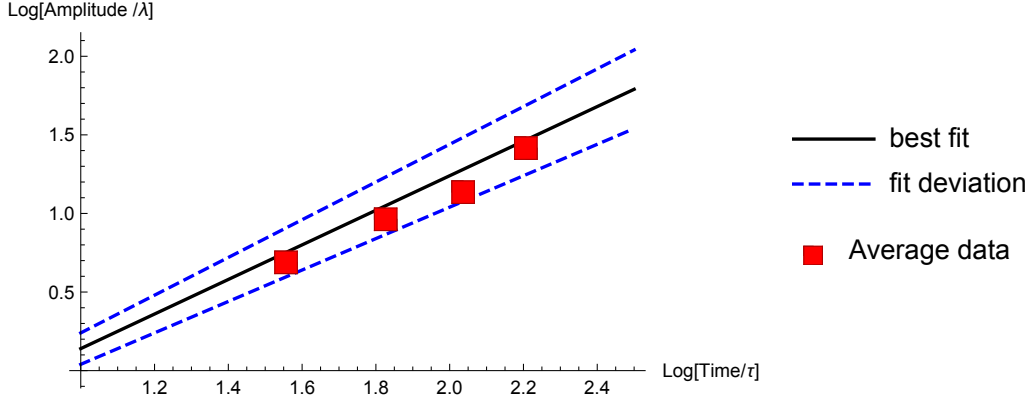


Figure 3.3: Average data (red squares) plotted with the fit from the linearized method. The dashed lines show the fit function with \pm the error of the fit exponent.

All data sets and fit methods suggest an exponent greater than 1. While it may appear that the two-mode targets and single-mode targets may have different interface growth, the difference is challenging to confidently determine due to the amount of variation in the measurements and the limited time range of available data. The linearized method and bootstrapping provide slightly different exponents, but both methods agree that the error in the exponents is small, 6 to 8% and the exponent is above 1.

3.3 Comparison with the momentum model

By comparing experimental data with the theoretical results, one can derive qualitative and quantitative conclusions on properties of RT mixing with time dependent acceleration, $g(t) = At^a$ in supernova experiments. One such property is the characteristic length scale L for energy dissipation. As the overall growth of the amplitude and the overall run time of the experiments are related as $(H/a_0) \sim (T/\tau)^{1.9}$ and $(H/\lambda) \sim (T/\tau)^{0.72}$, this may imply that in RT flow in experiments the amplitude is indeed a dominant length scale for energy dissipation. According to the theory (Table 2.3), for $L \sim h$, the acceleration exponent is $a = b - 2$ in the case of $b > (1 + C)^{-1}$; and it is $a \in (-2, -2 + (1 + C)^{-1})$ in case of $b = (1 + C)^{-1}$. On the other hand, for

$(h/\lambda) = B(t/\tau)^b$	Data	Steady state	Flash	Hyades	Drag
b	1.1	1	0.9	0.6	0.95
B	0.36	0.44	0.53	0.96	0.48

Table 3.2: Mean values of the parameters of theoretical solutions and numerical models for spike amplitude growth.

$L \sim \lambda$, the acceleration exponent is $a = 2(b - 1)$ with $a > -2$ and $b > 0$. Per experimental data, in RT flow $b > 1$ for all target types implying that $L \sim h$ and that the flow is in the mixing regime. Indeed, if one assumes that RT flow is in a nonlinear regime with $L \sim \lambda$, then the acceleration exponent would be $a = 2(b - 1)$ with $a > 0$ for $b > 1$, and the acceleration, $g(t) \sim t^a$ would be an increasing function of time. This behavior would contradict the design of supernova experiments, in which the system is influenced first by an initial shock and then by the rarefaction wave resulting in the decrease of the flow velocity [37, 81, 82]. Thus, per experimental data, in this particular time interval, $L \sim h$ and RT flow is in the mixing regime [15, 4, 8].

The other important property of RT flow is the exponents of the power law functions of the acceleration $g(t) = At^a$ and the amplitude $h = Bt^b$. On the other hand, per experimental data $b > 1$ for all target types implying that the acceleration exponent is $a = b - 2$ with $a > -1$, Table 2.3. This suggests that RT flow is in the regime of acceleration dominated mixing. On the other hand, numerical simulations indicate that the acceleration exponent is $a < -1$ [56, 57]. This case requires a more careful consideration, Table 2.3. Since in RT flow the effective drag is usually large with $C \gg 1$ [11], the critical values of $b = (1 + C)^{-1}$ and $a = -2 + (1 + C)^{-1}$ separating the acceleration dominated mixing regime from the dissipation driven mixing regime are $b \rightarrow 0$ and $a \rightarrow -2$, Table 2.3. In Hyades and FLASH simulations the value of b is finite, $0 \ll b < 1$, and the value of $a \sim -1$ [56, 57]. Thus, the numerical simulations indicate that RT flow is also in the acceleration dominated mixing regime.

For comparison of data with theory, we apply the acceleration exponent as suggested by the experiments and the simulations, Figure 3.4. Good agreement is achieved with experimental data in the case of exponents provided by the experiments ($g \sim t^{-0.9}$, $h \sim t^{1.1}$), Hyades simulations ($g \sim t^{-1.6}$, $h \sim t^{0.6}$), and FLASH simulations ($g \sim t^{-1.1}$, $h \sim t^{0.9}$). As on average in experiments and simulations the amplitude exponent is $b \sim 1$, we also compare

experimental data with the steady state solution of $b = 1$ that is permitted by the balance equations, Equation 2.5 for $L \sim h$, $a = -1$, Table 2.3, Figure 3.4. For the purpose of consistency, we present as well the comparison of experimental data with traditional drag model employing $L \sim t$ (with $h \sim t^{0.95}$, Table 2.3), and using multiple (7+) adjustable parameters [55, 34, 33, 13]. The values of the exponents and the prefactors are summarized in Table 3.2 in dimensionless units.

It is worth noting that while in both experiments and simulations of RT mixing flow the amplitude increases with $h \sim t^b$ and velocity decreases with $v \sim t^{b-1}$, experimental data imply that $b > 1$ leading to $h, v, \dot{v} > 0$, whereas simulations suggest $b < 1$ leading to $h, v > 0$ and $\dot{v} < 0$. Several reasons may explain this observation. First, within the available dynamic range of data, both kinds of dynamics fit the data well and are a challenge to differentiate, Table 3.2, Figures 3.2 and 3.4. Generally, a substantial dynamic range is required to reliably identify an exponent of a power law [89]. The current experiments and simulations span a decade or so. Without data spanning larger dynamic range and more sophisticated diagnostics, the power law exponent is a challenge to determine accurately [88]. In particular, as suggested by Figure 3.4 for the amplitude growth, the various power law functions begin to have some difference in value at 20τ ($\sim 50ns$), whereas data are only available up to roughly 10τ ($\sim 25ns$). Second, in realistic laboratory environment in supernova experiments, the influence of the shock and rarefaction wave on the target may be stronger than it is intended and may potentially cause the amplitude to grow quicker than linear with time. Third, as is true for any numerical method, the numerical simulations have numerical dissipation and diffusion that may potentially slow down the dynamics of RT mixing [56, 57, 37, 82, 81].

Finally for canonical blast waves in a uniform compressible fluid, the length scale increases as a power law with time, as $\sim t^b$ with $b < 1$ [87, 19, 92, 97, 86, 41]. This is because in ideal blast waves a large amount of energy is released in a small volume initially, and then this energy drives the dynamics in an expanding volume. At late times, no energy is supplied to the flow by other sources and no energy is lost due to dissipation. When a blast wave interacts with a density discontinuity leading to development of RTI, the flow dynamics may deviate away from this canonical scenario due to the transports of mass, momentum, and energy induced by interfacial RT mixing [66, 87]. Blast wave propagation in non-uniform fluids and its interaction with density discontinuities are open problems [87]. We relegate

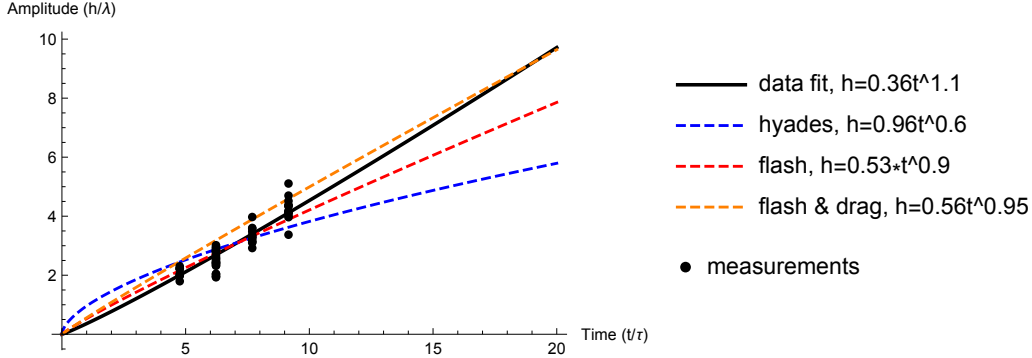


Figure 3.4: Measured spike amplitude points plotted with smooth power law fits $h \sim t^b$. [94]

consideration of these fundamental problems to the future.

Therefore, supernova experiments agree qualitatively and quantitatively with the theoretical analysis considering symmetries and momentum transport in RT flow [15, 4, 2, 8]. The available existing experimental data indicate that in supernova experiments with time dependent acceleration, RT flow is in the mixing regime, the amplitude is the characteristic length scale for energy dissipation (or, at least, contributes to it substantially), and the mixing flow is acceleration driven and keeps order. RT mixing dynamics in supernova experiments can be better understood upon further developments of theoretical, numerical, and experimental tools to handle matter at extremes [6, 79].

3.4 Discussion

In this chapter, we perform scrupulous data analysis study of supernova experiments that are designed to mimic and model astrophysical phenomena in a well-controlled laboratory environment at high power laser facilities [36, 79, 84, 17]. The parameters of experiments are properly scaled to model the interaction of a blast wave with helium-hydrogen interface in core-collapse supernova SN1987A [56, 57, 37, 82, 81]. In the experiments, strong laser beams irradiate an initially solid target composed of dense plastic and light foam causing the materials to behave as fluids, Figure 2.1. In the experimental system, the acceleration is time-dependent and is directed from the

denser to the light fluid leading to development of RTI and RT mixing. The experimental diagnostics includes x-ray radiography, Figure 2.2. We carefully analyze all structures in all available experimental images of RT flow in order to learn what experiments may tell us about the fundamentals of RT mixing in high energy density plasmas, Figures 2.3a, 2.3b, 2.4a and 2.4b. New theoretical asymptotic solutions are found to describe RT dynamics with time dependent acceleration in the nonlinear and mixing regimes, Table 2.3. The parameters of time dependent acceleration are evaluated on the basis of experimental data, as well as one dimensional Hyades and two-dimensional FLASH simulations, Figures 3.2 and 3.4. The data and the theoretical analysis are in good qualitative and quantitative agreements with one another, Figure 3.4.

To accurately compare the experimental data with one another and with the theory and simulations a novel scaling is found for data calibration, Table 3.1. We show that while in supernova experiments all quantities are time dependent, a scaling can be identified for RT evolution that is robust, reliable, and gives reasonable values. Our scaling employs the properties of the laser shot and the target, specifically - laser irradiance, target mass, and wavelength of the interface perturbation. It connects the parameters of RT mixing flow to well controlled parameters of the experimental system, and can be further applied for a design of future experiments on RT mixing in HEDP, Table 3.1.

In all experimental images, the interface envelopes and the shock fronts are curved. We measure these curvatures and thoroughly analyze the measurements showing that the curvatures are constant within the noise level and thus can be an imprint of experimental conditions, Figures 3.1a and 3.1b. On the basis of experimental data, further empirical evidences are provided that the set of images taken at different times can indeed be regarded as a time evolution of a single system, and that the dynamics of each of the different spikes can be analyzed. These results allow us to substantially increase the data set size and statistics of the interface measurements. They can be further applied for a design of future experiments on RTI in HEDP.

It is worth noting that it is a challenge to grasp precisely the cause of the curvature of the interface envelopes and shock fronts in HEDP experiments. The understanding of the phenomenon requires a synergy of theory, experiments, and simulations. The latter should be an integrated numerical approach including both Lagrangian and Eulerian modeling in order to reliably quantify the interplay of complex processes of light-material interaction

at microscopic scales (by means of molecular dynamics [32, 105], interaction of plasma flow with solid material boundaries at mesoscopic scales (by employing, e.g. smooth particle hydrodynamics simulations [91]), as well as interaction of shocks and rarefaction waves with density discontinuities and the influence of the finite size of the target (by using continuous dynamic simulations [56]). We address such integrated study to the future. Our empirical results on the constancy of the curvature of shock fronts and interface envelopes and on the weak influence of the curvature on the spike amplitude may serve as benchmarks for the existing and future experiments and simulations.

We perform scrupulous measurements of the interface features and analyze RT mixing for all available experimental times and all target types, Figure 3.2. Considering the extended data set with the enlarged statistics, we show that the corresponding variations of the spike amplitude are low (less than and within 10%) and that it is a challenge to confidently quantify the effect of superimposed modulations on RT evolution in different target types. The analysis of experimental data indicates that, within the time interval of experiments, the dynamics of RT spikes can be described as a power law and that RT spikes do accelerate. These results can be accounted for in a design of future experiments on RTI in HEDP.

By applying rigorous theoretical analysis that considers symmetries and momentum transport in RT flow and by further extending it to the case of acceleration with power law time dependence, we report new asymptotic solution describing RT dynamics, Table 2.3. We show that similar to the case of constant acceleration, in the case of time dependent acceleration the nonlinear and mixing regimes exist in RTI. In the nonlinear regime, the characteristic scale for energy dissipation is the horizontal wavelength and in the mixing regime it is the vertical amplitude, Table 2.3. Similar to the case of constant acceleration, in the case of time dependent acceleration the growth of horizontal scales is possible and is not a necessary condition for RT mixing to occur. RT mixing develops due to imbalance of the gain and loss of specific momentum, with the vertical scale being the characteristic scale for energy dissipation [15, 4, 8]. Detailed consideration of these asymptotic solutions will be given elsewhere.

By comparing supernova experiments with the theory, we find that the available existing data agree qualitatively and quantitatively with the theoretical analysis considering symmetries and momentum transport in RT flow, Figures 2.2 and 3.4. In particular, the data indicate that, in supernova

experiments RT flow is in the mixing regime, the amplitude significantly contributes to the characteristic length scale for energy dissipation, and the mixing flow is acceleration driven and keeps order.

Within the time intervals of supernova experiments, RT spikes appear to grow somewhat quicker in the experiments than in the simulation, Figure 3.2. Potential reasons for this observation may include relatively short dynamic range of the observation time, possibility of a stronger influence of the shocks and rarefaction waves on the flow in the experiments, and a potential effect of numerical dissipation and diffusion in simulations.

In Figure 3.4 we extend the time range nearly two fold of the actual time of supernova experiments (T/τ) in order to emphasize the necessity of a substantial dynamic range of the observation time for accurate evaluation of the exponent of the amplitude on the basis of data, Table 3.2. In order to increase the value (T/τ) and to achieve more advanced stages of RT mixing, one can increase the time T of the experiment and/or decrease the characteristic time scale τ . The time scale τ depends on the target mass and the laser irradiance (Table 3.1). For decreasing τ one may increase the laser irradiance by increasing the laser energy and decreasing the laser pulse duration and the target area and may also decrease the target mass. In addition, one may refine time steps at which the measurements are taken. By implementing these changes in future experimental design one may extend the observation time (T/τ) and identify more accurately the power law exponent b of the amplitude growth $h \sim t^b$ in supernova experiments, Figure 3.4, Table 3.2.

Our results clearly indicate that the dynamics of RTI under conditions of high energy density, the interaction of blast waves with density heterogeneities and discontinuities and the explosion of core-collapse supernova are fundamental problems that are well open for a curious mind [6, 7, 15, 4, 56, 57, 79, 84, 17, 87]. Further developments of theoretical, numerical, and experimental tools are required to better understand RT mixing in supernova experiments and to handle matter at the extremes.

To conclude, supernova experiments agree qualitatively and quantitatively with the theoretical analysis considering symmetries and momentum transport in RT flow in HEDP and show that RT mixing keeps order.

Chapter 4

Data analysis of multiplicative noise in Rayleigh-Taylor mixing

4.1 Introduction

As discussed earlier, Rayleigh-Taylor Instability presents a challenging problem because it is non-linear, non-local, anisotropic, multi-scale, and statistically unsteady [2, 4]. We investigate the statistical unsteadiness of RT mixing by numerically modeling the set of stochastic nonlinear differential equations which govern the rate of change of momentum in a packet of fluid undergoing RT instability. We analyze characteristic values across two regimes, measure the spectra of fluctuations, and investigate how fluctuations inherent in RT mixing may affect measurables.

Observations of RTI have reported significant scatter in the coefficient describing the vertical scale of the interface [85, 34, 29, 76, 27]. This observed scatter can be due to fluctuations inherent to the physical process or challenging experimental conditions such as sensitivity to initial conditions. Some of the scatter may be caused by noisy character of RT turbulent mixing, which is not typically quantified in the existing experiments and simulations (Section 1.1). Fluctuations in RT flows provide a stimulating subject for study distinct from classical Kolmogorov turbulence. In Kolmogorov turbulence, the energy dissipation is a statistical invariant and the random character of dissipation is caused by velocity fluctuations. In contrast, RT turbulent mixing has velocity and length-scale fluctuations and the energy dissipation rate grows with time [8], providing an additional challenge to the problem.

As a result of the flow evolution, RTI has characteristic structures at two scales. The large-scale bubble and spike structures may retain order and depend on the initial conditions. The dynamics of small scale structures are driven by shear, which is in general a noisy process. Small scale dynamics of RT flow may be more disordered and less deterministic. We investigate the influence of this disorder on large scale measurable parameters. The nonlinear regime may couple small and large scales. The noisiness due to shear on small scales may influence the overall dynamics, including some characteristics of the large-scale motion such as the non-universal α parameter. Fluctuations of the interfacial dynamics at small scales lead to fluctuations in density, temperature, and velocity, which then may cause fluctuations in the energy dissipation or the effective drag force. Drag is the source of energy dissipation in RT dynamics and it effects large scale flow quantities such as the growth of the interface.

The rate of growth of an interface undergoing RT instability is governed by the balance between the rates of gain and loss of momentum as described by the momentum model in Section 2.2.4. The rate of gain of momentum is given by gravity or an effective gravity (acceleration) while the rate of loss of momentum is due to energy dissipation. Hence, inherent fluctuations in small-scale flow characteristics may influence large-scale flow characteristics. It is important to analyze the impact these fluctuations may have on measurable quantities. We implement these ideas in the method of the momentum model with stochasticity, in Section 2.2.5.

RT mixing in supernova explosions and inertial confinement fusion is driven by a blast wave [102, 17]. The hydrodynamics of blast waves in incompressible fluids is described by self-similar solutions [87, 19]. The scaling law is set can depend on the load history and mass transport or the problem dimensionality, depending on how the energy is deposited [97, 86, 92, 41]. Considering these two important applications of RT mixing and wanting the solutions to remain generally applicable, we use accelerations in the form of power laws.

To study stochastic effects in RT mixing, the drag coefficient is modeled as a stochastic quantity, extending the momentum model as described in Section 2.2.5. The differential equations that describe RT mixing in the momentum model must be written in differential form and must include another equation to describe the evolution of the drag coefficient. The drag coefficient is described with a lognormal distribution plus a standard Wiener process. A lognormal distribution is chosen because a RT mixing fluctuations

are known to have long-tail distributions [5, 6].

Using a numerical differential equation solver with multiplicative noise in C++, we numerically solve the governing equations with the acceleration modeled as a power law and the drag coefficient modeled as a statistical process with a lognormal distribution, as described in Section 2.2.5 [5, 6]. In order to accurately determine the power law solutions we model 10^3 trajectories over six decades of time for each set of parameters. The modeled values of the acceleration and drag coefficient are output as diagnostics and the solution for the amplitude of the interface and its growth rate are output for analysis.

4.1.1 Relationship to previous studies

In previous work the numerical differential equation solver was used to model RTI with a stochastic drag term for a large dynamic range. The cases of constant acceleration [5] and power law accelerations with exponents ranging between -1 and 0 [6] have been well studied. It was found that the parameter α , the growth rate commonly used by the RTI community to characterize RT flow, is sensitive to fluctuations of the drag coefficient and that invariants of the flow exist despite the statistically unsteady nature of the problem.

The drag term, which determines the rate of loss of momentum in RT mixing, depends on a characteristic length scale. RT mixing involves many different size scales, but there are two easy-to-observe lengths: a vertical scale in the direction of growth, $h(t)$ and a horizontal scale normal to growth, λ . The horizontal scale corresponds to the wavelength of the initial sine wave perturbation. The system is in the nonlinear regime if the dominant length scale is the horizontal, λ . The vertical scale corresponds to the amplitude of the interface, which grows due to the instability. The system is in the mixing regime if the dominant length scale is the vertical, $h(t)$. These scales and the solutions they produce are discussed in Section 2.2.4.

Depending on the value of the acceleration exponent within the mixing regime, there are two different asymptotic solutions. The critical value of the acceleration exponent that divides the two regimes is beyond the previously studied regime. When the acceleration exponent is larger than the critical value, the dynamics are in the acceleration dominated mixing regime. A sub-range of the acceleration dominated mixing regime has been studied with a stochastic model before [5, 6]. Below the critical acceleration exponent, the dynamics are significantly influenced by the drag term and are

in the dissipation dominated mixing regime. We analyze the dynamics for both mixing regimes and demonstrate how certain values behave during the transition across the critical acceleration exponent. The dissipation dominated mixing regime may be relevant to supernova explosions and inertial confinement fusion because blast wave and shock wave drive RTI have accelerations matching the range of this regime. This work studies the dissipation dominated mixing regime for the first time, providing valuable insights for comparing models with experimental data.

We use the momentum model with a stochastic drag term to study how fluctuations influence RT mixing. In this work we thoroughly analyze two mixing regimes and the transition between them. Analysis of the nonlinear regime is left to future studies. The theoretical analysis of asymptotic solutions for the momentum model indicates that there is a critical value of the acceleration exponent. By looking at values near and on either side of the critical value, we determine that exponents are less sensitive to noise than coefficients in all cases and each range has its own invariants and dominant asymptotic solutions. We study the power spectrum density to better understand how multiplicative noise influences the solution. Additionally, we look at how these new invariants are affected by different values of the drag coefficient and averaging over different numbers of trajectories.

4.2 Results

4.2.1 Exponent and coefficient sensitivity

Comparing models to experimental data is a serious challenge for RTI. Due to the stochasticity, nonlinearity, and non-local behavior it is difficult to obtain precise experimental measurements over large enough dynamic ranges. For example, one must measure a value over multiple decades to accurately fit a power law, which is the functionality suggested by asymptotic solutions to the momentum model for RT mixing. However it is challenging to perform experiments that provide more than one measurable decade.

In recent studies, many have found fits to experimental data in order to determine the coefficient of the growth of the interface, sometimes called α . The vertical length of RTI flow is described as $h \sim \alpha f(A)gt^2$ where α is a constant, Section 2.2.1. This measurement has yielded a large spread in values, producing confusion and competition between experiments and

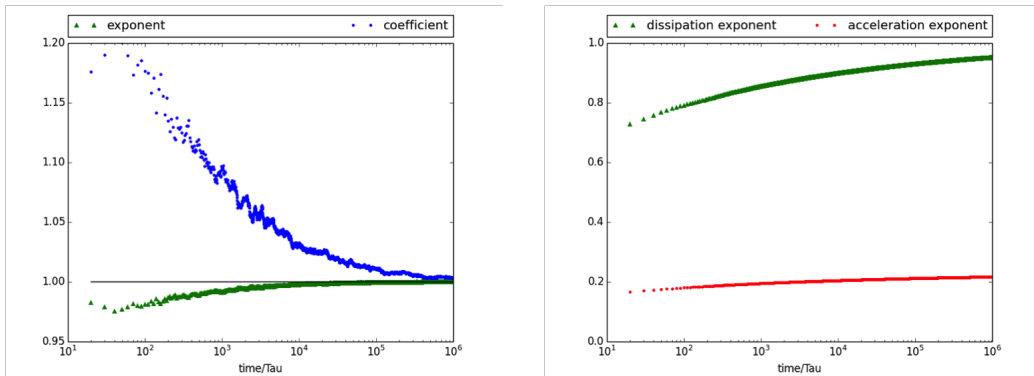
simulations. The amplitude of the interface can be described by a power law. We show that the coefficient is more sensitive to noise than the exponent. Thus the exponent is a better diagnostic measurement than the coefficient.

As discussed earlier, we treat the drag coefficient C as a stochastic quantity and then numerically solve Equation 2.6. The interface motion is dependent on C and can possibly inherit the fluctuations. For power law accelerations, $g = At^a$, the analytic asymptotic solutions describe the interface as a power law, $h = Bt^b$. The power law solution's coefficient is more sensitive to fluctuations than the exponent. In the asymptotic solutions in the acceleration dominated mixing regime, the coefficient is explicitly dependent on C , a fluctuating quantity, while the exponent only depends on the constant acceleration exponent, a [Table 2.3]. In the dissipation dominated mixing regime, the coefficient is not defined by known flow quantities because it is a free parameter. Therefore in both regimes, the exponent provides a more reasonable diagnostic than the coefficient. This can be seen in Figure 4.1.

We model thousands of trajectories of the stochastic differential equations [Equation 2.6], measuring h and v over six decades. To determine the modeled exponent, we use the power law solution and its derivatives to find $b = vt/h$. To determine the modeled coefficient, we multiply the solution (Bt^b) by t to the $-b$ power, using the modeled value of b to find $B = ht^{vt/h}$. The modeled coefficient and exponent are plotted in Figure 4.1a, each normalized by their analytic values (Table 2.3). The modeled coefficient has a larger difference from its analytic value, larger fluctuations, and takes more time to converge to its analytic value. The exponent, while not perfect, fluctuates significantly less and quickly converges to the analytic value. In Figure 4.1b, the modeled exponent in the dissipation dominated mixing regime is normalized by the analytic values of both regimes. The coefficient is not plotted because in this regime it is a free parameter. When normalized by the proper analytic value, the modeled exponent in the dissipation dominated regime approaches ~ 1 . This implies that when comparing experiments to models, one should focus on the exponent, as it is less susceptible to both experimental and intrinsic fluctuations.

4.2.2 Critical value of the acceleration exponent

Previous work modeling the same system of equations focused on values of the acceleration exponent between -1 and 0 [6]. For exponents between -1 and 0 , \dot{v} is always positive and the dynamics are dominated by the acceleration.



(a) The modeled solution's coefficient and exponent, each normalized by their analytic value in the acceleration dominated mixing regime ($a = -0.75$).

(b) The modeled exponent normalized by the analytic values in the dissipation dominated regime and the acceleration dominated regime ($a = -1.95$).

Figure 4.1: The modeled solutions normalized by analytic values.

We have identified a critical value of the acceleration exponent beyond the previously studied range, $a_{critical} = -2 + 1/(1+C)$. In the regime above the critical value, the acceleration term plays a dominant role in the dynamics and the regime is called the acceleration dominated mixing regime. The solution's second derivative has nearly the same slope as the acceleration, g , as seen in Figure 4.2a. Since \dot{v} and g have approximately the same slope, the dissipation effect is therefore small and does not have a strong influence on the dynamics when a is above $a_{critical}$.

The asymptotic solution to the momentum model [Equation 2.5] changes below $a_{critical}$ indicating a new regime. Below the critical value the dissipation term has a significant influence on the dynamics and the acceleration becomes negligible, especially at large times. One can see the influence of the dissipation term in Figure 4.2b. The slope of \dot{v} in the figure is no longer the same as g because the solution is modified by the dissipation term. The regime corresponding to values of the acceleration exponent below the critical value is called dissipation dominated mixing. These two regimes also have different invariants, as discussed in detail in Section 4.2.4.

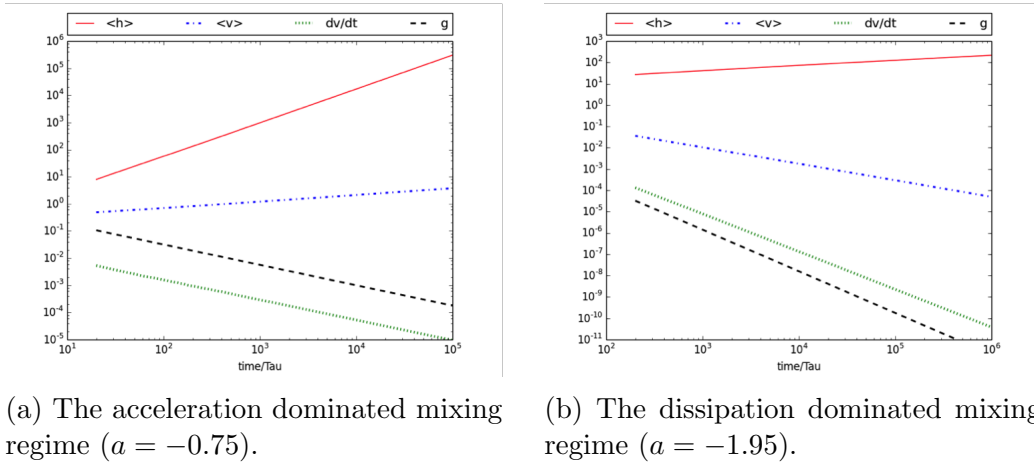


Figure 4.2: The external acceleration g (black), the solution h (red) and the solutions first and second derivative (blue and green) plotted on a log-log plot to demonstrate the power law dependence for both sub-regimes of the mixing regime.

4.2.3 Asymptotic solutions

We model Equation 2.6 with $C = 3.6$ and $a \in \{-1, -1.5, -1.65, -1.75, -1.85, -1.95\}$ to add to the range of the previously studied regime, verify the value of $a_{critical} = -2 + (1+C)^{-1} \sim 1.78$, and study the transition between regimes. The dynamics of each value of a were modeled over six decades (t ranging from 10^0 through 10^6) and the time evolution of certain quantities are plotted with their asymptotic analytic solutions.

To determine if the modeled solution matched the analytic solution, the modeled values of the coefficient and exponent were normalized by their analytic values and plotted in Figure 4.1a and 4.1b. We use the expression vt/h to determine the modeled values of the exponent and the expression $ht^{-vt/h}$ to determine the modeled values of the coefficient. In the acceleration dominated mixing regime, the modeled exponent is divided by its analytic value, $b = a + 2$, and the modeled coefficient is divided by its analytic value, $B = A/[(a+2)((a+1)+C(a+2))]$. In these plots, 1 represents an exact match between the numerically modeled value and the analytic value. Figure 4.1a shows an example of a data set in the acceleration dominated mixing regime. Both values inherit fluctuations from C but still clearly approach the analytic values.

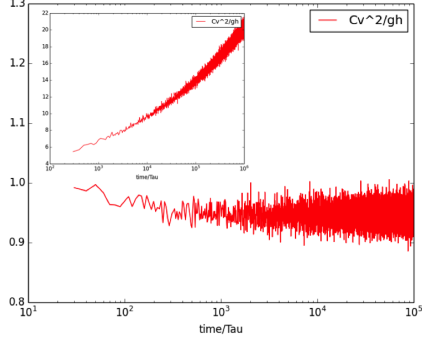
Figure 4.1b shows the normalized exponent values for a data set in the dissipation dominated mixing regime. In this case, according to the analytic solution, the coefficient is a free parameter and is omitted from the plots. The exponent was plotted with its appropriate analytic solution, $b = (1 + C)^{-1}$ (the “dissipation exponent”) in green as well as the solution for the acceleration dominated mixing regime (the “acceleration exponent”) in red. Unsurprisingly, the dissipation exponent is more accurate than the acceleration exponent. The modeled solutions agree with the analytic solutions, especially at late times. This indicates that our code works as expected.

4.2.4 Invariant quantities

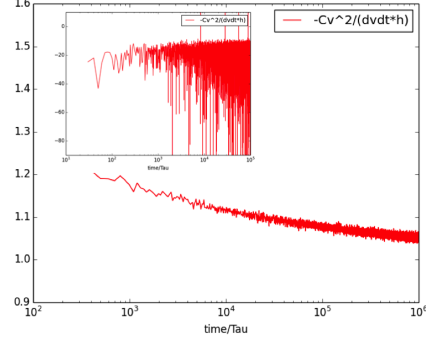
It is important to look for invariant quantities in physical systems in order to better learn about the symmetries and underlying processes involved in the problem (Section 1.1). Previous studies have shown that there is an invariant quantity of RT mixing, despite the statistical unsteadiness and time dependent dynamics [6, 5]. This invariant, Π , is the ratio of the rates of gain and loss of momentum, $\Pi = \mu/\bar{\mu} = \epsilon/\bar{\epsilon}$. All previous work has shown that $\Pi \approx 1$. In the acceleration dominated mixing regime, the current work supports the same result as seen in Figure 4.3a. This can also be seen in the analytic solutions for $\Pi = \mu/\bar{\mu} = \frac{Cv^2}{gh}$. Using power laws for g and h , and taking the time derivative of h to find v , this becomes $\Pi = \frac{CBb}{A}t^{-a-2+b}$. At first glance, this seems to be time dependent, however in this regime $b = a + 2$, meaning Π is proportional to t^0 . Both analytically and according to the numerical results, Π is constant approximately equal to 1 in the acceleration dominated mixing regime.

However, the exponent in the dissipation dominated mixing regime does not have the same dependence on a . The expression $\Pi = \frac{Cv^2}{gh}$ is proportional to $t^{-a-2+1/(1+C)}$ in the dissipation dominated mixing regime. This is only time independent when $a = a_{critical}$. This time dependence is illustrated for $C = 3.6$ in the insert in Figure 4.3b. While Π is constant with an average value of 1 for $a > -1$ (acceleration dominated regime), it is a smaller value and decreases for $a = -1.95$, a value below $a_{critical}$ (dissipation dominated regime). This regime requires a different characteristic value.

As discussed in Section 2.2.4, the asymptotic solution for the amplitude of the interface in the accelerated mixing regime is a power law with exponent $b = a + 2$ and coefficient $B = A/[(a+2)((a+1)+C(a+2))]$. In this regime, when



(a) The characteristic values modeled in the acceleration dominated mixing regime.



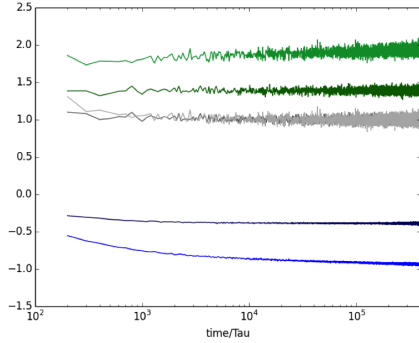
(b) The characteristic values modeled in the dissipation dominated mixing regime.

Figure 4.3: The appropriate (main figures) and inappropriate (inserts) characteristic values in the acceleration (a) and dissipation (b) dominated regimes.

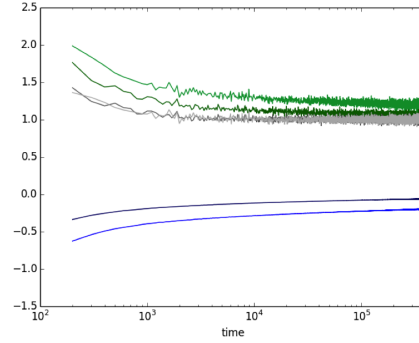
the acceleration $g(t) = At^a$ has the exponent $a > -2 + (1 + C)^{-1}$, one can rearrange the governing equations [Equation 2.5] to find a constant expression

$$\frac{dh}{dt} = v, \quad \frac{\dot{v}}{g} + \frac{Cv^2}{gh} = 1 \quad (4.1)$$

where $g \neq 0$. The two terms on the left hand side of the second equation must always add to a constant. Above the value $a = -1$, both terms are positive and less than 1. Below the value $a = -1$, the first term ($\frac{\dot{v}}{g}$) is negative and the second term ($\frac{Cv^2}{gh}$) is greater than 1, still their sum is always 1. Because this expression should always equal 1, we use it to check that our model is sound and the code works as expected. As demonstrated in Figure 4.3a, this expression's mean value is indeed 1 even though it inherits fluctuations from the stochastic C value. As the acceleration exponent decreases, the dynamics approach the other regime and the two terms diverge more (but always sum to 1). This behavior is demonstrated by plotting the time evolution of the two terms and their sum. The two terms significantly diverge for the smaller values of a , but they grow symmetrically in either direction, maintaining a constant sum. In Figure 4.4a, we plot these three terms for three successive values of a , approaching $a_{critical}$ from above.



(a) Approaching $a_{critical}$ from above. The terms of the invariant and their sum is plotted for various values of a within the acceleration dominated mixing regime.



(b) Approaching $a_{critical}$ from below. The terms of the invariant and their sum is plotted for various values of a within the dissipation dominated mixing regime.

Figure 4.4: The invariant value plotted as a approaches $a_{critical}$ in each regime. As the colors get lighter, a gets closer to $a_{critical}$.

As the acceleration exponent decreases, the value of the acceleration, g approaches zero more quickly. This is problematic for the invariant because g is in the denominator of both terms. This is the cause of the diverging terms in Figure 4.4a. In the dissipation dominated mixing regime we cannot use the same characteristic expression that was used in the acceleration dominated mixing regime. Instead of dividing the equation by g and rearranging to isolate 1, we perform a similar procedure with \dot{v} . Dividing Equation 2.5 by \dot{v} and rearranging terms yields,

$$\frac{dh}{dt} = v, \quad \frac{g}{\dot{v}} - \frac{Cv^2}{\dot{v}h} = 1 \quad (4.2)$$

As a decreases, asymptotically g also decreases and the first term becomes negligible. Thus in the appropriate regime, the term $\frac{-Cv^2}{\dot{v}h}$ is a constant approximately equal to 1. We can verify its lack of time dependence by plugging in h , v , and \dot{v} , and we find that the expression is proportional to $t^{2b-2-b+2-b} = t^0$. The characteristic value for dynamics with acceleration exponents below $a_{critical}$ is shown in Figure 4.3b.

The two regimes can be demonstrated by plotting the averages of the characteristic values, $\frac{-Cv^2}{\dot{v}h}$ and $\frac{Cv^2}{gh}$ for various acceleration exponents as in

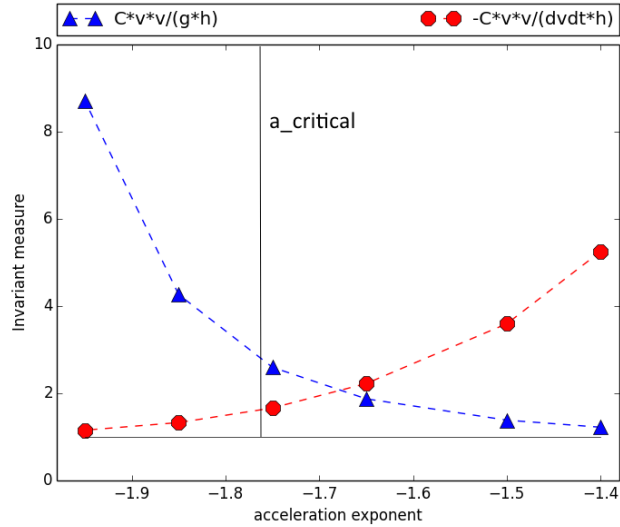


Figure 4.5: Two characteristic values measured across the entire range of tested acceleration exponents. In their respective regimes above and below $a_{critical}$ they are nearly flat, but diverge as they cross the critical value.

Figure 4.5. The characteristic value in the acceleration regime value is nearly flat in the acceleration regime and asymptotes below the critical value of the acceleration exponent. The characteristic value in the dissipation regime value is nearly flat in the dissipation regime and asymptotes above $a_{critical}$. Thus, the dynamics of the two regimes are distinct in quantity as well as quality; one must treat each regime separately when analyzing characteristic or invariant values. These characteristic values can provide a diagnostic; by calculating their numerical value for an experiment or simulation, one could determine the regime of the dynamics.

4.2.5 The effect of $\langle C \rangle$

In the above sections, we have thoroughly explored how the dynamics can be described for different values of the acceleration exponent, a . Next we study how the drag coefficient changes the behavior of these two regimes. Several different values of the drag coefficient are investigated for particular a values in both regimes. For small values of the acceleration exponent, the dynamics are securely in the acceleration dominated mixing regime and changing the

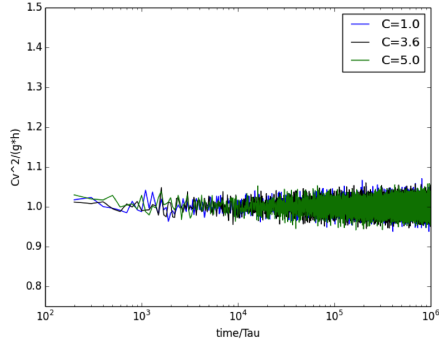
value of $\langle C \rangle$ has a subtle effect on the dynamics. Larger fluctuations show up in the modeled quantities when $\langle C \rangle$ is smaller. When $\langle C \rangle$ is larger, the dynamics are slightly smoother, despite having the same σ to $\langle C \rangle$ ratio because the large drag coefficient acts as a fluctuation moderator. Figure 4.6 shows the invariant quantities for both regimes, comparing various values of the drag coefficient. The value of $\langle C \rangle$ was limited by computational abilities and we studied $\langle C \rangle = \{1.0, 3.6, 5.0\}$. In all of the cases the normalized values have a constant average value close to 1 as expected. In the acceleration dominated mixing regime, the characteristic value is not sensitive to $\langle C \rangle$, as seen in Figure 4.6a. However, the characteristic value in the dissipation dominated mixing regime is sensitive to the value of $\langle C \rangle$ as seen in Figure 4.6b.

The value of $a_{critical}$ depends on the value of $\langle C \rangle$. If we compare the results of different $\langle C \rangle$ for a value of the acceleration exponent near $a_{critical}$, for example, $a = -1.95$ in the dissipation dominated mixing regime, then there are larger changes in the behavior because changing the value of $\langle C \rangle$ may change the regime of the dynamics or cause the dynamics to approach the critical value. While changing $\langle C \rangle$ may change the value of $a_{critical}$ and therefore the regime of a particular a value, the dissipation dominated mixing regime's small range makes it more susceptible to changes in the value of $a_{critical}$. If studying the acceleration dominated mixing regime, we can stay far away from the regime boundary and not be affected by changing $\langle C \rangle$. This is why the dissipation regime's invariant is more influenced by $\langle C \rangle$ than the acceleration regime's invariant.

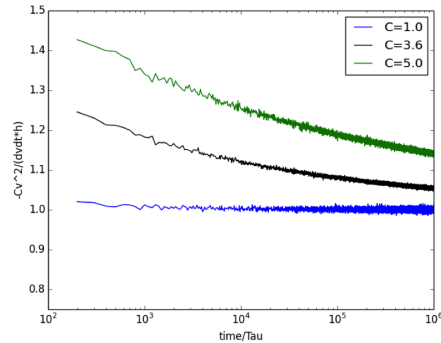
4.2.6 Number of trajectories

The code that numerically solves the stochastic differential equation typically averages over many trajectories. We now investigate how the number of trajectories influences the solution by averaging the numerical data over 1, 10, and 100 as well as the default value of 10^3 trajectories. The steady state solution in the acceleration dominated mixing regime is used in order to isolate the statistical effects and minimize complexity. When $a = -1.0$ in the mixing regime, the solution's derivative, v is a constant and \dot{v} is zero. By using the steady state solution [Section 2.2.4], we minimize the time dependent dynamics and can investigate the stochastic behavior more closely.

Fewer trajectories lead to more noise in measured values and the same general trends persist throughout all the measured quantities. The drag



(a) The invariant in the acceleration dominated regime for $\langle C \rangle = \{1, 3.6, 5\}$. As $\langle C \rangle$ increases, $\frac{-Cv^2}{gh}$ remains ~ 1 .



(b) The invariant in the dissipation dominated regime for $\langle C \rangle = \{1, 3.6, 5\}$. As $\langle C \rangle$ increases, $\frac{-Cv^2}{v h}$ diverges from 1.

Figure 4.6: The invariant values plotted for various values of $\langle C \rangle$.

coefficient, the solution, and the characteristic value all have less spread when more trajectories are averaged as illustrated for the drag coefficient in Figure 4.7. The equations are simulated over long time spans ($10^6 t/\tau$) in order to see the behavior at different stages in the evolution. During the first couple decades, the dynamics are still influenced by initial conditions and it is difficult to measure statistics. We may evaluate the mean past the third decade, and more sophisticated statistical measures (moments) may be made beyond this.

The characteristic value in the acceleration regime, $\frac{Cv^2}{gh}$, maintains its mean value of 1, indicating that we are in the expected sub-regime and the code is functioning properly. As with the drag coefficient and the solution, the standard deviation of the characteristic value increases when the number of trajectories is decreased.

For most accelerations, RT dynamics are statistically unsteady. That is, there are statistical fluctuations around time dependent variables. We want to observe the fluctuations around the mean separately from the mean dynamics. Again, the steady state case is used in order to isolate properties of these fluctuations. The power spectral densities (PSD) of the drag coefficient, the solution, and its derivative are measured for the case when a single trajectory is used and no averaging occurs. The PSD is found by squaring the discrete Fourier transform of a signal. For example, the PSD of C is

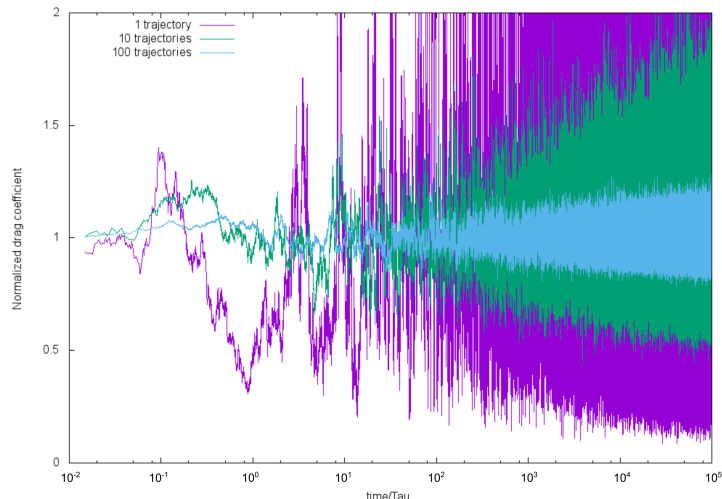


Figure 4.7: The time evolution of $C(t)$ plotted for various numbers of trajectories. As the value is averaged over more trajectories, the fluctuations become narrower.

computed as

$$\text{PSD}(\omega) = \frac{(\Delta t)^2}{T} \left| \sum_{n=1}^N C_n e^{-i\omega n} \right|^2 \quad (4.3)$$

where Δt is the time step size, $T = N\Delta t$ is the total time and C_n is the n^{th} value of C .

The drag coefficient, C has a power spectrum with two regions, each with characteristic power laws. On a log-log plot, C 's spectrum has a slope of -0.258 between frequencies 10^{-4} and 10^{-2} and a slope of -1.66 between frequencies 10^1 and 2×10^2 as seen in Figure 4.8. The PSD of C is smooth, even when evaluating one trajectory.

The PSDs of h and v have more noise and a different slope than C . Because of the noisiness, averages of 20 points around each endpoint were used to find an accurate slope. The PSD of h is described by one line between frequencies 2×10^{-4} and 10^1 with a slope of -1.64 (Figure 4.9a). The PSD of v is close to constant, but has significant noise due to using only one trajectory. The PSD of v is described by a line between frequencies 10^{-4} and 10^2 with a slope of -0.320 (Figure 4.9). Compared with the spectra of

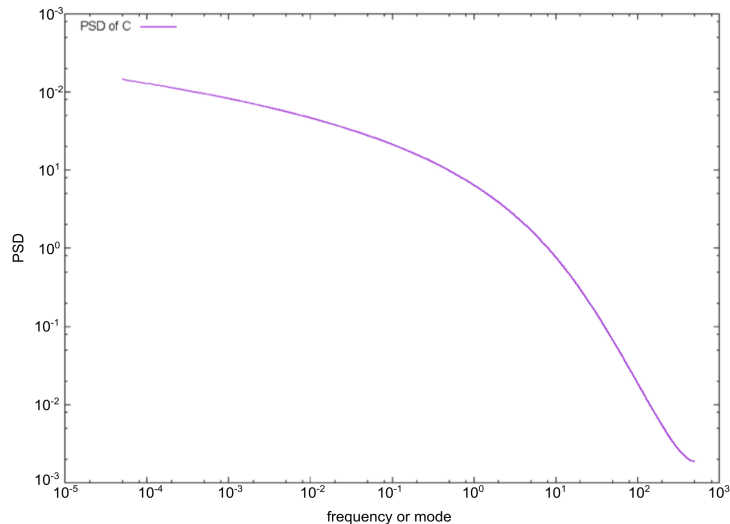


Figure 4.8: PSD of C.

Kolmogorov turbulence, this model is has a significantly different fluctuations in v . In Kolmogorov turbulence, energy (or v^2) scales with $k^{-5/3}$, Section 2.2. The stochastic momentum model used in this study has PSD scaling approximately as $k^{-1/3}$ which is much less steep than canonical Kolmogorov turbulence.

4.3 Discussion

We present results from a comprehensive study of a stochastic version of the momentum model for Rayleigh-Taylor instability with time dependent acceleration and vertical characteristic length. An established numerical method is expanded to model previously unstudied regimes [91]. This new regime is of great importance to the study of RTI in supernova explosions and inertial confinement fusion. The accelerations corresponding to the new regime are similar to those describing blast wave accelerations. By exploring our model below the critical acceleration exponent, we describe a regime that may correspond to blast wave driven RTI and Richtmyer-Meshkov instability. We contribute diagnostic values that may be used to compare the state of the art experiments with theoretical models, furthering our understanding and

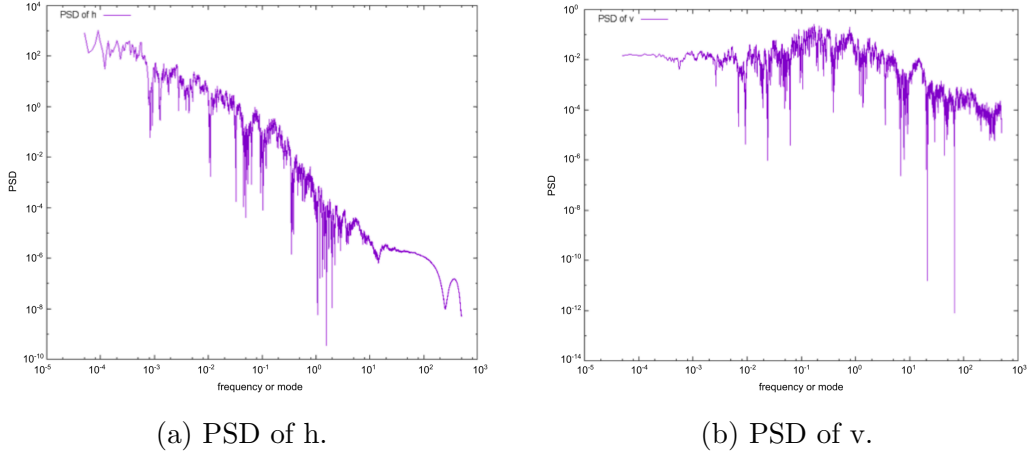


Figure 4.9: Power-spectrum-density.

potential control of RTI in processes such as inertial confinement fusion.

Both sub-regimes of the mixing regime are fully described and explored; a critical value of the acceleration exponent divides the acceleration dominated regime from the dissipation dominated regime. Solutions and invariants for each regime are discussed and the critical turning points are investigated. The numerical model converges to the asymptotic analytic solutions. As previous studies have shown, the exponent is less influenced by fluctuations than the coefficient (Figure 4.1). Averaging over different numbers of trajectories allows for additional statistical analysis (Section 4.2.6). We find new characteristic values that may be used as a diagnostic measurement of the regime (Figure 4.5). The power spectrum density of the drag coefficient (4.8), solution(4.9a), and derivative of the solution (4.9) are calculated and analyzed for the steady state case using only one trajectory. We find that our code behaves as expected and can describe the amplitude of the interface of two fluids undergoing Rayleigh-Taylor mixing. By studying the numerically modeled stochasticity, we contribute to the statistical knowledge of Rayleigh-Taylor Instability.

Despite having different behavior, the dynamics of each regime can be described by the same governing equations. In this work, both sub-regimes have been thoroughly studied and explored. RT mixing dynamics are modeled for various power law accelerations and the numerical model converges to the analytic solution for all tested values of the acceleration exponent. To avoid

overly demanding computational resources, an averaging system is utilized in which the stochastic differential equation is solved for many trajectories, and then the trajectories are averaged. This averaging process behaves as expected, with more trajectories decreasing the size of noisy deviations for all measured quantities. This is demonstrated with the drag coefficient in Figure 4.7. The averaging did not affect the qualitative properties of the solutions and it made macro-quantities easier to reliably diagnose.

The sub-regime is determined by the acceleration exponent, with a critical value of the exponent dividing the regimes. The two sub-regimes can also be diagnosed with a characteristic value. The combination $\frac{Cv^2}{gh}$ is approximately 1 in the acceleration dominated mixing regime (Figure 4.3a) while $\frac{-Cv^2}{\dot{v}h}$ is approximately 1 in the dissipation dominated mixing regime (Figure 4.3b). If these same characteristic values can be measured for experimental or simulation data, then the particular regime of the experiment may be determined. Whichever value of the two is close to one determines the subregime of the system (Figure 4.5). This characteristic value provides a valuable metric for comparing experiments, simulations, and theory.

Special attention was given to the steady state solution, when the acceleration exponent is -1.0 . In the steady state case, the time dependent dynamics are minimized because the solution's time derivative is zero. It is easier to measure fluctuations around the mean values in the steady state case because the mean values themselves are linear or constant rather than time dependent power laws. Since the dynamics did not overwhelm the signal, we were able to perform rigorous statistical analysis on the fluctuations. We measured the power spectrum density for the drag coefficient and the solution and compared the results with each other and Kolmogorov turbulence. Both the drag coefficient and the solution have non-trivial spectra and may be fit in segments with two different power laws. Data plotted in Figure 4.8 suggest that the drag coefficient's spectra can be described by -0.258 between frequencies 10^{-4} and 10^{-2} and -1.66 between frequencies 10^1 and 2×10^2 . In frequencies above 10^2 , the data breaks the trend, likely due to small sample size at large frequencies. The solution's power spectrum density is more linear than the drag coefficient and it expresses a more noisy signal (Figure 4.9a). The power spectrum density of the velocity is significantly different than canonical Kolmogorov turbulence (Figure 4.9), adding to the evidence that RT mixing is a turbulent process distinct from Kolmogorov turbulence [4, 2].

The coefficient of the function describing the interface amplitude has often been used as a diagnostic measure for RTI observations. By introducing a stochastic process in the governing equations, we find that the coefficient is sensitive to fluctuations inherent in disordered RT mixing and experimental conditions. On the other hand, the exponent provides a diagnostic that is robust to noisiness and helps determine the regime of the problem (Figure 4.1a). Since multiple decades are needed to accurately fit a power law, it may be challenging for experimentalists to measure exponents. However, future experiments and simulations should give more attention to measuring and fitting the exponent of the interface growth in order to evaluate the theoretical models of RT mixing and further understand the fundamental science behind these systems.

In the future, this type of study may be extended in several different ways. With small changes to the code, future studies may look at the different distributions of fluctuations on the drag coefficient, different types of noise (additive vs multiplicative), or different accelerations. Currently our group is working on spatially varying accelerations to extend the method beyond time dependent accelerations such as in this work. There are ongoing opportunities to model multiplicative noise in differential equations.

Our results demonstrate how the stochastic model and similar numerical models can be used to reliably study the effect of multiplicative noise on observational quantities. In the case of RT mixing, we may better understand the role that microscopic fluctuations have on the macroscopic dynamics. With knowledge about the statistical behavior of RTI, we may better understand how to interpret the experimental data by determining which measures are more or less susceptible to inheriting fluctuations, and anticipating noisiness in aggregate data. Studying the measurable effects of fluctuations also helps us understand the character of the fluctuations and what physical significance they might have.

Chapter 5

Data analysis of simulated Richtmyer-Meshkov interfacial growth

5.1 Introduction

The dynamics of Rayleigh-Taylor instability (RTI) and Richtmyer-Meshkov instability (RMI) in high energy density plasmas (HEDP) are complex processes involving multiple simultaneous physical phenomena [15, 6, 42, 61]. Plasma considerations characterize the dynamics by a strong influence of radiation transport, charge-field interactions, complex material properties, and other effects on top of challenging hydrodynamic properties such as strong shocks, highly contrasted fluid densities, and large perturbations [42, 15, 6]. In the past 10 to 15 years, the RTI/RMI community has made successful headways in the understanding of HEDP hydrodynamics, including experiments at high powered laser facilities [36, 82], large scale simulations with both Eulerian and Lagrangian methods [90, 91, 28, 49, 34], and rigorous theoretical analyses [15, 4, 2, 74, 103]. It is known that RMI evolution depends on the amplitude of the initial perturbation, and the small scale dynamics at late times are non-uniform, with structures such as hot spots and cumulative jets [91].

One still poorly understood aspect of RMI evolution is the partitioning of energy between the interface and the bulk of the fluid flow. Understanding this fundamental physical process will further our understanding of RMI and

its applications in experiments and technology. After a shock wave interacts with a fluid interface separating fluids of different acoustic impedance, two types of motion occur in the fluid flow. The bulk of both fluids moves in the same direction as the shock with background velocity, v_∞ , and an initially perturbed interface will expand with an interface growth rate v_0 . This evolution is illustrated in Figure 5.1. By looking at the background velocity and the interface growth rate we may compare the amount of energy deposited to the interface with the energy of the bulk flow [90, 45, 66]. When the initial interface has a single mode sinusoidal perturbation, the amount of energy deposited to the interface can be quantified by the growth rate, v_0 , which depends on the shock strength, fluid properties, initial perturbation amplitude, and wavelength [91, 74, 46]. The amount of energy deposited to the fluid bulk is quantified by the background velocity v_∞ and it depends on the shock strength and fluid properties [91, 80]. Generally, only a fraction of the shock energy is transferred to the interface. The ratio of velocities v_0/v_∞ is relatively small across a broad parameter regime, ranging from $v_0/v_\infty = 0$ to $v_0/v_\infty \sim 0.5$ [91].

We study the effect of the initial perturbation amplitude on the RMI interfacial dynamics using SPH simulations described in Section 2.2.2. In order to study the evolution of RMI in a well controlled environment, especially avoiding radiation transport, charge-field interactions, and non-canonical material properties, we use a hydrodynamic approximation. The results are compared with existing theories, simulations, and experiments and achieve good agreement. The background motion is shown to agree with linear theory [103]. We measure the initial interface growth rate and compare with linear and weakly nonlinear theory. The dependence of the initial growth rate on the initial perturbation amplitude is studied by fitting simulation results to an empirical model.

SPH code was used to model Richtmyer-Meshkov instability (RMI) in a broad range of parameters. We investigate an intermediate to high range of Mach numbers 3, 5, and 10 and high fluid density contrasts, Atwood number 0.6, 0.8, and 0.95. The initial perturbation amplitude was varied from 0% to 100% of the initial perturbation wavelength, λ . The preliminary results of the simulations have been presented, finding a non-monotonic dependence of the initial growth rate on the initial perturbation amplitude, a_0 [31].

In this synergistic study, the values of (v_0, a_0) are described with an empirical model, compared to rigorous theoretical results, and the relationship of the results with other simulations and experiments is discussed. We find

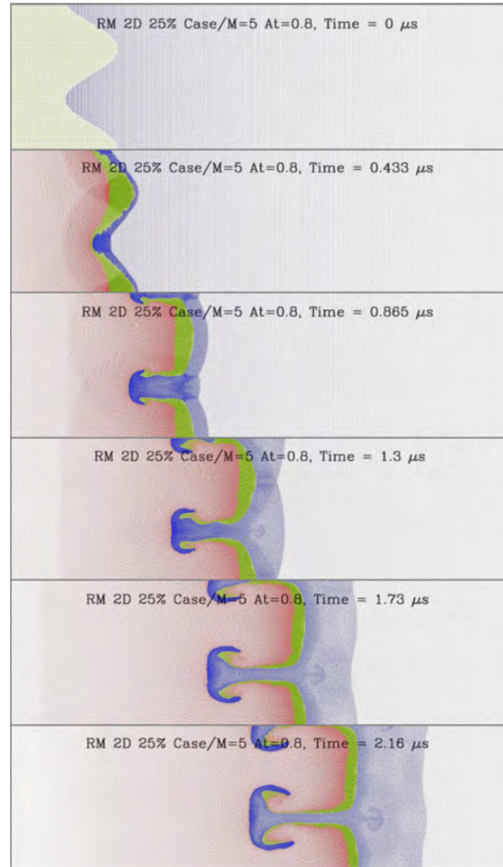


Figure 5.1: Simulation results showing the compound motion induced by the shock. The shock passes through the interface between fluids of different acoustic impedance (from left to right). After the shock passage, the fluid moves as a whole with speed $v_\infty < v_{shock}$ to the right and the interface grows due to the instability with growth rate $v_0 < v_\infty$ [31]. The colors represent region, a property that corresponds to the initial positions. The light fluid is shown in red and green and the heavy fluid is shown in blue.

that the background motion agrees with linear theory within 1% [31, 103], the initial growth of the interface has a nonmonotonic dependence on the perturbation amplitude, and may be described by an empirical model. By studying the relationship between initial perturbation amplitude and the initial growth of the interface, we may study the energy partitioning between the bulk motion and the interface growth. We present an upper bound to the energy deposited to the interface.

5.2 Simulation setup

The data analyzed in this chapter were obtained from [31] with a computational setup similar to [91]. Continuing to study along similar computational parameters allow us to expand, confirm, and strengthen the previous results. In this study, SPH code simulates a regime with strong shocks ($M \in \{3, 5, 10\}$), high density contrast ($A \in \{0.6, 0.8, 0.95\}$) and a large range of initial amplitudes ($0 < (a_0/\lambda) < 1$). Approximately 2×10^5 particles are simulated for each set of parameters. In order to keep the computation accurate near the interface while maintaining computational efficiency, the spacing of particles varies across the domain, depending on the flow fields.

The dynamics of ideal mono-atomic gases are modeled with adiabatic index $\gamma = 5/3$, initial temperature $T_0 = 300K$, and initial pressure $P_0 = 2.494 \times 10^6 Pa$. The gas constants are $R_l = 8.314 J/mol \cdot K$ and $R_h = \{2.079, 9.238 \times 10^{-1}, 2.132 \times 10^{-1} J/mol \cdot K\}$ depending on Atwood number. The densities are $\rho_l = 1 \times 10^{-3} kg/m^3$ and $\rho_h = \{4 \times 10^{-3}, 9 \times 10^{-3}, 3.2 \times 10^{-2} kg/m^3\}$ depending on the Atwood number. These gases are rarefied and rather stiff. The energy per proton initially ranges from 1.92 eV to 1.03 MeV and reaches 1.1 keV to 2.8 MeV after the shock passes through the interface.

Compared to realistic gases, the simulated gases are scaled by a few orders of magnitude. For example, helium has density $\rho_{He} = 1.64 \times 10^{-1} kg/m^3$ under initial temperature $3 \times 10^2 K$ and pressure $10^5 Pa$. Under the same conditions, nitrogen's density is $\rho_{N_2} = 8.08 \times 10^{-1} kg/m^3$. Because of these differences as well as the existence of numerical viscosity and surface tension in the SPH code, a sequence of simulations are conducted to ensure key measurables are not affected. In the control simulations the initial temperature, pressure, and densities correspond to the realistic gas values. Good agreement is found between SPH simulations and experiments [90, 69]. This indicates that the dynamics of the flow are scale-invariant and the numerical

viscosity and surface tension have a negligible effect on the results. We may use the rarefied and stiff gases to effectively model realistic gases.

In our case, the SPH code simulates RMI in a two-dimensional domain with size $1 \times 10^{-2} m$ by $3 \times 10^{-2} m$. The shock propagates from the light fluid to the heavy fluid with its Mach number defined relative to the speed of sound in the light fluid ($c_l = 2.039 \times 10^3 m/s$). The fluid interface is normal to the shock propagation and initially positioned in the middle of the domain with approximately equal areas of light and heavy fluid.

As discussed, using characteristic scaling values when analyzing simulated and experimental data is important [Section 1.1]. We scale amplitudes, velocities, and time by the following values. The wavelength of the initial perturbation, λ is the characteristic length scale and v_∞ is the characteristic velocity [91, 45, 31]. Both of these choices are common. These two values can combine to provide a characteristic time, $\tau = \lambda/v_\infty$. The scaling values are presented in Table 5.1

The time duration of each simulation is 3τ , which provides enough time to study the initial growth rate of RMI. This value ranges depending on the Mach number: from $\tau = 9.5 \times 10^{-7} s$ for $M = 10$, $A = 0.6$ to $\tau = 8.3 \times 10^{-6} s$ for $M = 3$, $A = 0.95$. In all cases, the reflected shock has time to reach the end of the computational domain and in some cases the flow has time to proceed into the highly nonlinear regime before the simulation ends [31].

5.3 Diagnostics

The complete structure and evolution of the RM flow is contained in the SPH simulation data. Scalar and vector flow fields are completely known, including region, density, temperature, pressure, and velocity across the entire domain. Both qualitative and quantitative analysis may be performed on SPH simulation data. Qualitative analysis can be performed on images of these flow fields. Many important features have been identified by qualitative analysis of the flow fields, such as cumulative jets, hot spots, and the shape of the bubble tip [91, 90]. For quantitative analyses, data from regular time intervals is stored for post processing. Additionally, moving probes (i.e. designated particles that act as markers) may be used to quantify interface dynamics [91]. Moving probes allow real-time data capture, but the probe signal may be noisy because of small scale structures such as vortices on the sides of spikes [91]. Here, we analyze measurements of the

Mach	Atwood	$v_\infty \times 10^3 \text{ m/s}$	$\tau \times 10^{-6} \text{ s}$
3	0.6	2.7586	1.1963
	0.8	2.1059	1.5670
	0.95	1.2016	2.7464
5	0.6	5.0035	0.6596
	0.8	3.8488	0.8574
	0.95	2.2229	1.4845
10	0.6	10.384	0.3178
	0.8	8.0141	0.4118
	0.95	4.6475	0.7101

Table 5.1: Scaling values v_∞ and τ . The fluids are monoatomic gases with adiabatic index $\gamma = 5/3$. The velocity values are rather large due to the use of artificial gasses in order to improve computational efficiency. When the computations are scaled to realistic values, excellent agreement is achieved with experiments. [31]

time evolution of the velocity and the shape of the large scale flow features (RM bubbles and spikes).

Through a “snapshot” technique [91], where qualitative features of the dynamics are observed at instances throughout the evolution, the flattening of the bubble front, a checkerboard velocity field in the fluid bulk, reverse cumulative jets, and local hot spots have been observed [91, 31]. In [31] a new way to determine the initial RMI growth of the interface was developed. This method uses the difference in the positions of spikes and bubble fronts to measure the amplitude of the interface as illustrated in Figure 5.2.

Typically the simulation evolves as follows: the initial sinusoidal perturbation is set by the amplitude a_0 and wavelength λ , the shock propagates from the light fluid to the heavy fluid, first compressing the interface decreasing the perturbation amplitude until the shock passes the entire interface, after which RMI develops and interfacial growth begins. If the simulation runs long enough, the shock will reflect off of the far domain wall and travel back towards the interface. After the reflected shock meets the interface again, the amplitude of the interface decreases [31]. We focus our analysis on the initial growth rate, truncating most analysis before the shock is reflected.

The initial growth rate is calculated by taking the time derivative of the

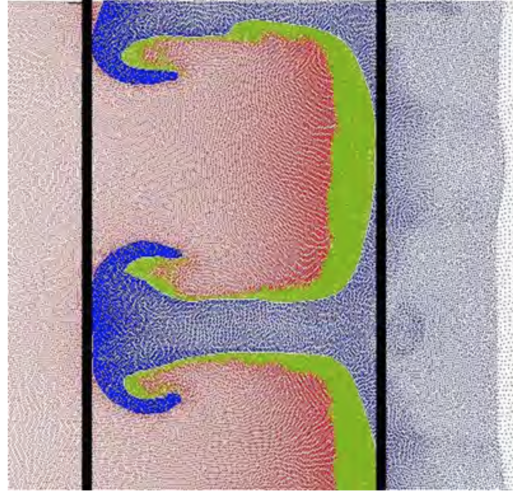


Figure 5.2: Illustration of the technique used to measure the amplitude of the interface. Black lines mark the spike and bubble positions and their difference provides the measure of the interface amplitude [31].

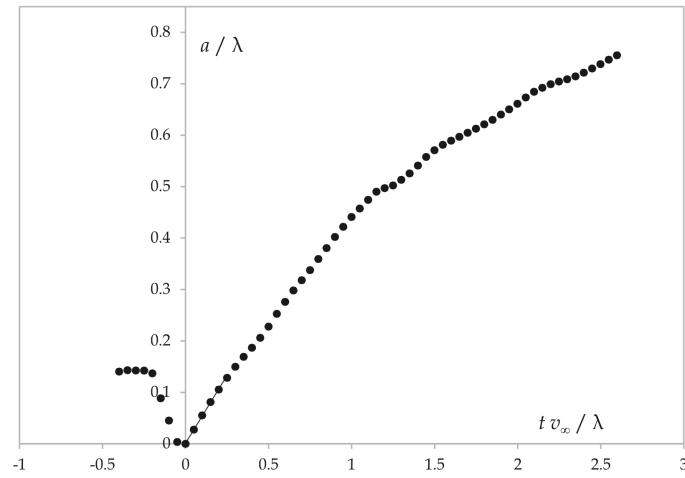


Figure 5.3: The time evolution of difference between the spike position and bubble position. The first 6 time steps after $t = 0$ are used to calculate the initial growth rate, v_0 [31].

interface amplitude over the first 6 time steps after the shock passes through the interface. The average of $v_0 = h(t)/t$ is calculated with $t = 0$ corresponding to the smallest value of the amplitude of the interface and $h(t)$ describing the time evolution of the amplitude of the interface. Figure 5.3 shows the time evolution of h . The slope is measured immediately after the time step with the smallest amplitude, before the behavior becomes nonlinear in time. The time interval over which this calculation occurs is small with each time step $(1/20)\tau = (1/20)(\lambda/v_\infty)$ for a total time interval of 0.3τ . It should be noted that the initial growth rate is found by taking the time derivative of the difference in the bubble and spike positions [91, 31]. This definition is used because the shape of the interface does not remain sinusoidal in RMI evolution in the case of strong shocks and high contrast fluid densities, notably causing asymmetry in size and shape of the bubble and spikes [91].

In order to use the background velocity v_∞ as a characteristic scaling value for velocity, it must first be measured. The value of v_∞ is different for different Mach and Atwood numbers and must be calculated for each combination of these parameters. To calculate the background motion, a planar initial interface is simulated and the time derivative of the interface amplitude is measured within the interval between the shock passing through the interface and the reflected shock hitting the interface. The background velocity provides a good characteristic scaling value because it is a relevant to the flow, it is easy to measure precisely (it agrees within 1% of zero-order theory, and 6% of previous simulations, Table 5.2), and it provides reasonable velocity values (on the order of $\sim 10^0$) [Section 1.1].

5.4 Results

5.4.1 Velocity of the background motion

The fluid bulk and interface move together with velocity v_∞ after the shock passes through the surface. In reference [31], the value of v_∞ is calculated in SPH simulations for planar interfaces with a broad parameter regime of Mach and Atwood numbers. This value is crucial for the analysis of the interface motion, v_0 because we use it as a scaling parameter. By comparing these two velocities, we may measure how the shock's initial energy is partitioned between the bulk flow and the interface instability.

The bulk velocity v_∞ is expected to depend on Mach number, Atwood

Mach	Atwood	Simulated v_∞/c_l	Theoretical v_∞/c_l	Percent Error
3	0.6	1.3529	1.3609	0.5878
	0.8	1.0328	1.0391	0.6063
	0.95	0.5893	0.5924	0.5233
5	0.6	2.4539	2.4710	0.6920
	0.8	1.8876	1.8998	0.6422
	0.95	1.0902	1.0961	0.5383
10	0.6	5.0927	5.1202	0.5371
	0.8	3.9512	3.9512	0.5264
	0.95	2.2793	2.2938	0.6321

Table 5.2: Simulated [31] and theoretical [103] values of the background velocity normalized by the speed of sound in the light fluid. The results agree within 1% for all simulated Mach and Atwood values.

number, and the adiabatic index of the fluids [80]. It can be calculated from zero-order theory, although v_∞ has a complicated dependence on M and A for strong, finite shocks and high, finite density contrast [80, 103]. Previous studies have shown that v_∞ is supersonic for strong shocks ($v_\infty/c_l > 1$ for $M > \sim 2.5$) and the bulk velocity is slower than the shock velocity ($v_\infty/c_l < M$) by approximately one order of magnitude [91]. Compared to the post shock velocity in a standard shock problem, u_p , the bulk velocity is smaller ($v_\infty/c_l < u_p/c_l = M(1 - 1/\rho_{21})$ where $\rho_{21} = (\gamma+1^2_M)/[(\gamma+1^2_M)+2]$ [91, 14]).

As shown in Table 5.2, the SPH simulated values of v_∞ agree quantitatively within 6% of previous SPH studies [91] and within 1% of zero-order theory [103, 80]. [31] found that for fixed Atwood number, increasing Mach number increases v_∞ and for fixed Mach number, increasing Atwood number decreases v_∞ . The values of v_∞ in the parameter range $3 \leq M \leq 10$, $0.6 \leq A \leq 0.95$, and $\gamma = 5/3$ scale with M and $A(1 - A)$. The v_∞ values can be empirically modeled as $(v_\infty - u_p)/c_l \approx M(\kappa_1(A(1 - A)) + \kappa_0)$ with fit parameters $\kappa_1 = 1.53$ and $\kappa_0 = -0.61$) [31].

5.4.2 Growth of the interface amplitude

RMI growth begins after the shock passes all the way through an initially perturbed interface. At early times, the amplitude of single-mode sinusoidally perturbed interface will grow linearly with time. At small but finite times,

the growth slows as it enters the nonlinear regime. We are primarily interested in measuring the growth rate in the linear stage, v_0 . The value of v_0 depends on Mach number, Atwood number, the speed of sound in the light fluid, the adiabatic index, and the initial perturbation amplitude, a_0 [103].

The measured values of v_0 are scaled by the characteristic velocity v_∞ [Table 5.1]. It is important to note that v_0/v_∞ is a relative measurement of the interface and bulk velocities, not an absolute measurement of the interface growth. This relative measurement gives us insight into the energy partitioning between the interface and bulk, providing more meaning than the absolute measure of v_0 alone.

Dependence on the initial perturbation amplitude

Linear theory can be used when the initial perturbation amplitude is small because the growth rate of the interface v_0 depends linearly on a_0 for small values of the initial perturbation amplitude (when $ka_0 \ll 1$) [98, 74, 46]. Linear theory provides the initial growth rate as a function of Mach number, Atwood number, adiabatic index, speed of sound, and the initial perturbation wavelength [103]:

$$[v_0]_{linear} = C_0 c_l(ka_0), \quad C_0 = C_0(M, A, \gamma) \quad (5.1)$$

SPH simulations of RMI agree with the linear growth rate for small values of the initial perturbation amplitude ($(ka_0) \sim O(10^{-2}), O(10^{-1})$), indicating the simulation results are accurate and valid [91, 31].

For $(ka_0) < 1$ (but not $(ka_0) \ll 1$), the interfacial dynamics are no longer linear and incompressible weakly nonlinear theory can be applied [98, 74, 46]. Weakly nonlinear theory suggests that for small but finite values of a_0 , the initial growth of the interface can be described by correcting the linear theory (Equation 5.1) by a factor F as $[v_0]_{W.N.L} = F[v_0]_{linear}$ [74, 103]. The correction factor, F can be calculated and is a power law function of the initial amplitude a_0 and the Atwood number A . As per weakly nonlinear theory, the initial growth rate is an increasing function of a_0 that grows slower than linear; $[v_0]_{W.N.L}$ is expected to be a monotonic function [98, 46].

The SPH simulation results agree with the weakly nonlinear theory within 10% for small values of the initial amplitude ($a_0/\lambda \leq 0.1$) and all values of Atwood number ($A = \{0.6, 0.8, 0.95\}$) [98, 46, 31]. However, for values of a_0 above ~ 0.3 , the simulated v_0 is smaller than $[v_0]_{W.N.L}$ [31, 91, 46]. The discrepancy between simulations and experiment may be due to complex

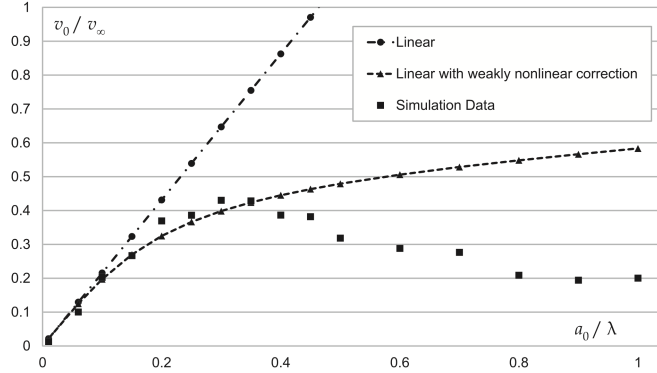


Figure 5.4: The initial RMI growth rate as a function of initial perturbation amplitude from simulation results (squares), linear theory (line), and weakly nonlinear theory (dashed line) [31].

physical processes such as secondary shocks and geometric factors which are not accounted for in weakly nonlinear theory. To our knowledge, no existing theory is capable of rigorously describing these effects.

To illustrate the extent of agreement with theory, an example of simulated (v_0, a_0) data [31] is shown with linear theory and weakly nonlinear theory [103] in Figure 5.4.

5.4.3 Empirical model of the interface growth

RTI growth has traditionally thought to increase as the initial perturbation amplitude increases, as per linear and weakly nonlinear theory. To the author’s knowledge,[31] was the first presentation of non-monotonic dependence of v_0 on the initial perturbation amplitude. As published in [31], the interface growth rate has a non-monotonic dependence on the initial perturbation amplitude, a_0 . As seen in Figure 5.5, v_0 increases as a_0 increases up to a_0 between 0.2 and 0.4% λ . After the peak v_0 value, the trend decreases at a decreasing rate (it is decreasing and “concave up”).

To quantitatively investigate the behavior of the interface growth, we fit an empirical model to the simulated data using the function:

$$v_0/v_\infty = C_1 \frac{a_0}{\lambda} e^{-C_2 \frac{a_0}{\lambda}} \quad (5.2)$$

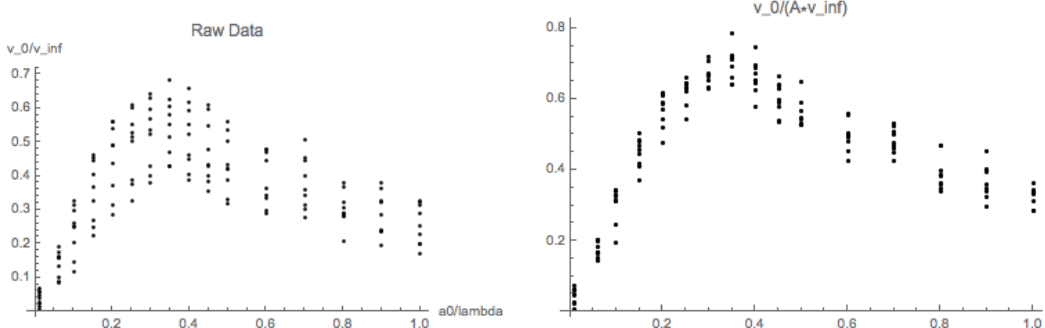
where C_1 and C_2 are adjustable parameters and A is the Atwood number.

Mach	Atwood	C_1 (fit)	C_2 (fit)
3	0.6	3.11	2.94
	0.8	4.17	3.06
	0.95	4.59	2.85
5	0.6	2.69	2.60
	0.8	3.95	2.92
	0.95	4.64	2.81
10	0.6	2.49	2.41
	0.8	3.77	2.69
	0.95	4.65	2.74

Table 5.3: Fitted coefficient values from the empirical model (Equation 5.2) for all simulated values of Mach and Atwood number.

This function was chosen because it recreates the linear theory in the limit of small initial perturbation amplitude and has the same concavity for large initial perturbation amplitude [Section 1.1]. Table 5.3 shows the fit parameters for all simulated Mach and Atwood numbers. Unlike the analysis for v_∞ we do not present comparison with linear theory because the theory is inaccurate for larger values of the initial perturbation amplitude. Linear theory is only expected to be accurate over $\sim 10\%$ of the range of a_0/λ values analyzed.

Figure 5.5a shows the simulated data from all Mach and Atwood numbers together as a scatter plot. The average value of C_1 is 3.78 with a standard deviation of 0.839 leading to a deviation of $\sim 22\%$. C_1 is expected to show significant dependence on Mach and Atwood number. The fit coefficient C_1 is related to the coefficient in linear theory and weakly nonlinear theory. In the theoretical models, the coefficient depends on Mach and Atwood number, thus we expect C_1 to depend on M and A . Since a wide range of Mach and Atwood values are simulated, we expect a large range in C_1 values. The scatter collapses if the initial growth rate is normalized by the Atwood number, as seen in Figure 5.5b. This is expected from linear theory, where the coefficient depends on A . We divide Equation 5.2 by A and then analyze the fit parameter C_1/A . The average value of C_1/A is 4.81 with a standard deviation of 0.332 corresponding to a deviation of $\sim 7\%$. Dividing by Atwood number significantly collapses the data quantitatively as well as qualitatively.



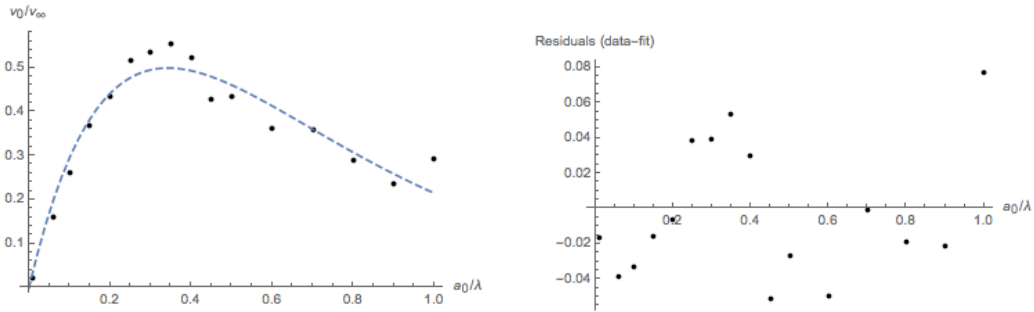
(a) Simulated values of the initial growth rate normalized by the bulk motion v_∞ . (b) Simulated values of the initial growth rate normalized by Av_∞ .

Figure 5.5: The initial growth rate of the interface (v_0/v_∞) versus the initial perturbation amplitude (a_0/λ). In (b) the data collapses when divided by Atwood number, A .

In other words, there is a constant parameter in the empirical model that varies less than 10% across all simulated Mach and Atwood numbers.

Remarkably, the fit parameter C_2 has little variation with respect to Mach and Atwood number. The average value of C_2 is 2.78 with a standard deviation of 0.196 leading to a deviation of $\sim 7\%$. The simulated density ratio changes from $\rho_h/\rho_l \sim 4$ to ~ 40 and the Mach number ranges from 3 to 10. The exponent of the fit varies within 7% over all simulated M and A values. The same C_2 value is applicable across a broad parameter range. This universal factor may be an important quantification of RM flow dynamics.

Figure 5.6 shows an example of a single run of SPH data plotted with its fit. While all individual data sets show similar trends, we choose a parameter combination in the middle of the tested range to illustrate the general behavior, using Mach number 5 and Atwood number 0.6. In Figure 5.6b we present the residual values for this particular case. The residuals are all less than 0.08 (dimensionless units $\sim v_0/Av_\infty$), while the data's mean is 0.36. The fit may provide insight into the behavior of the initial growth at larger initial perturbation amplitudes. Future studies may improve its agreement with data by adding more points to the fit or extending the range.



(a) Simulated values of the initial growth rate normalized by the bulk motion v_∞ and the fit line (Equation 5.2) for $M = 5$, $A = 0.6$.

(b) Residuals between the data and fit from Figure 5.6a.

Figure 5.6: One example of details of the fit. (a) shows the v_0/v_∞ data (dots) and the fit line (dashed line) while (b) plots the difference between the two (the residuals).

5.5 Energy partitioning

The nonmonotonic dependence of v_0 on a_0 indicates that there may be a maximum amount of energy deposited at the interface (the rest going into bulk fluid flow). Since the energy deposited at the interface is proportional to v_0^2 , the peak value of v_0 corresponds to the peak value of the interface energy. The peak value of v_0/v_∞ occurs between a_0/λ is 0.35 and 0.40. After this peak value it decreases with a decreasing rate [Figure 5.5].

We use E_0 to denote the energy deposited at the interface and E_∞ to denote the energy of the bulk motion in analogy with v_0 and v_∞ . Quantitatively, the energy ratio can be calculated as $E_0/E_\infty \sim v_0^2/v_\infty^2 \sim (v_0/v_\infty)^2$. The the maximum of v_0/v_∞ for each simulation is found and the average of these maximums is $\langle [v_0/v_\infty]_{max} \rangle = 0.709$. By rearranging and squaring, we produce the following statement: according to SPH simulations [31], the maximum fraction of energy deposited to the interface in RMI is proportional to A^2 scaled by coefficient $0.709^2 = 0.503$. In other words, the maximum of E_0/E_∞ is roughly half of the Atwood number squared.

An alternate value of the ratio of energies can be found by finding the zero of the derivative of Equation 5.2. The maximum of Equation 5.2 occurs when $a_0/\lambda = 1/c_2$. By plugging the location of the maximum back into the

original equation, we obtain a peak value of $\langle [v_0/Av_\infty]_{max} \rangle = 0.64$ leading to energy ratio $E_0/E_\infty \sim 0.4A^2$. In either method of calculation, this result is the upper bound of the ratio of energy partitioning. In the limit of $A \rightarrow 1$, the energy ratio approaches 0.4 or 0.5, implying that the absolute maximum of energy deposited at the interface is half of the energy of the bulk motion.

We find both the peak value and the position of the peak value of v_0/Av_∞ . In order to determine the position of the peak, we look at the empirical model's derivative. The derivative of the empirical model is zero when $(a_0/\lambda)_{peak} = 1/C_2$. The average value of $1/C_2$ is 0.361 with a standard deviation of 0.0266 corresponding to a 7% deviation. This means that the maximum amount of energy is deposited to the interface when the initial perturbation amplitude is roughly one third of the perturbation wavelength. For applications such as inertial confinement, where the development of RMI interfacial growth hinders combustion, experiment designers may want to insure the interface has no perturbations of amplitude near one third the wavelength. This result provides a possible method of controlling RMI growth.

5.6 Discussion

SPH simulations may provide more complete information about the system than experiments and the simulated parameters are more controllable than experiments. As discussed in Section 1.1, a synergistic analysis provides more knowledge than the presentation of data alone. The initial interfacial growth rate of RMI is known to depend on the initial perturbation amplitude. A recent study has shown a surprising non-monotonic dependence [31] that we describe quantitatively and analyze in regards to fundamental physical values such as the energy deposited to the interface.

Using measurements of the background velocity and the interface's initial growth rate obtained in [31] we compare results with theory, describe the data with an empirical model, and investigate what data may tell us about the energy partitioning between the bulk motion and the growth of the interface.

We compared simulated values of v_∞ , the background motion with theory [103] and achieve excellent agreement. The simulated and theoretical values differ by less than 1% in all cases (Table 5.2). This agreement validates the use of SPH code in this extreme parameter regime.

The simulated values of the initial interfacial growth rate v_0 are also analyzed and compared with theory. For small values of the initial perturbation

amplitude, a_0 , the simulations agree with linear theory and weakly nonlinear theory. However the simulated initial growth rate is significantly smaller than weakly nonlinear theory for large initial perturbation amplitudes as seen in Figure 5.4. The existing theory is unable to adequately describe the data for large initial perturbation amplitudes. This opens the door for new descriptions of RMI evolution in the case of large initial perturbation amplitude and may have consequences in the design of inertial confinement fusion experiments. The existing theory states that the growth rate has a monotonic dependence on a_0 , indicating that to minimize growth, one should use the smallest initial perturbation amplitude possible. However, the simulation results suggest the interface growth rate has a maximum around $a_0 \sim 1/3\lambda$ and may be small at large initial perturbation amplitudes.

To describe the initial growth rate data, we use an empirical model of the form $C_1 \frac{a_0}{\lambda} e^{-C_2 \frac{a_0}{\lambda}}$. When fit to the simulated data, this model reproduces the theoretical results at small initial perturbation amplitude ($a_0/\lambda \sim < 0.1$) while also describing the data at large initial perturbation amplitude. An example of the data shown with the fit is seen in Figure 5.6a. The fit parameter C_1 is related to the linear and weakly nonlinear theories and varies with Mach and Atwood number. The fit parameter C_2 is remarkably constant over the simulated parameter range. C_2 variation is 7% while Mach number ranges from 3 to 10 and the density ratio changes by an order of magnitude (Table 5.3). The exponent may provide insight into the RM interface growth for large initial perturbation amplitudes.

We measure the peak value of the initial growth rate as well as the position of the peak. For all simulated values of Mach and Atwood number, the peak value of the initial growth rate occurs between $a_0/\lambda = 0.35$ and 0.4 (Figure 5.5a). The position of the peak seems to be the same for different combinations of parameters. It is constant with respect to the parameters varied in this study, Mach and Atwood number. This study does not address the behavior with respect to other important parameters such as the adiabatic index (γ), and further simulations and analysis are needed to verify the universality of the perturbation amplitude corresponding to the peak growth rate.

Since both bulk motion, v_∞ and the interface growth, v_0 are measured, we analyze their ratio in order to study the partitioning of energy between the bulk and the interface. The maximum value of the velocity ratio can provide an upper limit to the maximum fraction of energy deposited to the interface during RMI. We find that the maximum energy ratio is $\sim 0.5A^2$,

indicating that the upper limit on the relative growth rate of the interface is approximately half of the Atwood number squared. In reality, this quantity may be even smaller due to losses. At late times of RMI evolution, the energy of the interface may be even smaller due to the appearance of small scale structures and interfacial mixing.

SPH simulations provide valuable data for understanding early RMI evolution in the case of strong shocks and high density contrast. The simulated data achieves very good agreement with theory. We are able to discover new trends and place limits on fundamental physical quantities. Further studies are needed in experimental, numerical, and theoretical avenues in order to verify and expand on the results.

Chapter 6

Conclusion

This work provides an example of the much needed analysis of RTI/RMI experiments and simulations. The field will benefit from more comprehensive analyses of data, rather than publishing experimental results alone. There exists a plethora of data that may still be analyzed systematically, as exemplified in this thesis. Future work may improve the fits of experimental data by exploring well designed parameter spaces, modeling a wider range of stochastic effects, and measuring delicate, small scale flow features in simulations. We present three sets of systematic data analysis of Rayleigh-Taylor unstable flows.

Data analysis of laboratory supernova experiments

We conduct a thorough analysis of experimental data in supernova experiments conducted at high powered laser facilities. We discover more information from experimental images than previous studies, evaluating what information experiments and simulations may tell us about the fundamentals of RTI and RT mixing in HEDP by comparing the data with rigorous theoretical approaches. The radius of curvature of the interface, as seen in all available images, is analyzed and determined to be an imprint of initial conditions.

Although the specific experimental condition causing the curvature is unable to be determined from the experimental images and available simulations, it is a topic of future study. Investigating how the curvature is imprinted on to the system would involve simulations of multiple simultaneous physical phenomenon including laser-material interactions, boundary

effects, and ionization effects as well as experiments carefully designed to isolate physical processes of laser ablation creating a blast wave in a finite domain.

The confirmation of a non-evolving (constant) curvature allows us to analyze more than a single spike per image to determine the interface amplitude. More measurements improve the analysis shown here and may be used in future analysis of laboratory supernova experiments.

The growth of the amplitude in laboratory supernova experiments was measured and found to grow as a power law with exponent $>\sim 1$, indicating that the interface does accelerate. The experimental data were compared with theoretical models and simulation results. All are within good agreement and a larger dynamic range of data or data with higher resolution are needed to differentiate the different models. Future studies using greater quantity or higher quality of experimental data may be able to make stronger statements about the growth of the interface in Rayleigh-Taylor flows in the high energy density regime.

With a greater quantity of data, future studies could also perform statistical analysis on the spread of coefficient values. As demonstrated in Chapter 4, the fluctuations of the coefficient may be related to fluctuations inherent in Rayleigh-Taylor mixing. An integrated study comparing stochastic modeling and experimental data may provide valuable insight to the fundamental processes occurring on small scales in RTI.

Data analysis of a stochastic model of RT mixing

We study the statistically unsteadiness of RT mixing by numerically modeling the set of stochastic nonlinear differential equations which govern the rate of change of momentum in a packet of fluid undergoing RT instability. We model multiplicative noise in the acceleration dominated mixing regime and the dissipation dominated mixing regime. By analyzing the modeled solutions, we measure the influence of fluctuations on measurable quantities like the power law describing the growth of the interface. New characteristic values are found which may be used as a diagnostic. The numerical differential equation solver, which typically averages over thousands of trajectories, is also run for a single trajectory in the steady state case and the spectra of fluctuations is measured.

We find that the power law solution's exponent is less sensitive to fluctuations than the coefficient and therefore may be a better diagnostic measure-

ment. Although determining the exponent of power laws requires measurements over long dynamic ranges, this would more reliably characterize the system. Another diagnostic that may be used in experiments and simulations are the two characteristic values in the mixing regime. The subregime (acceleration dominated or dissipation dominated mixing regime) of the system can be determined by looking at the characteristic values described in Section 4.

A similar model has been used to study the constant acceleration case and time dependent power law accelerations with exponents > -1 . Here we analyze time dependent power law accelerations with exponents between -2 and 0 . Future studies using the same infrastructure may study spatially varying accelerations rather than accelerations as a function of time. Accelerations with power law dependence on position are expected to have subregimes analogous, but not equivalent to the subregimes in the mixing regime (acceleration and dissipation dominated mixing).

Data analysis of simulated RMI interfacial growth

We investigate the effect of the initial perturbation amplitude on the RMI interfacial dynamics using Single Particle Hydrodynamics simulations. The compound motion of the interface and bulk fluid flow is measured, an empirical model is found to describe data, and we find an upper bound for the amount of energy deposited to the interface.

The velocities describing large scale RMI evolution are measured. We use the measured background velocity as a characteristic velocity. The initial growth rate of the velocity is measured and its behavior with respect to the initial perturbation amplitude is investigated. A non-monotonic dependence, as seen in [31] is described by an empirical model. We measure the maximum and the initial perturbation amplitude corresponding to the maximum. By relating the velocity ratios to the energy ratios, we find an upper bound for the amount of energy deposited to the interface in RMI.

We present several important results from SPH data, yet the data analyzed in this thesis have not been analyzed to their full extent. It is easy to find new measurements to make on existing data, especially from simulations which contain vast amounts of information. In particular, future studies should include quantitative analysis of scalar and velocity fields and the effect of the adiabatic indices of the two fluids.

Experimentally, it would be useful to verify the result that the initial

growth rate has a non-monotonic dependence of the initial perturbation amplitude. By conducting series of experiments with varying initial amplitudes in both hydrodynamic systems and high energy density plasmas, we may better understand this important result leading to control of RTI/RMI in applications such as inertial confinement fusion. Additionally, there exists experimental data that may be simulated using SPH code and analyzed in a similar manner as this thesis.

In order to determine the role that hot spots and cumulative jets play in RT/RM dynamics [66, 67], the pressure and temperature gradients across the interface should be measured. It is evident from qualitative analysis of simulation results that the pressure varies along the length of a spike. Future investigations can study the relationship between this pressure gradient and the growth of the interface. Does the pressure gradient relate directly to the growth of the interface or do they have a more complicated relationship?

RT mixing is known to have physical characteristics distinct from canonical Kolmogorov turbulence [71, 2]. A quantitative statistical analysis of the velocity field at late times can be compared with Kolmogorov turbulence may be achieved with SPH simulations.

The adiabatic index, γ of the fluids is an indication of the compressibility of the fluid. When studying systems with strong pressure fluctuations (inherent in RMI), the compressibility may have a significant effect on the dynamics. Future studies will investigate the γ effect on the non-monotonic dependence of the initial interfacial growth rate on the initial perturbation amplitude. Such a study would enhance the empirical model and better describe RMI for large initial perturbations.

Data analysis of Rayleigh-Taylor unstable flows

Overall we present a systematic analysis of RT unstable flows, acquiring new findings from multiple sources of data. Due to funding for inertial confinement fusion research and the large simulations capable today, Rayleigh-Taylor and Richtmyer-Meshkov flows provide immense sources of unanalyzed data. These problems, while ubiquitous in nature and applications, are still challenging: analysis must account for statistical unsteadiness, multiple scales, nonlinearity, nonlocalness, and especially in the case of high energy density, multiple physical effects. In the future, we hope more analyses in the same style as this thesis may be carried out to better understand the challenging topic of Rayleigh-Taylor unstable flows.

Contributions

This thesis builds upon data and research of others. In this section we spell out exactly what steps were done by the author and what steps are provided by others.

Data analysis of laboratory supernova experiments

The experiment was conceived and conducted by researchers at Lawrence Livermore National Laboratory, University of Michigan, and the Omega Laser Facility. Several are listed as co-authors in reference [94] and related work can be found in [37, 57, 55, 56, 79, 81]. Carolyn Kuranz provided experimental images and corresponding experimental quantities (e.g. target specifications). We performed analysis of those images and published the results in [94]. This publication is the basis of Chapter 3.

Specifically, Figures 2.1 and 2.2 were provided by our collaborators and Figures 3.1 through 3.4, Tables 3.1-3.2, and corresponding discussion are original work from the author.

Data analysis of a stochastic model of RT mixing

The numerical differential equation solver used in Chapter 4 was previously used in [5, 6]. In previous studies, the acceleration exponent varied from 0 to -1 . In this thesis we present similar analyses of acceleration exponents between -1 and -2 in addition to new types of analysis.

We applied the numerical differential equation solver to a new regime (extending beyond previously studied parameter ranges) and are responsible for all of the figures in Chapter 4.

Data analysis of simulated RMI interfacial growth

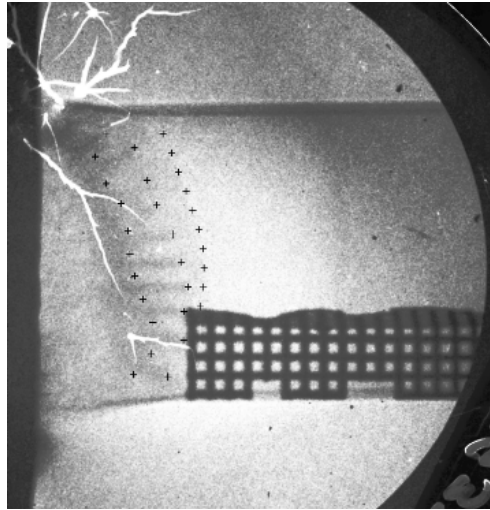
Chapter 5 builds upon the work in [31]. Zachary Dell, a student who studied with Snezhana Abarzhi, ran simulations using code from Stellingwerf Consulting [93] and measured the values of background motion (v_∞) and interface growth (v_0) and provided Figures 5.1 through 5.4. Zachary's data is used in Figures 5.5 and 5.6 although the actual figures and related discussion is work from the author.

We analyzed the velocities, including the development and implementation of the empirical model (Section 5.4.3), the study of energy partitioning (Section 5.5) and are responsible for Figures 5.5 through 5.6.

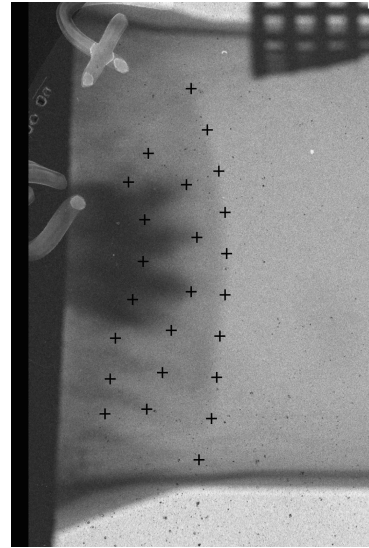
Appendix

Experimental Images

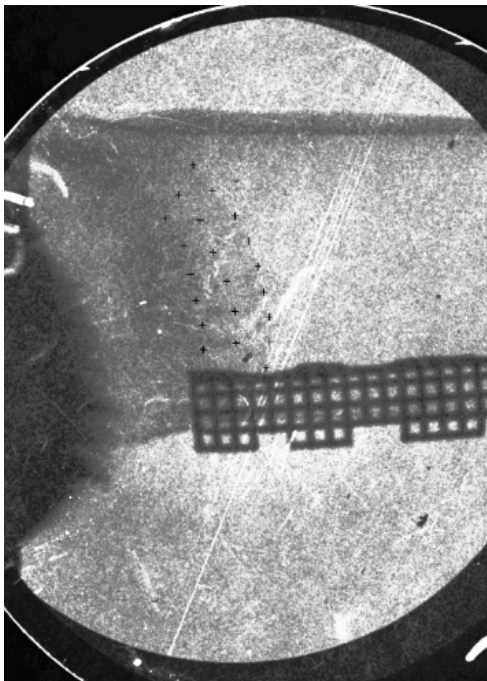
Here we present all 12 images from which spike amplitude measurements were made. They are grouped according to target type. In addition, images of planar target types are shown. In planar experiments, bubbles and spikes do not develop but they were used for measurements of shock curvature. In all cases the shock propagates from left to right and the small crosses indicate position measurements.



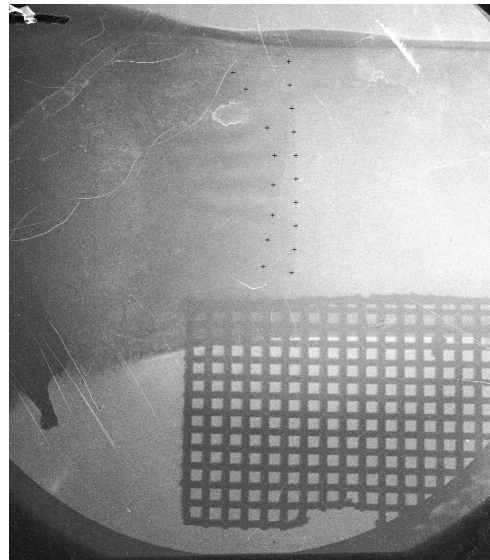
(a) Taken at 17 ns



(b) Taken at 17 ns

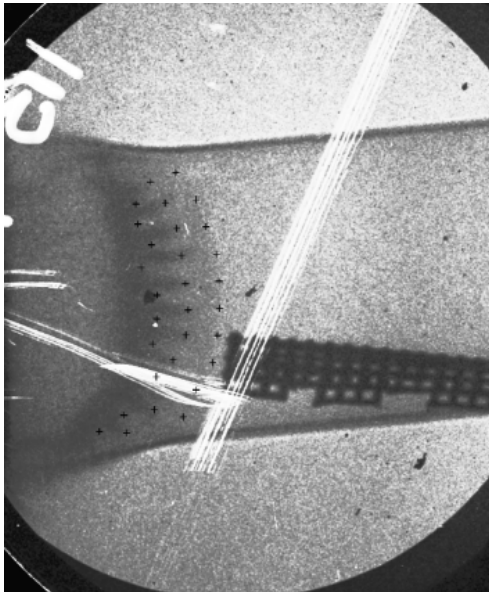


(c) Taken at 21 ns

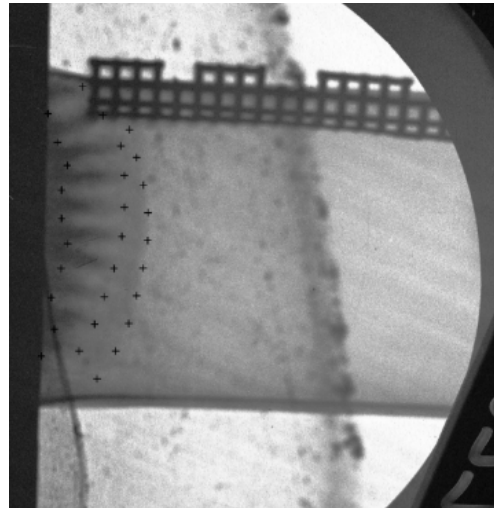


(d) Taken at 25 ns

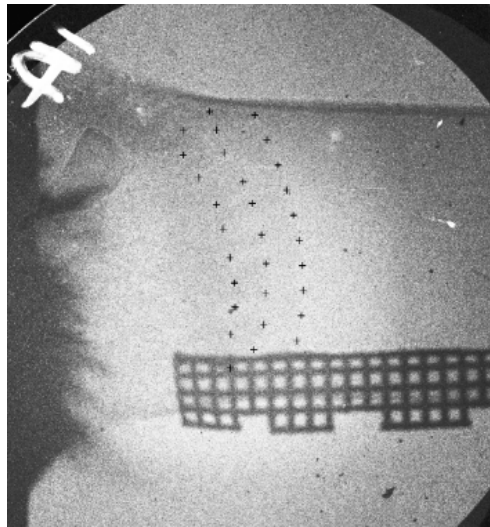
Figure 6.1: Experimental images from single mode target types.



(a) Taken at 17 ns

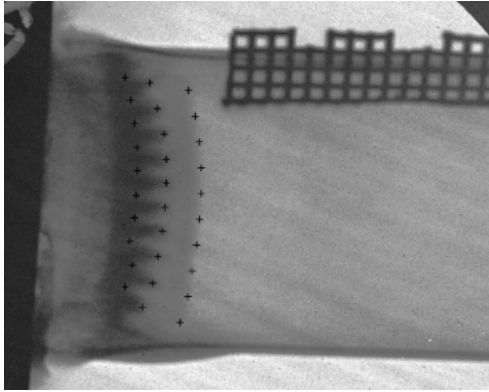


(b) Taken at 17 ns

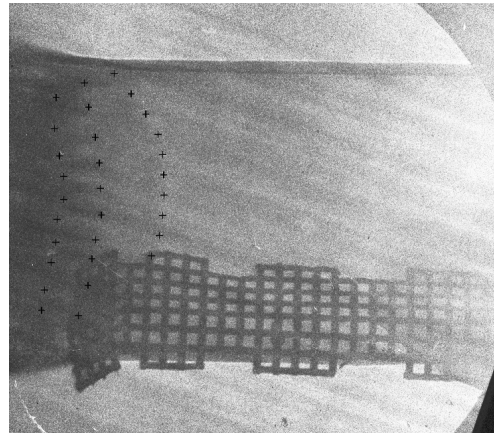


(c) Taken at 21 ns

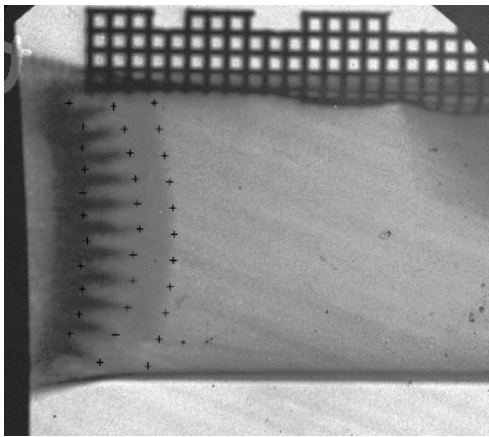
Figure 6.2: Experimental images from small-two-mode target types.



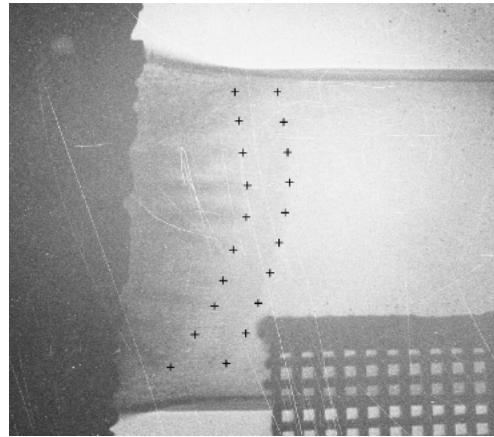
(a) Taken at 13 ns



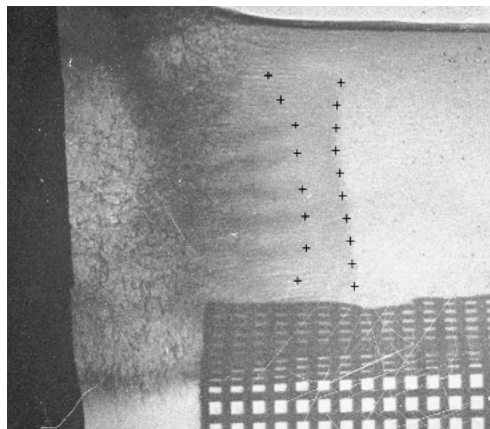
(b) Taken at 17 ns



(c) Taken at 17 ns

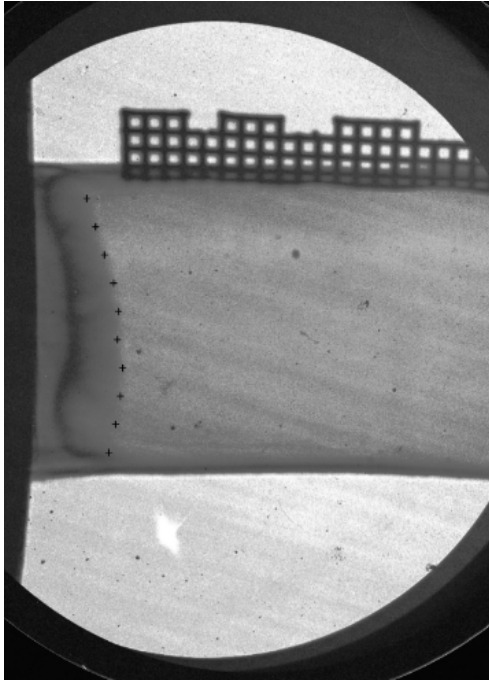


(d) Taken at 21 ns

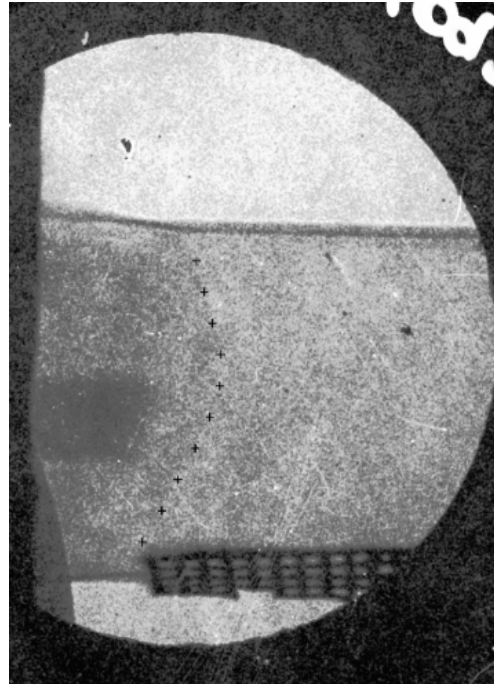


(e) Taken at 25 ns

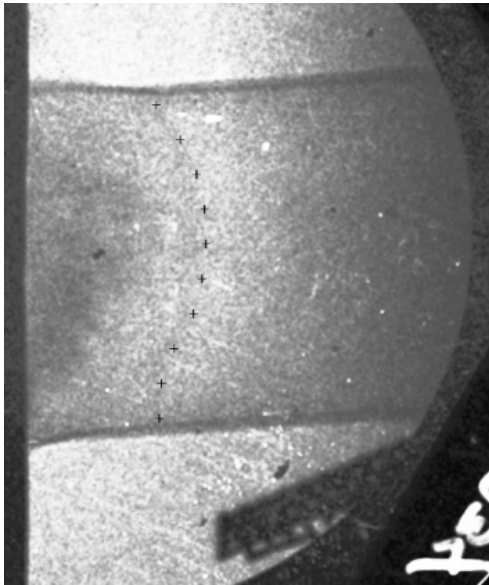
Figure 6.3: Experimental images from large-two-mode target types.



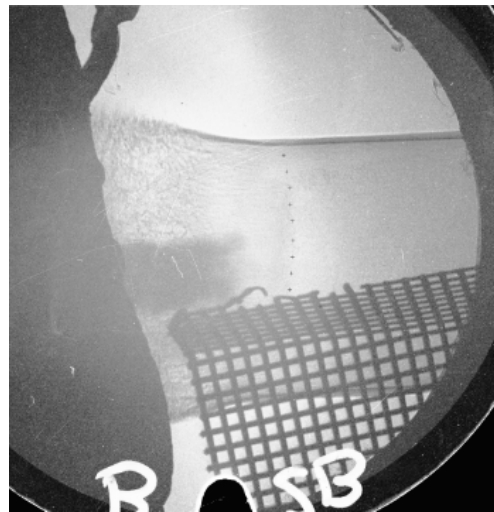
(a) Taken at 13 ns



(b) Taken at 17 ns



(c) Taken at 21 ns



(d) Taken at 25 ns

Figure 6.4: Experimental images from planar target types.

Bibliography

- [1] S. Abarzhi. A new type of the evolution of the bubble front in the Richtmyer-Meshkov instability. *Physics Letters A*, 294:95–100, Feb. 2002.
- [2] S. Abarzhi. Review of nonlinear dynamics of the unstable fluid interface: conservation laws and group theory. *Physica Scripta*, T132:18, December 2008.
- [3] S. Abarzhi. On fundamentals of Rayleigh-Taylor turbulent mixing. *Europhysics Letters*, 91(35001):5, August 2010.
- [4] S. Abarzhi. Review of theoretical modelling approaches of Rayleigh-Taylor instabilities and turbulent mixing. *Philosophical Transactions of the Royal Society A*, 368(1809):21, March 2010.
- [5] S. Abarzhi, M. Cadjan, and S. Fedotov. Stochastic model of Rayleigh-Taylor turbulent mixing. *Physics Letters A*, 371(457):5, June 2007.
- [6] S. Abarzhi, M. Cadjan, and A. Qamar. Stochastic modeling of statistically unsteady processes. *Physica Scripta*, T155(014046):10, July 2013.
- [7] S. Abarzhi, S. Gauthier, and K. Sreenivasan. Introduction II, Introduction I, Preface: Turbulent mixing and beyond: Non-equilibrium processes from atomistic to astrophysical scales. *Philosophical Transactions of the Royal Society A*, 371:20130268, 20120436, 20120435, 2013.
- [8] S. Abarzhi, A. Gorobets, and K. Sreenivasan. Turbulent mixing in immiscible, miscible and stratified media. *Physics of Fluids*, 17(081705), 2005.

- [9] S. Abarzhi, K. Nishihara, and J. Glimm. Rayleigh-Taylor and Richtmyer-Meshkov instabilities for fluids with a finite density ratio. *Physics Letters A*, 317(470), 2003.
- [10] S. Abarzhi, K. Nishihara, and R. Rosner. Multi-scale character of the large-scale coherent dynamics in the Rayleigh-Taylor instability. *Physical Review E*, 73(036310), 2006.
- [11] S. Abarzhi and R. Rosner. A comparative study of approaches for modeling Rayleigh-Taylor turbulent mixing. *Physica Scripta*, T142(014012):13, December 2010.
- [12] S. I. Abarzhi. The stationary spatially periodic flows in Rayleigh-Taylor instability: solutions multitude and its dimension. *Physica Scripta*, 1996(T66):238, 1996.
- [13] U. Alon, J. Hecht, D. Mukamel, and D. Shvarts. Scale-invariant mixing rate of hydrodynamically unstable interfaces. *Phys. Rev. Lett.*, 72(2867), 1994.
- [14] J. Anderson. *Modern Compressible Flow with Historical Perspective*. McGraw-Hill Companies, New York, 2nd ed. edition, 1990.
- [15] S. Anisimov, R. P. Drake, S. Gauthier, E. Meshkov, and S. Abarzhi. What is certain and what is not so certain in our knowledge of Rayleigh-Taylor mixing? *Philosophical Transactions of the Royal Society A*, 371(20130266):15, October 2013.
- [16] S. Anisimov, A. Prokhorov, and V. Fortov. Application of high-power lasers to study matter at ultrahigh pressures. *Sov. Phys. Usp.*, 27:181–205, 1984.
- [17] D. Arnett. *Supernovae and Nucleosynthesis: An Investigation of the History of Matter from the Big Bang to the Present*. Princeton University Press, Princeton, NJ, 1996.
- [18] D. Arnett, C. A. Meakin, and P. Young. Turbulent convection in stellar interiors. II. The velocity field. *Astrophysics J.*, 690(1715), 2009.
- [19] G. Barenblatt. *Similarity, Self-Similarity and Intermediate Asymptotics*. Consultants Bureau, New York, 1979.

- [20] G. Batchelor. *The Theory of Homogeneous Turbulence*. Cambridge University Press, Cambridge, 1953.
- [21] S. Belenki and E. Fradkin. Theory of turbulent mixing. *Trudi FIAN (in Russian)*, 29:207–233, 1965.
- [22] T. Boehly, R. Craxton, T. Hinterman, J. Kelly, T. Kessler, S. Kumpan, S. Letzring, R. McCrory, F. Morse, W. Seka, S. Skupsky, J. Soures, and C. Verdon. The upgrade to the OMEGA laser system. *Rev. Sci. Instrum.*, 66:508–510, 1995.
- [23] S. Braginski. *Reviews in Plasma Physics*. Consultants Bureau, New York, 1965.
- [24] M. Brouillette. The Richtmyer-Meshkov Instability. *Annual Review of Fluid Mechanics*, 34(1):445–468, 2002.
- [25] W. Cabot and A. Cook. Reynolds number effects on Rayleigh-Taylor instability with possible implications for type-Ia supernovae. *Nat. Phys.*, 2(562), 2006.
- [26] Chandrasekhar. *Hydrodynamic and Hydromagnetic Stability*, 3rd ed. Dover, New York, 1981, pp. 428-477.
- [27] B. Cheng, J. Glimm, and D. Sharp. Density dependence of Rayleigh–Taylor and Richtmyer–Meshkov mixing fronts. *Physics Letters A*, 268(4–6):366 – 374, 2000.
- [28] D. Clark, S. Haan, A. Cook, M. Edwards, B. Hammel, J. Koning, and M. Marinak. Short-wavelength and three dimensional instability evolution in National Ignition Facility ignition capsule designs. *Phys. Plasmas*, 18(082701), 2011.
- [29] S. Dalziel, P. Linden, and D. Youngs. Self-similarity and internal structure of turbulence induced by Rayleigh–Taylor instability. *Journal of Fluid Mechanics*, 399:1–48, 11 1999.
- [30] R. Davies and G. Taylor. The mechanics of large bubbles rising through extended liquids and through liquids in tubes. *Proc. R. Soc. London, Ser. A.*, 200(375), 1950.

- [31] Z. Dell, R. F. Stellingwerf, and S. Abarzhi. Effect of initial perturbation amplitude on Richtmyer-Meshkov flows induced by strong shocks. *Physics of Plasmas*, 22(9), 2015.
- [32] B. Demaske, V. Zhakhovsky, N. Inogamov, and I. Oleynik. Ultrashort shock waves in nickel induced by femtosecond laser pulse. *Physical Review B*, 87(054109), 2013.
- [33] G. Dimonte. Spanwise homogeneous buoyancy-drag model for Rayleigh-Taylor mixing and experimental evaluation. *Physics of Plasmas*, 7:2255–2269, 2000.
- [34] G. Dimonte, D. Youngs, A. Dimitis, S. Weber, M. Marinak, S. Wunsch, C. Garasi, A. Robinson, M. Andrews, P. Ramaprabhu, A. Calder, B. Fryxell, J. Biello, L. Dursi, P. MacNeice, K. Olson, P. Ricker, R. Rosner, F. Timmes, H. Tufo, Y. Young, and M. Zingale. A comparative study of the turbulent Rayleigh-Taylor instability using high resolution three-dimensional numerical simulations: The Alpha-Group collaboration. *Physics of Fluids*, 16:1668–1693, 2004.
- [35] P. Dimotakis. The mixing transition in turbulent flows. *Journal of Fluid Mechanics*, 409:69–98, 200.
- [36] R. P. Drake. Perspectives of high energy density physics. *Physics of Plasmas*, 16(055501), 2009.
- [37] R. P. Drake, D. Leibbrandt, E. Harding, C. Kuranz, M. Blackburn, H. Robey, B. Remington, M. Edwards, A. Miles, T. Perry, R. Wallace, H. Louis, J. Knauer, and D. Arnett. Nonlinear mixing behavior of the three-dimensional Rayleigh-Taylor instability at a decelerating interface. *Physics of Plasmas*, 11(5):9, April 2004.
- [38] P. R. Garabedian. On steady-state bubbles generated by Taylor instability. *Proceedings of the Royal Society of London A: Mathematical, Physical and Engineering Sciences*, 241(1226):423–431, 1957.
- [39] S. G. Glendinning, J. Bolstad, D. G. Braun, M. J. Edwards, W. W. Hsing, B. F. Lasinski, H. Louis, A. Miles, J. Moreno, T. A. Peyser, B. A. Remington, H. F. Robey, E. J. Turano, C. P. Verdon, and Y. Zhou. Effect of shock proximity on Richtmyer–Meshkov growth. *Physics of Plasmas*, 10(5):1931–1936, 2003.

- [40] J. Glimm and D. Sharp. Chaotic mixing as a renormalization-group fixed-point. *Phys. Rev. Lett.*, 64:2137–2139, 1990.
- [41] G. Guderly. Starke kugelige und zylindrische verdichtungsstöße in der Nähe des kugelmittelpunktes bzw. der zylinderachse. *Luftfahrtforschung*, 19:302–312, 1942.
- [42] S. Haan, J. Lindl, D. Callahan, D. Clark, J. Salmonson, B. Hammel, L. Atherton, R. Cook, M. Edwards, S. Glenzer, A. Hamza, S. Hatchett, M. Herrmann, D. Hinkel, D. Ho, H. Huang, O. Jones, J. Kline, G. Kyrala, O. Landen, B. MacGowan, M. Marinak, D. Meyerhofer, J. Milovich, K. Moreno, E. Moses, D. Munro, A. Nikroo, R. Olson, K. Peterson, S. Pollaine, J. Ralph, H. Robey, B. Spears, P. Springer, L. Suter, C. Thomas, R. Town, R. Vesey, S. Weber, H. Wilkens, and D. Wilson. Point design targets, specifications, and requirements for the 2010 ignition campaign on the National Ignition Facility. *Physics of Plasmas*, 18(5), 2011.
- [43] B. Hammel, S. Haan, D. Clark, M. Edwards, S. Langer, M. Marinak, M. Patel, J. Salmonson, and H. Scott. High-mode Rayleigh-Taylor growth in {NIF} ignition capsules. *High Energy Density Physics*, 6(2):171 – 178, 2010. {ICHED} 2009 - 2nd International Conference on High Energy Density Physics.
- [44] X. He, R. Zhang, S. Chen, and G. Doolen. On the three-dimension Rayleigh-Taylor instability. *Physics of Fluids*, 11(1143), 1999.
- [45] M. Herrmann, P. Moin, and S. Abarzhi. Nonlinear evolution of the Richtmyer-Meshkov instability. *Journal of Fluid Mechanics*, 612(311):28, June 2008.
- [46] R. Holmes, G. Dimonte, B. Fryxell, M. Gittings, J. Grove, M. Schneider, D. Sharp, A. Velikovich, R. Weaver, and Q. Zhang. Richtmyer-Meshkov instability growth: Experiment, simulation and theory. *Journal of Fluid Mechanics*, 389:55–79, 6 1999.
- [47] O. Hurricane, D. Callahan, D. Casey, E. Dewald, T. Dittrich, T. Döppner, M. Barrios Garcia, D. Hinkel, L. Berzak Hopkins, P. Kervin, J. Kline, S. L. Pape, T. Ma, A. MacPhee, J. Milovich, J. Moody, A. Pak, P. Patel, H. Park, B. Remington, H. Robey,

- J. Salmonson, P. Springer, R. Tommasini, L. Benedetti, J. Caggiano, P. Celliers, C. Cerjan, R. Dylla-Spears, D. Edgell, M. Edwards, D. Fittinghoff, G. Grim, N. Guler, N. Izumi, J. Frenje, M. Gatu Johnson, S. Haan, R. Hatarik, H. Herrmann, S. Khan, J. Knauer, B. Koziowski, A. Kritcher, G. Kyrala, S. Maclaren, F. Merrill, P. Michel, J. Ralph, J. Ross, J. Rygg, M. Schneider, B. Spears, K. Widmann, and C. Yeamans. The high-foot implosion campaign on the National Ignition Facility. *Physics of Plasmas*, 21(5), 2014.
- [48] N. Inogamov. Higher-order Fourier approximations and exact algebraic solutions in the theory of the hydrodynamic Rayleigh-Taylor instability. *JETP letters*, 55(9):521–525, 1992.
- [49] B. Johnson and O. Schilling. Reynolds-averaged Navier–Stokes model predictions of linear instability. I: Buoyancy- and shear-driven flows. *Journal of Turbulence*, 12:N36, 2011.
- [50] M. Jones and J. Jacobs. A membraneless experiment for the study of Richtmyer–Meshkov instability of a shock-accelerated gas interface. *Physics of Fluids*, 9(10):3078–3085, 1997.
- [51] A. Kolmogorov. The Local Structure of Turbulence in Incompressible Viscous Fluid for Very Large Reynolds’ Numbers. *Akademiia Nauk SSSR Doklady*, 30:301–305, 1941.
- [52] Y. Kucherenko, S. Balabin, R. Ardashova, O. Kozelkov, and A. Dulov. Experimental study of the influence of the stabilizing properties of transitional layers on the turbulent mixing evolution. *Laser Part. Beams*, 21(369), 2003.
- [53] Y. Kucherenko, O. Shestachenko, S. Balabin, and A. Pylaev. Multifunctional shock tube for investigating the evolution of instabilities in non-stationary gas dynamic flows. *Laser Part. Beams*, 21(381), 2003.
- [54] H. J. Kull. Theory of the Rayleigh-Taylor instability. *Phys. Rep.*, 206:197–325, Aug. 1991.
- [55] C. Kuranz, R. P. Drake, M. Grosskopf, A. Budde, C. Krauland, D. Marion, A. Visco, J. Ditmar, H. Robey, B. Remington, A. Miles, A. Cooper, C. Sorce, T. Plewa, N. Hearn, K. Killebrew, J. Knauer, D. Arnett, and

- T. Donajkowski. Three-dimensional blast-wave-driven Rayleigh-Taylor instability and the effects of long-wavelength modes. *Physics of Plasmas*, 16(5), 2009.
- [56] C. Kuranz, R. P. Drake, M. Grosskopf, B. Fryxell, A. Budde, J. Hansen, A. Miles, T. Plewa, N. Hearn, and J. Knauer. Spike morphology in blast-wave-driven instability experiments. *Physics of Plasmas*, 17(5), 2010.
- [57] C. Kuranz, R. P. Drake, E. Harding, M. Grosskopf, H. Robey, B. Remington, M. Edwards, A. Miles, T. Perry, B. Blue, T. Plewa, N. Hearn, J. Knauer, D. Arnett, and D. Leibbrandt. Two-dimensional blast-wave-driven Rayleigh-Taylor instability: Experiment and simulation. *The Astrophysical Journal*, 696(1):749, 2009.
- [58] L. Landau and E. Lifshitz. *Course of Theoretical Physics VI, Fluid Mechanics*. Pergamon Press, New York, 1987.
- [59] J. Larsen and S. Lane. HYADES—A plasma hydrodynamics code for dense plasma studies. *Journal of Quantitative Spectroscopy and Radiative Transfer*, 51(1):179 – 186, 1994.
- [60] P. Linden, J. Redondo, and D. Youngs. Molecular mixing in Rayleigh-Taylor instability. *Journal of Fluid Mechanics*, 265(97), 1994.
- [61] J. Lindl, P. Amendt, R. Berger, S. Glendinning, S. Glenzer, S. Haan, R. Kauffman, O. Landen, and L. Suter. The physics basis for ignition using indirect-drive targets on the National Ignition Facility. *Physics of Plasmas*, 11(2):339–491, 2004.
- [62] M. Marinak, S. Glendinning, R. Wallace, B. Remington, K. Budil, S. Haan, R. Tipton, and J. Kilkenny. Nonlinear Rayleigh-Taylor evolution of a three-dimensional multimode perturbation. *Phys. Rev. Lett.*, 80(4426), 1998.
- [63] C. A. Meakin and D. Arnett. Turbulent convection in stellar interiors. i. hydrodynamic simulation. *The Astrophysical Journal*, 667(1):448, 2007.
- [64] E. Meshkov. Instability of the interface of two gases accelerated by a shock wave. *Fluid Dynamics*, 4(5):101–104, 1969.

- [65] E. Meshkov. Instability of shock-accelerated interface between two media. *Proceedings of the 1st International Workshop on the Physics of Compressible Turbulent Mixing, Princeton, USA (1988)*, pages 473–503, 1992.
- [66] E. Meshkov. *Studies of Hydrodynamic Instabilities in Laboratory Experiments*. Number ISBN: 5-9515-0069-9. FGYS-VNIIEF, Sarov (in Russian), 2006.
- [67] E. Meshkov. Some peculiar features of hydrodynamic instability development. *Philosophical Transactions of the Royal Society of London A: Mathematical, Physical and Engineering Sciences*, 371(2003), 2013.
- [68] E. Meshkov, V. Nikiforov, and A. Tolshmyakov. Structure of the turbulent mixing zone on the boundary of two gases accelerated by a shock wave. *Combustion, Explosion and Shock Waves*, 26(3):315–320, 1990.
- [69] B. Motl, J. Oakley, D. Ranjan, C. Weber, M. Anderson, and R. Bonazza. Experimental validation of a Richtmyer–Meshkov scaling law over large density ratio and shock strength ranges. *Physics of Fluids*, 21(12), 2009.
- [70] R. Narasimha and K. R. Sreenivasan. Relaminarization in highly accelerated turbulent boundary layers. *Journal of Fluid Mechanics*, 61:417–447, 11 1973.
- [71] A. Nepomnyashchy and S. Abarzhi. Monochromatic waves induced by large-scale parametric forcing. *Physical Review E*, 81(037202):4, March 2010.
- [72] V. Neuvazhaev. Theory of turbulent mixing. *Sov. Phys. Dokl.*, 20:398–400, 1975.
- [73] V. Neuvazhaev. *Mathematical Modeling of Turbulent Mixing*. Number ISBN: 5-902278-19-8. Russian Federal Nuclear Center Publishing, 2007.
- [74] K. Nishihara, J. G. Wouchuk, C. Matsuoka, R. Ishizaki, and V. V. Zhakhovsky. Richtmyer–Meshkov instability: theory of linear and nonlinear evolution. *Philosophical Transactions of the Royal Society of London A: Mathematical, Physical and Engineering Sciences*, 368(1916):1769–1807, 2010.

- [75] S. Orlov, S. Abarzhi, S. Oh, G. Barbastathis, and K. Sreenivasan. High-performance holographic technologies for fluid dynamics experiments. *Philosophical Transactions of the Royal Society A*, 368(10.1098):31, March 2010.
- [76] P. Ramaprabhu and M. Andrews. Experimental investigation of Rayleigh-Taylor mixing at small Atwood numbers. *Journal of Fluid Mechanics*, 503:233–271, 2003.
- [77] L. Rayleigh. Investigations of the character of the equilibrium of an incompressible heavy fluid of variable density. *Proc. London Math. Soc.*, 14:170–177, 1883.
- [78] K. Read. Experimental investigation of turbulent mixing by Rayleigh-Taylor instability. *Physica D: Nonlinear Phenomena*, 12(1):45 – 58, 1984.
- [79] B. Remington, R. P. Drake, and D. Ryutov. Experimental astrophysics with high power lasers and Z pinches. *Rev. Mod. Phys.*, 78:755–807, Aug 2006.
- [80] R. D. Richtmyer. Taylor instability in shock acceleration of compressible fluids. *Communications on Pure and Applied Mathematics*, 13(2):297–319, 1960.
- [81] H. Robey, J. Kane, B. Remington, R. P. Drake, O. Hurricane, H. Louis, R. Wallace, J. Knauer, P. Keiter, D. Arnett, and D. Ryutov. An experimental testbed for the study of hydrodynamic issues in supernovae. *Physics of Plasmas*, 8(5):2446–2453, 2001.
- [82] H. Robey, Y. Zhou, A. Buckingham, P. Keiter, B. Remington, and R. P. Drake. The time scale for the transition to turbulence in a high Reynolds number, accelerated flow. *Physics of Plasmas*, 10(3):614–622, 2003.
- [83] D. Ryutov, M. Derzon, and M. Matzen. The physics of fast Z pinches. *Rev. Mod. Phys.*, 72:167–223, Jan 2000.
- [84] D. Ryutov, R. P. Drake, J. Kane, E. Liang, B. A. Remington, and W. M. Wood-Vasey. Similarity criteria for the laboratory simulation

- of supernova hydrodynamics. *The Astrophysical Journal*, 518(2):821, 1999.
- [85] M. B. Schneider, G. Dimonte, and B. Remington. Large and small scale structure in Rayleigh-Taylor mixing. *Phys. Rev. Lett.*, 80:3507–3510, Apr 1998.
- [86] L. Sedov. Propagation of strong shock waves. *J. Appl. Math. Mech.*, 10(241), 1946.
- [87] L. Sedov. *Similarity and Dimensional Methods in Mechanics*. CRC Press, 10th ed. edition, 1993.
- [88] K. Sreenivasan and S. Abarzhi. Acceleration and turbulence in Rayleigh-Taylor mixing. *Philosophical Transactions of the Royal Society A*, 371(20130267):7, October 2013.
- [89] K. R. Sreenivasan. Fluid turbulence. *Rev. Mod. Phys.*, 71:S383–S395, Mar 1999.
- [90] M. Stanic, J. McFarland, R. Stellingwerf, J. Cassibry, D. Ranan, R. Bonazza, J. Greenough, and S. Abarzhi. Non-uniform volumetric structures in Richtmyer-Meshkov flows. *Physics of Fluids*, 25(106107):15, October 2013.
- [91] M. Stanic, R. Stellingwerf, J. Cassibry, and S. Abarzhi. Scale coupling in Richtmyer-Meshkov flows induced by strong shocks. *Physics of Plasmas*, 19(082706):16, August 2012.
- [92] K. Stanyukovich. *Non-steady Motion of Continuous Media*. Oxford University Press, Oxford, UK, 1960.
- [93] R. Stellingwerf. *SPHC Manual; SPHC User's Guide*. Mission Research Corporation, Albuquerque, New Mexico, version 1.20 edition, 1990.
- [94] N. Swisher, C. Kuranz, D. Arnett, O. Hurricane, B. Remington, H. Robey, and S. Abarzhi. Rayleigh-Taylor mixing in supernova experiments. *Physics of Plasmas*, 22(10), 2015.
- [95] N. Swisher and B. Utter. Flow profile of granular avalanches with imposed vertical vibration. *Granular Matter*, 16(2):175–183, 2014.

- [96] G. Taylor. The criterion for turbulence in curved pipes. *Proceedings of the Royal Society of London A: Mathematical, Physical and Engineering Sciences*, 124(794):243–249, 1929.
- [97] G. Taylor. The formation of a blast wave by a very intense explosion. ii. the atomic explosion of 1945. *Proceedings of the Royal Society of London A: Mathematical, Physical and Engineering Sciences*, 201(1065):175–186, 1950.
- [98] A. Velikovich, M. Herrmann, and S. Abarzhi. Perturbation theory and numerical modelling of weakly and moderately nonlinear dynamics of the incompressible Richtmyer-Meshkov instability. *Journal of Fluid Mechanics*, 751:432–479, 2014. cited By 5.
- [99] J. Waddell, J. Jacobs, and C. Niederhaus. Experimental study of Rayleigh-Taylor instability: Low Atwood number liquid systems with single mode initial perturbations. *Physics of Fluids*, 13(1263), 2001.
- [100] J. White, J. Oakley, M. Anderson, and R. Bonazza. Experimental measurements of the nonlinear Rayleigh-Taylor instability using a magnetorheological fluid. *Phys. Rev. E*, 81:026303, Feb 2010.
- [101] M. Wilson and M. Andrews. Spectral measurements of Rayleigh-Taylor mixing at small Atwood number. *Physics of Fluids*, 14(938), 2002.
- [102] S. Woosley, A. Heger, and T. Weaver. The evolution and explosion of massive stars. *Rev. Mod. Phys.*, 74:1015–1071, Nov 2002.
- [103] J. G. Wouchuk. Growth rate of the Richtmyer–Meshkov instability when a rarefaction is reflected. *Physics of Plasmas*, 8(6):2890–2907, 2001.
- [104] Y. Zeldovich and Y. Raizer. *Physics of Shock Waves and High-temperature Hydrodynamic Phenomena*. Dover, New York, 2nd ed. edition, 2002.
- [105] V. Zhakhovsky, M. Budzevich, N. Inogamov, I. Oleynik, and C. White. Two-zone elastic-plastic single shock waves in solids. *Phys. Rev. Lett.*, 107:135502, Sep 2011.